SYNTHESIS, PRODUCTION AND CHARACTERIZATION OF NEXT GENERATION THERMAL INTERFACE MATERIALS FOR ELECTRONIC APPLICATIONS

A Dissertation

by

CENGIZ YEGIN

Submitted to the Office of Graduate and Professional Studies of
Texas A&M University
in partial fulfillment of the requirements for the degree of

DOCTOR OF PHILOSOPHY

Chair of Committee,	Mustafa Akbulut
Committee Members,	Zhengdong Cheng
	Victor Ugaz
	Patrick Shamberger
Head of Department,	Ibrahim Karaman

December 2016

Major Subject: Materials Science and Engineering

ABSTRACT

The inefficient dissipation of heat is a crucial problem that limits the reliability and performance of all electronic systems. As electronic devices get smaller and more powerful, and moving components of machinery operate at higher speeds, the need for better thermal management strategies is becoming increasingly important. Heat removal during the operation of electronic, electrochemical, and mechanical devices is facilitated by high-performance thermal interface materials (TIMs), which are utilized to couple devices to heat sinks. Herein, we report a new class of TIMs involving the chemical integration of boron nitride nanosheets (BNNS), soft organic linkers, and a metal matrix - which are prepared by chemisorption coupled electrodeposition approach. Thermal and mechanical characterization of the copper-based hybrid nanocomposites involving thiosemicarbazide demonstrates bulk thermal conductivities ranging from 211 to 277 W/(m.K), which are very high considering their relatively low elastic modulus values on the order of 15 to 30 GPa. The synergistic combination of these properties leads to the lowest measured total thermal resistivity to date for a TIM with a typical bondline thickness of 30-50 μm: 0.38 to 0.56 mm^2.K/W. Moreover, its coefficient of thermal expansion (CTE) is 11 ppm/K, forming a mediation zone with a low thermally-induced axial stress due to its close proximity to the CTE of most coupling surfaces needing thermal management. Furthermore, preliminary electrochemical tests revealed that the presence of organic ligands and BNNS in the hybrid nanocomposite TIMs improves the corrosion protection behavior of the TIMs by nearly 72%.

Further analysis of the hybrid nanocomposite TIMs included the replacement of thiosemicarbazide with various organic ligands and the replacement of copper matrix with silver. Compared to all the ligands that were used in copper-based hybrid nanocomposites, the most promising thermal and mechanical test results were obtained from thiosemicarbazide. On the other hand, the best silver-based nanocomposite TIM was determined to be the one involving the ligand 2-mercapto-5-benzimidazolecarboxylic acid, in which the thermal conductivity was near 360 W/m.K, and elastic modulus and hardness were about 35 GPa and 0.25 GPa, respectively. The promising results indicate that metal-inorganic-organic nanocomposite TIMs can be great alternatives to currently used TIMs in the market.

DEDICATION

To my family

ACKNOWLEDGEMENTS

I would like to express my deep gratitude to my advisor Professor Mustafa Akbulut. He has been an exceptional mentor and supported me in every stage of my study. His guidance and patience played a significant role in my research progress and future plans. I also would like to thank my committee members, Dr. Victor Ugaz, Dr. Zhengdong Cheng, and Dr. Patrick Shamberger, for their guidance and valuable comments throughout this research.

It has been a pleasure to work with Nirup Naganbandi on the same project. His great personal character, availability and helpfulness enabled us a fast and smooth progress. Moreover, I also wish to express my good feelings about the past and present group members: Dr. Ming Zhang, Dr. Jun Kyun Oh, Dr. Blake Teipel, Dr. I-Cheng Chen, Dr. Bassem Kheireddin, Mrs. Wei Lu, Ms. Varsha Talari, Mrs. Li Hao and Ms. Paula Choinski. They created an enjoyable working environment for me, helped with some experiments and shared their valuable ideas. Last but not least, I would like to thank the visiting scholar, Dr. Mufrettin Murat Sari, for his positive attitude, friendship and research support throughout his stay in our group.

I wish to extend my appreciation to colleague and wife, Yagmur Yegin, as words cannot explain how grateful I am to her. This work would not be completed without her love, continuous support and positive encouragement. Finally, I give thanks to my parents for their support, both financially and spiritually, in all stages of my life.

CONTRIBUTORS AND FUNDING SOURCES

This work was supervised by a dissertation committee consisting of Professor Mustafa Akbulut (chair), Professors Zhengdong Cheng and Patrick Shamberger of the Department of Materials Science and Engineering, and Professor Victor Ugaz of the Department of Chemical Engineering.

All work for the dissertation was completed by the student, in collaboration with Nirup Nagabandi of the Artie McFerrin Department of Chemical Engineering. Also some parts of the work were completed in collaboration with the people at Texas A&M University: Dr. Alexei Sokolov and Ansam Talib of the Department of Physics and Astronomy, Dr. Stanislav Verkhoturov of the Materials Characterization Facility, and Dr. Homero Castenada, Dr. Shei Sia Su and Dr. Winson Kuo of the National Corrosion and Materials Reliability Center. Additionally, some parts of the work were completed in collaboration with people from outside: Dr. Xuhui Feng, Dr. Charlie King and Dr. Sreekant Narumanchi of National Renewable Energy Laboratory (Golden CO), Dr. Massimo Catalano and Dr. Moon J. Kim of the University of Texas at Dallas, and Dr. Kaiser Matin of DARPA (U.S. Department of Defense).

This work was made possible in part by DARPA of the U.S. Department of Defense under Grant Number D13AP00040. Its contents are solely the responsibility of the authors and do not necessarily represent the official views of the DARPA.

NOMENCLATURE

A	Hamaker Constant
AFM	Atomic force microscopy
ATR-FTIR	Attenuated total reflectance-Fourier transform infrared
BNNS	Boron nitride nanosheets
C_p	Specific heat capacity
CTE	Coefficient of thermal expansion
D_e	Deborah number
DLF	Discovery laser flash
DLS	Dynamic light scattering
E	Elastic modulus
E_a	Activation energy
E_r	Reduced elastic modulus
EDS	Energy dispersive X-ray spectroscopy
EDTA	Ethylenediamine tetraacetic acid
ESEM	Environmental scanning electron microscopy
f-BNNS	Functionalized boron nitride nanosheets
g	Gravitational acceleration
GPa	Gigapascal
H	Hardness
h-BN	Hexagonal boron nitride

IL	Ionic liquid
k	Boltzmann constant
K	Thermal conductivity
LFD	Laser flash diffusivity
NMR	Nuclear magnetic resonance
NPs	Nanoparticles
OP	Over-potential
OTS	Octadecyltrichlorisilane
pK_a	Acid dissociation constant
p-TC	p-toluoyl chloride
PVB	Polyvinyl butyral
PEG-D	Polyethylene glycol dithiol
PSTTR	Phase sensitive transient thermoreflectance
R	Resistance
SEM	Scanning electron microscopy
SIMS	Secondary ion mass spectrometry
T	Temperature
TD	Terepthalic dihydrazide
TEM	Transmission electron microscopy
TGA	Thermogravimetric analysis
TIM	Thermal interface material
TSC	Thiosemicarbazide

XPS	X-ray photoelectron spectroscopy
vdW	van der Waals
v_s	Settling velocity
2-MBC	2-mercapto-5-benzimidazole carboxylic acid
4-ABT	4-aminobenzenethiol
4-BBC	4-bromobenzoyl chloride
4-CBC	4-cyanobenzoyl chloride
4-MBA	4-mercaptobenzoic acid
4-MPA	4-mercaptopropionic acid
4-MT	4-mercaptotoulene
4-NBC	4-nitrobenzoyl chloride
α	Thermal diffusivity
$\dot{\gamma}$	Shear rate
ε	Dielectric constant
ε_o	Permittivity of free space
μ	Viscosity
μ_0	Zero frequency viscosity
ρ	Density
υ	Poisson`s ratio
ψ	Surface potential

TABLE OF CONTENTS

Page

LIST OF FIGURES

Page

LIST OF TABLES

CHAPTER I

INTRODUCTION

1.1. Objectives

The main objective of this proposed work is to develop next generation thermal interface materials (TIMs) for efficient thermal management in electronic systems. Up on this objective, metal-based thin film nanocomposite TIMs involving functionalized boron nitride nanosheets were fabricated; microstructurally, thermally and mechanically characterized; and finally their reliability, performance and lifetime against corrosion were examined.

The insufficient dissipation of heat is a critical problem in electronic systems, which significantly reduces their performance. As the devices, such as CPUs and integrated circuits, have been smaller, more sophisticated, and generating higher levels of power, they dissipate much larger amounts of heat. For instance, while Intel Pentium® II 233 MHz processor had a dissipation rating of 34.8 W, this value was 165 W in dual-core Intel Xeon® 7041 processor.[1] As they generate higher amounts of power, effective thermal management of these electronic circuits gains utmost importance in terms of lifetime and reliability. Thermal interface materials (TIMs), integral parts of the electronic systems, act as a bridge between heat sources (CPU/IC) and heat sinks to maximize the apparent contact area at the interface, and help transfer the maximum amount of heat. Thus, it is a significant task to keep the TIMs up to date with the advances in the other components of the electronic systems.

1.2. Background and Approach

1.2.1. Background

A thermal interface material (TIM) is a crucial component of an electronic system that is responsible for efficient cooling and thermal management. With the fast-paced technological advances in recent decades, there has been a substantial increase in the power generation capacity of integrated circuits (IC) and CPUs. However, current TIMs have not kept up with the advances in these electronic components and the thermal limitations of these components have been a critical factor that hinders the transition from prototype to product in several applications including digital and RF components. Hence, there is an urgent need to develop TIMs to improve the thermal management and reliability of electronic systems.

An electronic system consists of several components as illustrated in Figure 1a. The most delicate component of the system is the chip, which is protected by a lid causing an indirect contact with the heat sink. Two types of thermal interface materials are incorporated to the system: TIM 1 and TIM 2. They are designed to conform with the lid-chip and lid-heat sink interfaces, respectively. Figure 1b demonstrates the contact surfaces of the two components. When these two nominally flat surfaces come together at a typical material interface, the solid-solid contact area is limited to 1-2% of the apparent contact area due to surface asperities, which is an inhibiting factor for efficient heat transfer. The TIM is placed at this interface to increase the contact surface by fully covering the surface asperities and maximize the area of contact. The TIM must be mechanically compliant to achieve this task, and it also requires being thermally conductive for efficient heat transport. Figure 2 depicts the surface RMS roughness values of two heat sinks (a-b) and a CPU (c), which were disassembled from personal computers and analyzed by atomic force microscopy (AFM). While the RMS roughness of the CPU was near 50 nm, it was more than three times higher in the heat sink surfaces. As such, the TIM placed at a heat source-heat sink interface must conform to various roughness values of the mating surfaces.

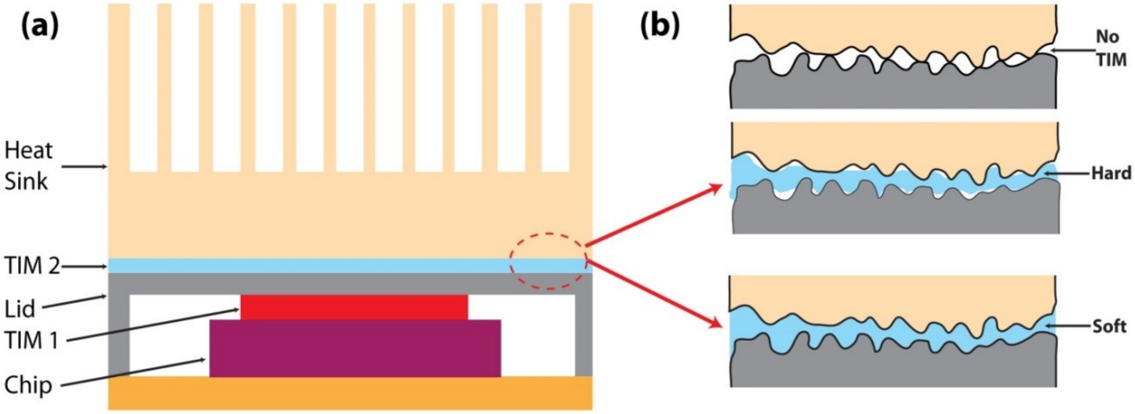

Figure 1. a) Schematic view of a typical electronic system and its components, and b) placement of TIMs between two mating surfaces

1.2.2. Current TIMs and Limitations

TIMs come with varying properties such as thermal conductivity/resistivity, stiffness, temperature range and ease of application. Thermal greases, polymer-based composites, phase change materials and solders are commonly used as thermal interface materials.

In thermal greases, conductive fillers are dispersed in silicone or a hydrocarbon oil to form a paste. In current paste formulations, several types of fillers such as diamond powder,[2] silver,[3] copper,[4–6] carbon nanotubes (CNT)[7,8] and aluminum nitride[9–11] have been used. The thermal properties of the composite paste are described by the type, concentration and morphology of the filler. The common thermal conductivity values of thermal pastes differ from 0.5 to 7 $W.m^{-1}.K^{-1}$, while the thermal resistances changing from 10 to 30 $K.mm^2/W$.

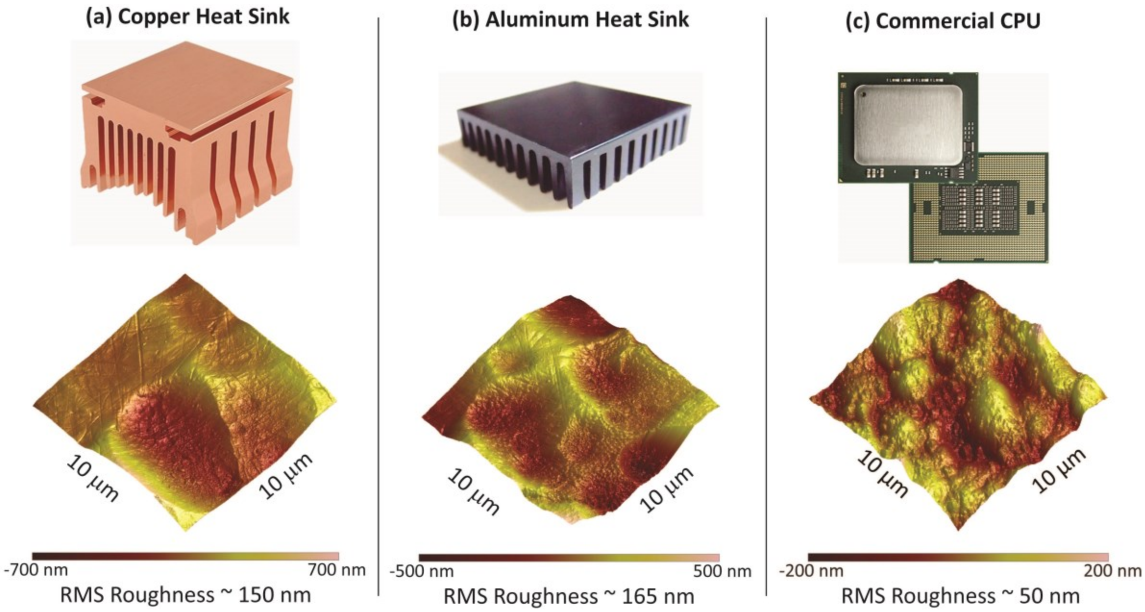

Figure 2. Surface RMS roughness values of a-b) copper and aluminum heat sinks, and c) a CPU, which were disassembled from personal computers and analyzed by atomic force microscopy (AFM)

In polymer-based TIMs, the composite is formed by adding the thermally conductive filler to a polymer matrix. Similar to the thermal pastes, copper, silver, aluminum nitride particles,[1,10,12–17] and CNTs[18–20] have been used as fillers in polymers such as epoxy, polyvinyl chloride and polyacrylate. Graphite[21] and graphene[22] have also been recently used as novel type of fillers. Typical thermal conductivity and resistance values of the polymer-based TIMs vary within a range of 0.5-5 $W.m^{-1}.K^{-1}$, and 3-80 $K.mm^2/W$.

Another class of TIMs has been designed with solders, which have relatively lower melting points than most metals. Solder TIMs can flow and spread over the interface, and introduce a small thermal contact resistance. While Tin/Lead alloys have extensively been used,[23] some other elements such as bismuth and antimony[24–27] have also been added to solder alloys depending on specific needs. Thermal conductivity of solder alloys range from 20 to 80 $W.m^{-1}.K^{-1}$.

Phase change materials (PCMs) are most commonly based on paraffin, polymer or copolymer in which the conductive filler are suspended. The PCMs are solid TIMs at room temperature and turn into liquid at the operating temperature. Therefore, it flows into the voids and reduce the thermal contact resistance similar to solder TIMs. Low melting alloys such as the systems based on bismuth, indium, gallium, lead and mercury are a class of PCMs due to their low melting points.[28,29] However, some of these alloys are not usually preferred due to toxic effects.[1] PCMs have thermal resistances from 1 to 10 $K.mm^2/W$.[30]

The limitations to the current TIMs are as follows: Although solder TIMs have relatively high thermal conductivity/low thermal resistance coupling, high stiffness of these TIMs leads to delamination and chip cracking when the difference in thermal expansion coefficients of the two mating surfaces is large. On the other hand, polymer-based composite TIMs are softer, but their relatively low thermal conductivity and poor heat transport across interface results in an inefficient operation. Thermal greases are difficult to apply and remove, and excess grease may flow out of joint and contaminate the other components.[31] While PCMs introduce relatively low thermal resistance, frequent phase change might induce reaction with the mating surfaces and damage them. In addition formation of intermetallic compounds and corrosion due to oxidation may lead to lower performance in the long run and even fail the device.[29,31]

As such, next-generation TIMs are in need to overcome the abovementioned problems. This work aims to develop novel TIMs with thermal resistivity lower than solders and PCMs, and elastic modulus close to or less than epoxy-based composite TIMs.

1.2.3. Approach for Development of Metal-based Nanocomposite TIMs

There are two potential routes to overcome the limitations mentioned above, and develop TIMs that can satisfy stringent operational conditions: (i) further improving the thermal properties of elastomer-based TIMs and (ii) improving the mechanical compliance of solder (or metal)-based TIMs. While most research efforts in this field are on enhancing the thermal properties of polymer-based composite TIMs, we were interested in the other approach: improving the mechanical compliance of solder alloys or metals by incorporating soft ligand functionalized nanomaterials as illustrated in Figure 3a. By this way, we propose that the stiffness will be reduced due to presence of soft organic ligands and nanoparticles, and the thermal conductivity values will remain high due to the metal matrix and selection of high thermal conductivity filler.

We initially began with the selection of filler that will meet the expectations. Graphene is a novel type filler widely used in enhancement of the thermal properties of TIMs.[22] However, recent studies have shown that graphene is damaged in presence of various metals.[32,33] For this reason, the idea of developing a metal/alloy-graphene composite TIMs was not feasible. Compared to graphene, Boron Nitride nanosheets (BNNS), also known as white graphene because of its similar chemical structure (Fig. 3b[34]), display much better thermal and chemical stabilities,[35] and have extremely high in-plane thermal conductivity (300-2000 W.m^{-1}.K^{-1}).[35,36] Therefore, BNNS was selected as the building block nanomaterial.

BNNS were exfoliated from the commercially available h-BN flakes. Mechanically assisted cleavage resulted in breaking the interlayer van der Waals bonds, and eventually mono- or few-layered nanosheets were obtained (Fig. 4a). The next step

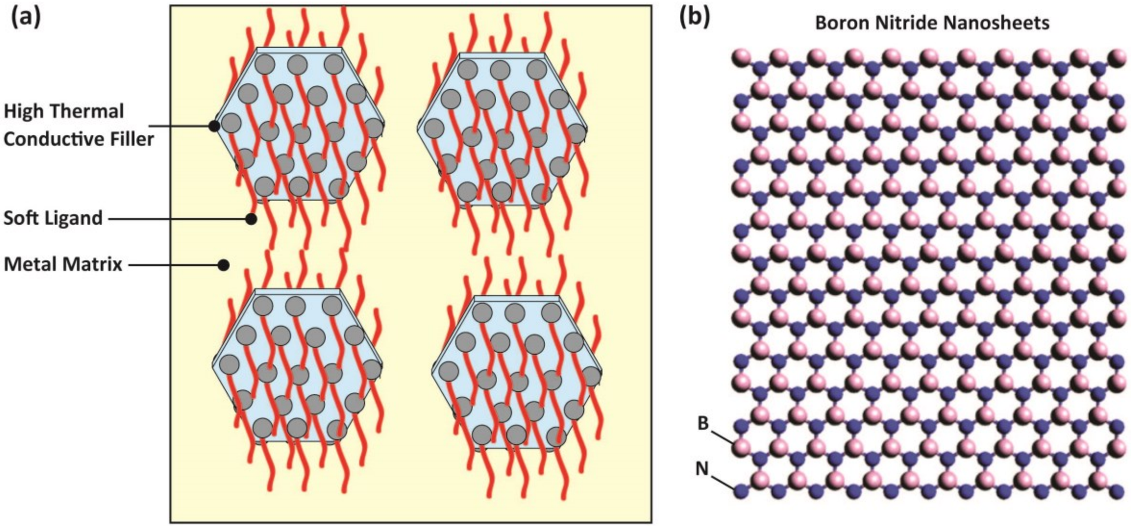

Figure 3. Schematic illustration of a) dispersion of soft ligand functionalized nanoparticles in metal matrix and b) boron nitride nanosheets.[34]

was the functionalization of the BNNS with organic ligands since these ligands are capable to reducing the effective stiffness of the nanomaterials, and maintain the homogeneity of filler nanomaterials when they are dispersed in the matrix.

Functionalization was performed through Lewis acid-base reactions,[37] and with ligands having amine/thiol groups.[38,39] While functionalization was achieved with various ligands, we initialized the investigation with thiosemicarbazide (TSC), which contains an amine group to link to boron groups of BNNS and a carbonothioyl group (or thiol) that can react with metals. The functionalization and characterization results of thiosemicarbazide and the other ligands will be discussed in Chapters III and IV, respectively.

Upon functionalization of the BNNS with the appropriate ligands, the next task was to disperse the functionalized BNNS (f-BNNS) in a solder (or metal) matrix using mechanical agitation and ultrasonic dispersion. Since the matrix has very high surface energy, the mixing and dispersing low surface energy BNNS in the metal matrix was very challenging. Moreover, traditional molten metal mixing and agitation method was employed. However, producing the desired metal-based nanocomposite TIMs was not feasible with this method because of the high melting temperature of the metals (solder) and the presence of volatile organic linker molecules. Therefore, alternative approaches were searched and a breakthrough in producing nanocomposites with f-BNNS and metal matrix was introduced. This breakthrough was enabled by an electrocodeposition approach involving metal cations and f-BNNS as indicated by Figure 4b. It was shown that for the electrocodeposition approach, the functional groups on BNNS strongly influence morphology and nanostructure, mechanical properties, and thermal properties of f-BNNS-metal nanocomposites. In other words, we can adjust mechanical and thermal properties of BNNS by altering architecture, chemistry, and coverage (or concentration) of ligands. The fundamentals of electrodeposition method will be given in the next chapter.

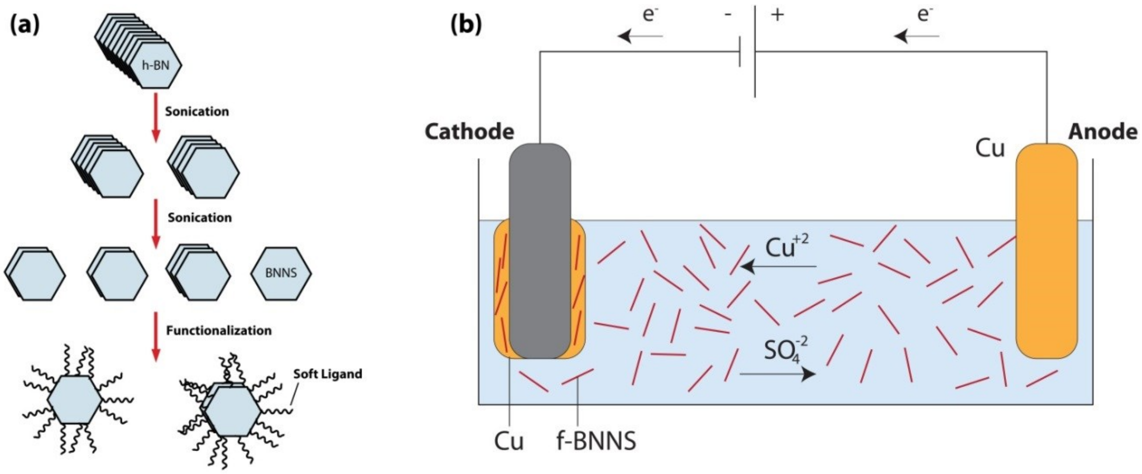

Figure 4. a) Exfoliation of BN nanosheets from h-BN powder, and functionalization of the nanosheets with organic soft ligands, and b) schematics of electrocodeposition of Copper atoms and functionalized BNNS.

Copper was initially selected to be the metal matrix due to its well-known high thermal conductivity, low cost and availability. Then, silver was chosen to be the alternative metal since it has higher thermal conductivity and mechanical compliance than those of copper.

1.3. Dissertation Outline

This study was divided into six chapters: Chapter I provides a general introduction of the thermal interface materials such as the need for TIMs in the industry, current TIMs and their limitations, and our approach on developing the next-generation TIMs. Chapter II describes the fundamentals of electrodeposition method that was used in fabricating the metal-based nanocomposite TIMs. Chapter III includes a comprehensive characterization of copper-based hybrid nanocomposite TIMs involving the ligand, thiosemicarbazide. Chapter IV further enhances the investigation to other organic ligands types and contains electrochemical test results of the hybrid nanocomposite TIMs, which informs the reader about how the corrosion behavior of pure matrix is affected by nanoparticles and organic linkers. In Chapter V, the starting metal matrix, copper, is replaced with silver, and similar microstructural and thermomechanical characterization of Ag-based nanocomposite TIMs are performed in presence of various ligands. Finally in Chapter VI, the summary and conclusions are presented, and the possible future work is discussed.

In Appendices, the manuscripts of the author`s two papers are provided: In Appendix A, pH-responsive supramolecular solution systems and their potential application in hydraulic fracturing, and in Appendix B, tribological investigation of inorganic nanoparticle-based ionic liquid nanofluids are discussed.

CHAPTER II

FUNDAMENTALS OF ELECTRODEPOSITION

2.1. Introduction

Electrodeposition is the process of electroplating, in which electric field is utilized to reduce metal cations dissolved in an electrolyte solution to form a metal coating on an electrode. Both electrolytes, cathode and anode, are immersed in the electrolyte that contains the salt of the metal, i.e. the metal ions, to be electrodeposited.[40] Figure 5a shows a typical electrodeposition of copper onto a metal cation where $CuSO_4$ is the copper salt providing the ions, which help the atomic migration from anode to cathode and maintain the electrical conductivity of the solution. Cu atoms are oxidized at the anode to form Cu^{2+} ions by losing two electrons and join the electrolyte. Meanwhile, Cu^{2+} cations are reduced at the cathode and deposit onto it as metallic Cu atoms. Hence, the metallic Cu atoms cover the surface of the cathode[41]. Eq.1 below shows the general form of the reaction: (1) the reaction from left to right is the oxidation reaction that occurs at the anode-solution interface, and (2) the reaction from right to left is the reduction reaction at the solution-cathode interface where two electrons are consumed.

$$Cu \rightleftharpoons Cu^{2+} + 2e^{-} \qquad [1]$$

Next section will include brief summaries of basics electroplating such as potential of electrodes, electrodeposition mechanism and its atomistic aspects, growth phases of the deposit, effect of additives and materials aspects. Moreover, the last section of this chapter will discuss the optimization of the experimental conditions that was performed in this project.

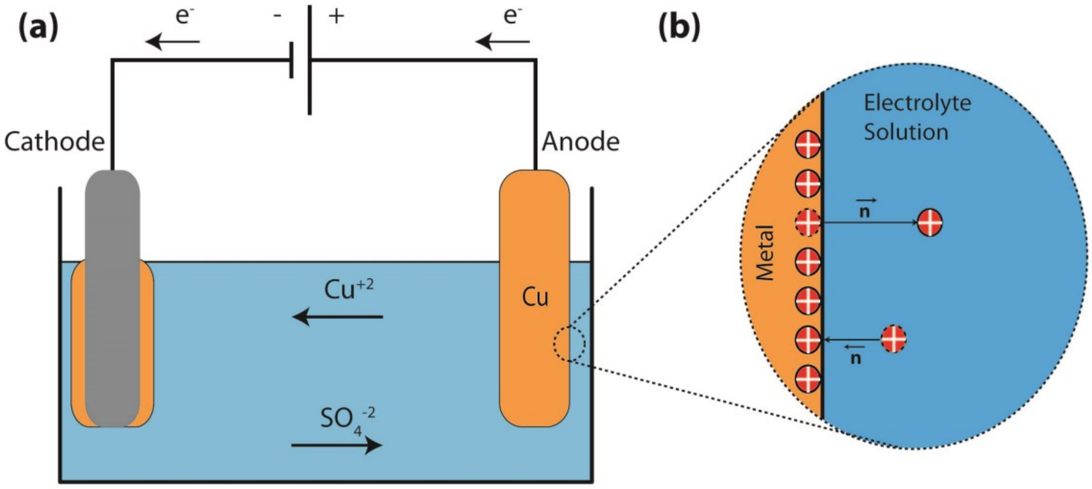

Figure 5. a) Electrodeposition of copper with $CuSO_4$ electrolyte solution and electric potential, and b) metal-solution interphase equilibrium in absence of electric current

2.2. Fundamentals of Electrodeposition

2.2.1. Electrode Potential

Electrode potential is a phenomenon that occurs at an electrode-electrolyte interface due to the transfer of charged species in absence of electric current. When a metal M is submerged in an electrolyte containing M^{z+} ions, ion exchange occurs between the solution and the metal crystal lattice, as demonstrated in Figure 5b. For example, if the ion transfer from the crystal lattice to the solution is higher the other way, metal acquires negative charge in the vicinity of the interface due to excess electrons. This attracts the M^{z+} ions and in the solution and the ion transfer rate increases from the solution to the metal lattice. Charge interactions at the interface bring the ion transfer to equilibrium state ($\vec{n} = \overleftarrow{n}$). At the dynamic equilibrium, the oxidation/reduction reactions occur at the metal-solution interface (Eq. 1). The potential of an electrode, i.e. standard electrode potential, can be measured via electrochemical cells.[41] The potential at a metal/ion interface is dependent on the activity of metal ions, which is a function of ion concentration in the solution. The effect of electrolyte solution concentration on the properties of nanocomposite TIMs will be discussed in Section 2.3.

2.2.2. Kinetics and Mechanism of Electrodeposition

When electric current passes through an electrode, it gains a new potential state from its standard equilibrium potential. This is called the over-potential and defined as the difference between the potentials in presence and absence of electric field ($OP = E(I) - E$). Large values of over-potential give rise to an exponential increase in the current density, i, which is the current per unit area of the electrode surface ($i = I/A$).[41]

The abovementioned potential-current density relationship is valid at slow deposition processes and there is a maximum current density limit which is a function of solution concentration, diffusion coefficient of the metal ions, number of electrons and the layer thickness.[42] The diffusion layer thickness is determined by Nernst diffusion layer model, which assumes that the solution concentration linearly influences the layer thickness up to a particular distance from the interface, beyond which the concentration effect start disappearing. Stirring of the solution can help increase this thickness as we did in our electrodeposition experiments. Moreover, deposit thickness is dependent on the duration of the electrodeposition as well as the current density and the solution concentration, which is given in the equation below;[41]

$$h = \frac{Zit}{\rho} \qquad [2]$$

where Z is proportionality constant, i is the current density, ρ is the deposit density and t is the time of deposition. The time effect of electrodeposition thickness was verified via experiments as shown in Figure 8.

Another factor affecting the properties of the electrodeposited metal is the source of current. When the DC source is replaced with an AC source, it enables the modification of diffusion layer. The abovementioned Nernst diffusion model is modified by pulsating current that leads to pulsation of the ion concentration in the solution.[43] Pulse deposition increases the uniform distribution, brightness and leveling of the deposition.[41,44]

2.2.3. Atomistic Aspects

Electrodeposition facilitates the transfer of metals ions (M^{z+}) from the solution to the metal lattice by providing z number of electrons to the electron gas in the metal, and the deposit layer grows on the cathode surface. Differing from the ideal surfaces, the real substrate surfaces, as the ones we used in this study, contain various defects including impurities, dislocations, grain boundaries, kinks, steps and vacancies. They have surface roughness while the ideal surfaces are considered to be smooth. The final state of a metal ion is described as an adatom (or adsorbed atom) that is attached to a kink site.[45] Settling of the adatoms at a kink site are achieved via one of the two mechanisms: (i) *Step-edge ion transfer (Fig.6a)*, where the adatom is either directly transferred to a kink site or diffuse along a step edge (in one step), and (ii) *Terrace-ion transfer (Fig.6b)*, where the adatom, which was added to the flat terrace, travels to the step edge (phase 1) and diffuses along the step edge towards the kink site (phase 2). Since the defective sites are energetically favorable growth locations, the adatoms tend to migrate towards these sites.[40] Lorenz et.al[46] and Mehl and Bockriz[47] have reported the initial theoretical and experimental studies of this type of surface diffusion.

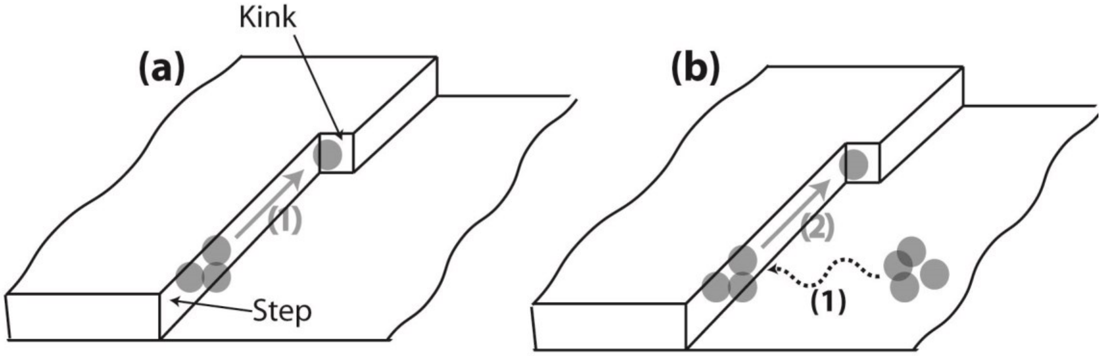

Figure 6. Electrodeposition in atomistic level: a) Step-edge ion transfer, and b) terrace ion transfer.

2.2.4. Growth Mechanism

It is shown in Figure 7 that one-dimensional layer growth and three-dimensional nucleation-coalescence growth are two principle growth mechanisms of electrodeposition.[40,48] In the former growth mechanism the metal crystals form layer-by-layer structure, which is also called the thin step growth (Fig. 7a), whereas in the latter mechanism, the deposit is formed by accumulation of 3-D crystallites (Fig. 7b). Initially, nucleation starts and it is followed by growth of the crystallites. As they increase in size, they form network structures and eventually evolve into a uniform deposit. The deposit formation creates a columnar structure with various grain sizes, which are usually fine grains at close proximity to the substrate and coarser ones at further distances. The variation in the grain size can be due to surface energies of the grains where low energy grains grow faster than the high surface energy ones leading to increase in grain size with thickness.

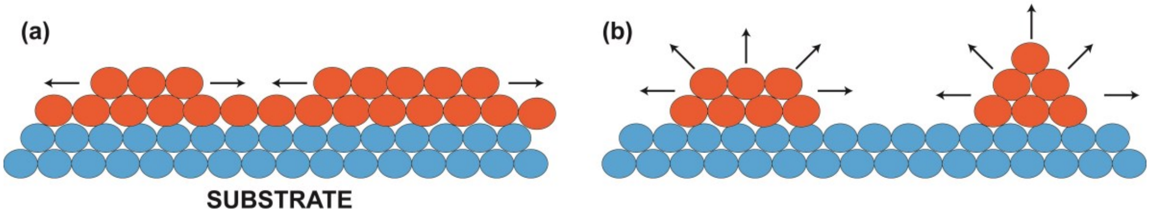

Figure 7. Growth mechanism of electrodeposition: a) 1-D layer growth, b) 3-D nucleation-coalescence growth

2.2.5. Influence of Additives

When additives are used in the electrodeposition process, they function as adsorbed substances on the cathode surface and influence deposition kinetics and growth mechanisms. Adsorption of additives changes various surface properties such as the number of growth sites of the surface, surface diffusion of adatoms and concentration of adatoms on the surface.[41] They diminish the diffusivity of the atoms through the interface, nevertheless this decrease results in the increasing concentration of adatoms at steady state, which may eventually increase 2-D nucleation growth between diffusing adatoms.[41]

Based on the above given knowledge of electrodeposition, a systematic investigation of optimum experimental conditions giving the most robust nanocomposite TIMs was completed and the results were given in the next section.

2.3. Investigation of Optimum Experimental Conditions

As the functionalization reaction of the BNNS was well-established, thiosemicarbazide (TSC) was considered to be the main organic ligand for systematic study. Numerous copper-based thin film nanocomposite TIMs (Cu/f-BNNS nanocomposite TIMs) were fabricated to determine the optimum experimental conditions in producing smooth and homogenous TIMs. The experimental parameters were selected to be electrodeposition time, filler (f-BNNS) and electrolyte metal salt ($CuSO_4$) concentrations, current density and concentration of PEG-Dithiol as free ligand additive. Since the systematic investigation required characterization of TIMs samples produced at several conditions and we had only one potentiostat, DC power sources were initially used as the main source of electric current in order to produce multiple samples at the same time. The potentiostat was used as AC the power source when the optimum conditions were determined.

Figure 8 demonstrates the produced film thicknesses at various electrodeposition times. The film thickness linearly increases with electrodeposition time. At a current density of 5 A/dm^2, unstable thin films or sometimes no film formation was observed below 45 minutes. Then, the current density was gradually increased to 12 A/dm^2, and nanocomposites with several hundreds of thicknesses were obtained. Since the laser flash diffusivity system that we used in thermal conductivity measurements, is set to measure samples having thickness of 100 µm and above, 60 minutes of electrodeposition time was decided for further electrodeposition experiments to obtain 100-200 µm thick samples.

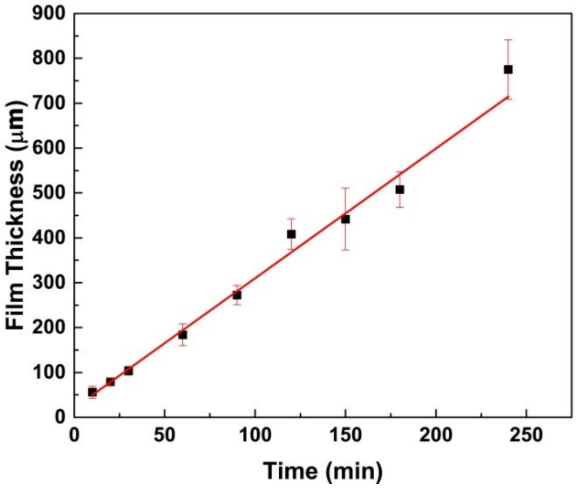

Figure 8. Effect of electrodeposition time on film thickness (R^2=0.988)

Once the electrodeposition time required to produce nanocomposite thin films at desired thicknesses was determined, the influence of other experimental parameters on surface structure, mechanical and thermal properties of metal nanocomposites was investigated. As the second parameter, the filler (f-BNNS) concentration in the electrolyte solution was increased up to 3.8 wt.% (above which no film formation was observed), starting from 1.3 wt.%. The current density was maintained at 12 A/dm^2.

Although robust thin film nanocomposite TIM samples were achieved at several filler concentrations, we selected 1.25 wt.% as the optimum concentration since a high thermal conductivity value (>200 W/m.K) was obtained at this value. As a next step, the various electrolyte $CuSO_4$ concentrations were used for sample fabrication, and it was observed that the concentrations above 1.5 M resulted in very rough surface morphologies despite these samples` having high thermal conductivities. Thus, in the next step where the nanocomposite samples were produced at varying current densities, the electrolyte solution with a 1.25 wt.% f-BNNS and a 1.0 M $CuSO_4$ concentrations was utilized. The thermal conductivity results of the samples produced at current densities within a range of 5-12 A/dm^2 were recorded, above which the sample surfaces were very non-uniform and rough, which led to inaccurate thermal measurements. Smooth nanocomposite samples were obtained at reduced current densities. However, it did not significantly alter the surface morphology and the current density of 12 A/dm^2, which is the current density limit of the electrodeposition, was kept constant in the last step. Finally, an external polymer additive, polyethylene glycol dithiol (PEG-D), was added to the electrolyte solution at trace amounts to analyze its effect to the thermal and mechanical properties of the nanocomposite TIMs. As a result of the parametric study, high thermal conductivity nanocomposite TIMs were obtained in presence of PEG-Dithiol. Further experimental details of microstructural and thermomechanical characterization of Cu/f-BNNS thin film nanocomposite TIMs will be discussed in Chapter III and Chapter IV.

CHAPTER III

NEXT-GENERATION THERMAL INTERFACE MATERIALS WITH ULTRA-LOW THERMAL RESISTANCES

3.1. Introduction

The removal of heat dissipated during the high power-density operations is typically achieved by the transfer of heat by conduction from a heat source to a heat sink.[49,50] When these two surfaces are brought together in the absence of any TIM, surface roughness - which all engineered objects have - causes the thermal contact to occur only at discrete junctions. The resultant thermal contact is characterized by nano- and micro-junctions surrounded with a large volume fraction of interstitial air or pores. Such pores reduce the effective thermal conductivity of the contact region, often termed as the thermal contact resistance. In addition, the heat transfer across the contact junctions is further reduced owing to the thermal boundary resistance stemming from phonon or electron scattering processes depending on the nature of materials comprising the interface.[51] Moreover, when the size of contact junctions becomes comparable with the mean free path of the energy carriers, their transport is even further hindered through the quantum confinement effect and changes in phonon/electron dispersion.[52] One potential approach for overcoming these problems is to use TIMs that enable a better thermal contact by conforming to the topographical features of the coupling surfaces via flow or deformation without introducing a significant conductive resistance into the system, and by reducing the sharp acoustic mismatch between air and solid surfaces.

Currently, thermal greases, polymer-composites, and solders are the most commonly used types of TIMs. In thermal greases, thermally conductive fillers are dispersed in a viscous fluid such as silicone oil, sodium silicate, or hydrocarbon oil to form a paste.[53] In polymer-composite TIMs, the matrix is an elastomer instead of a viscous fluid, such as epoxy or polyurethane.[54,55] In both types of TIMs, a high thermal conductivity material such as graphene, carbon nanotubes, diamond powder, silver particles, and copper particles is used as a filler.[56–62] Thermal grease and polymer-composite TIMs typically have bulk thermal conductivity values in the range of 0.5 W/(m.K) to 10 W/(m.K) at room temperature.[63] These TIMs are compliant, but their low thermal conductivity and poor thermal transport across the boundaries pose a significant thermal barrier to high-power-density operations. In addition, these TIMs also suffer from pump-out and dry-out issues, when subjected to thermal cycling and elevated temperatures, which degrades their performance. Solder TIMs, which are fusible metal alloys with low melting temperatures, have a thermal conductivity of 20 to 80 W/(m.K).[30,63] While solder TIMs offer relatively high thermal conductivities, solder TIMs – similar to other low-melting-temperature metals - tend to have a high coefficient of thermal expansion (CTE). For instance, the CTE of indium is 29 ppm/K while the CTE of silicon and copper is 2.4 ppm/K and 16.4 ppm/K, respectively,[64] making them prone to thermally-induced high-stress failure. For a typical bond line thickness of 50 μm, the total thermal resistance is on the order of 5 to 30 mm^{2}K/W for thermal greases, polymer TIMs, and solders TIMs.[65] Another important type of TIM is highly oriented pyrolytic graphite, which has very high thermal conductivity along the in-plane direction

(600-1700 W/m^2.K) and low thermal conductivity in the out-of-plane direction (10-20 W/m^2.K). However, most thermal management applications require a high thermal conductivity in the out-of-plane (z-) direction between heat spreader and sink. While graphene-based TIMs achieved thermal resistances as low as 1.5×10^{-2} mm^2.K/W at nanoscale,[66,67] their device scale forms and highly oriented pyrolytic graphite sheets with a thickness of 50-100 μm have been reported to result in a total resistance in the order of 20 mm^2.K/W.[68] The delamination and flaking off are other challenges associated with pyrolytic graphite sheets.

There are two potential routes for reducing the total thermal resistance of TIMs that are needed to satisfy stringent thermal needs of emerging advanced applications: either by further improving the thermal properties of a compliant matrix, or by further improving the mechanical properties of a high-thermal-conductivity matrix. Currently, the majority of research is focused on the former approach. As ours is a novel approach aiming at the enhancement of the mechanical properties of the metal matrix, we develop a new class of nanocomposite TIMs by covalently integrating boron nitride nanosheets (BNNS) functionalized with soft organic linkers and a copper matrix. Here, BNNS is selected as filler because of its extremely high in-plane thermal conductivity (300-2000 W/(m.K)), low coefficient of thermal expansion, and superior thermal and chemical stability.[69–72] Copper is a well-known matrix material with high thermal conductivity.

3.2. Materials and Methods

3.2.1. Materials

Hexagonal Boron Nitride, h-BN (98%, APS: 0.5 micron), produced by the reaction of boric acid and ammonia at 900˚C ($B(OH)_3 + NH_3 \rightarrow BN + 3H_2O$) was received from Lower Friction-M.K. IMPEX Corp, (Mississauga, Ontario, Canada). Sulphuric Acid (H_2SO_4, ACS reagent, 95.0-98.0%), Copper (II) Chloride ($CuCl_2$, 99%) and Copper Sulfate pentahydrate ($CuSO_4.5H_2O$, ≥98%) were obtained from Sigma Aldrich (St. Louis, MI). Thiosemicarbazide (CH_5N_3S, >98%) and 1,3,4-Thiadiazole-2,5-dithiol ($C_2H_2N_2S_3$, >95%) were obtained from TCI America (Portland, OR). N-methlyl-2-pyrrolidone (C_5H_9NO, 99%) (NMP) was obtained from VWR (Radnor, PA). Copper sheets were obtained from McMaster Carr (Elmhurst, IL) and Aluminum substrate was obtained from Metals Depot (Winchester, KY). Silicon wafers (Silicon <100> P/Boron, >5000 ohm-cm, doubleside polish, <10 Angstrom R_a) were received from University Wafer (Boston, MA)

3.2.2. Synthesis and Characterization of f-BNNS

The chemical interactions of TMCS with silica materials (i.e., quartz and silica aerogel) were characterized by attenuated total reflectance-Fourier transform infrared (ATR-FTIR) spectroscopy. ATR-FTIR spectra were measured using an IRPrestige-21 (Shimadzu Corp., Kyoto, Japan) system and analyzed using IRsolution version 1.40 (Shimadzu Corp., Kyoto, Japan) software.

Covalent functionalization of BNNS was achieved by reacting exfoliated BNNS with thiosemicarbazide (>98%) in NMP (1:10:100 in weight). The reaction took place at 170 ˚C for 30 hours under nitrogen flow. The obtained product was dialyzed in NMP for 10 hours to remove the unreacted ligands, followed by centrifugation at 3500 rpm for 15 minutes. Next, the supernatant was removed; the precipitate (functionalized BNNS, f-BNNS) was dried at 75 ˚C in a vacuum furnace for further removal of the remaining NMP from f-BNNS powder.

Nuclear magnetic resonance spectra in solid state were obtained on AVANCE-400 instrument. ^{11}B shifts are reported relative to $BF_3(OEt_2)$. High-power proton decoupling was applied with a 90° pulse time of 5 μs, a contact time of 5 ms, and a recycle delay of 8 s. Approximately 50 mg of the sample was packed into 5 mm Wilmad thin wall precision NMR sample tube 8" and loaded in to 7 mm CP-MAS rotors. The rotor spinning speeds were 4 kHz. All NMR measurements were carried out at 25 °C. High resolution Transmission electron microscopy was performed in a JEOL ARM200F with electron probe aberration (Cs) corrector operated at 200 kV, also equipped with an Oxford Instruments X-MaxN 100TLE 100 mm^2 detector for Energy dispersive X-ray spectroscopy (EDS) and a Gatan Enfina spectrometer for electron energy loss spectroscopy (EELS). High angle annular dark field (HAADF) and annular bright field (ABF) Scanning transmission electron microscopy (STEM) imaging techniques were used to characterize the nanostructural morphology of the BNNS samples.

3.2.3. Fabrication of Thin Film Nanocomposite TIMs

Thin film nanocomposite TIMs were grown on aluminum sheets and silicon wafers. The aqueous electrolyte solutions were prepared by varying concentrations of $CuSO_4.5H_2O$, 1.8 M H_2SO_4, a trace amount of $CuCl_2$, and various concentrations of f-BNNS. Each solution was briefly sonicated for homogenous dispersion of f-BNNS, and transferred to an electroplating cell. A pure copper sheet (>99%) and a substrate were connected to anode and cathode, respectively. The electrical power source was a Nuvant Powerstat05 Potentiostat (Nuvant Systems Inc., Crown Point, IN). The electrodeposition was carried out at a current density of 0 to 12 A/dm^2 and AC frequency of 950 Hz with 30% off time. The main advantage of the pulse electrodeposition is the ability to change experimental parameters such as pulse peak current density and on-/off-time in pulse electrodeposition. Manipulation of these parameters enabled us to better control the homogeneity of nanocomposite TIMs.

3.2.4. Characterization and Performance Evaluation of TIMs

Nanoindentation was used as the main technique for mechanical characterization. Hardness and reduced elastic modulus values were measured via a Hysitron TI 950 Triboindenter (Hysitron Inc., Minneapolis, MN). A Berkovich tip with a well-defined geometry was used for indentation and forty measurements were taken from each sample for statistical analysis.

Thermal properties of thin film nanocomposite TIMs were measured via various techniques. A Modulated Q20 DSC (TA Instruments, New Castle, DE) was used to measure specific heat capacity of the samples. Thermal diffusivity measurements were performed via a DLF-1200 Laser Flash Diffusivity System (TA Instruments, New Castle, DE). The density of samples was determined gravimetrically. These values were employed in equation 3 of supporting information to obtain thermal conductivity of the samples. Further, PSTTR measurements were done at NREL, Colorado to determine thermal resistance of the samples and detailed information on this is provided in supporting information.

3.3. Results and Discussion

3.3.1. Characterization of Functionalization

The first step in producing metal/organic/inorganic nanocomposite TIMs was the functionalization of the boron nitride nanosheets with a ligand that is capable of reducing their effective stiffness and covalently linking BNNS with the metal matrix. Towards this end, we relied on thiosemicarbazide (TSC), which contains an amino group that can react with electron deficient boron groups of BNNS, and a carbonothioyl group (or its tautomer, thiol) that can react with copper. To gain insights into the reaction of TSC with BNNS, first, solid state ^{1}H MAS (Magic-Angle Spinning) NMR (Nuclear Magnetic Resonance) was used (Fig. 9a). The major changes were observed as disappearance of peak at $\delta = 5.01$, this is hydrogen in the hydroxyl group on an edge B atom. This indicates reaction with TSC as a condensation reaction. This was also supported by ^{11}B MAS NMR spectrum for BNNS and f-BNNS shown in Figure S3. No change was observed in basal B atoms16 at $\delta = 20.8$, but prominent change was recorded on tetra coordinated B atoms at δ = -25.7 to -17.2 indicating the site of reaction. Further studies with Raman spectroscopy revealed the disappearance and major shifts at wavelengths 806 cm^{-1} (NH_2 wagging and CS stretching), 1008 cm^{-1} (NN stretching and CN stretching), 1172 cm^{-1} (NN stretching), 1526 cm^{-1} (NH bending), 1630 cm^{-1} (NH_2 bending), and 3258 cm^{-1} (NH_2 stretching) from the TSC spectra upon the reaction with BNNS (Fig. S4). These findings demonstrate that the most notable changes on TSC occur on the amino group. On the other hand, no significant change on the peaks associated with the primary amide was observed (see Supporting Information for details), proving that the functionalization reaction indeed takes place between the amino group of TSC and BNNS.

The comparison of high-resolution TEM micrographs of BNNS before and after the functionalization step revealed that the functionalization occurs at the edges rather than on the basal plane (Fig. 9b), which is preferred in 2-D materials to prevent the loss of intriguing properties. The complementary x-ray photoelectron spectroscopy (XPS) studies showed that some fraction of carbonothioyl was converted to tautomeric thiol upon the functionalization reaction (Fig. 14). When we put all of these pieces together, the picture emerges that the electron-rich amino group of TSC reacts with hydroxylated and tetra coordinated borons of BNNS either via condensation or Lewis acid-base reaction (Fig. 9c). In this reaction scheme, the carbonothioyl (or its tautomer, thiol) group sticking out of the f-BNNS is available for coordination bonding with copper.

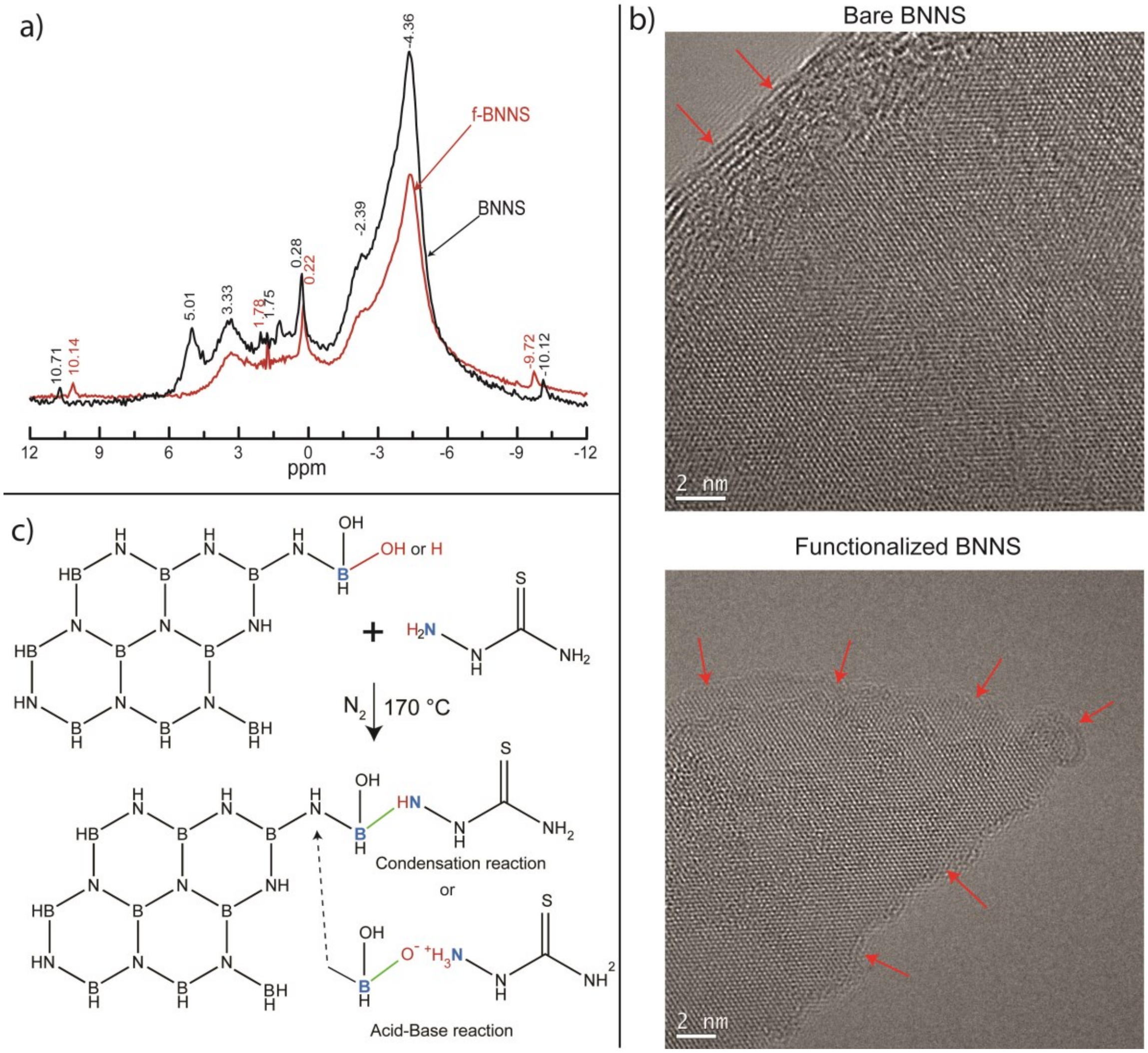

Figure 9. a) 1H MAS NMR spectra of BNNS before and after the functionalization reaction with thiosemicarbazide, b) HR-TEM micrographs of BNNS before and after the functionalization reaction, and c) Proposed reaction schemes.

3.3.2. Electrodeposition of Thin Film Nanocomposite TIMs

Traditional molten metal-based mixing and agitation approaches for metal/inorganic nanocomposites are not feasible for producing metal/inorganic/organic hybrid nanocomposite TIMs due to the presence of organic linker molecules and the high melting temperature of copper. To overcome this challenge, we developed a programmed electro-codeposition approach by which the reduction of copper ions and the nucleation and growth of the resultant elemental copper on the cathode occurs, while f-BNNS experience Brownian motion and reaches the cathode through diffusion (Fig. 10a). Once the f-BNNS bearing carbonothioyl/thiol groups on the terminal edges come into the contact with copper crystals, the chemisorption reaction takes place (Fig. 10b). The coordination reaction between copper atom and sulfurous groups was confirmed through X-ray photoelectron spectroscopy (XPS) studies as evidenced by a shift in binding energy of some fraction of copper from 932.75 eV to 934.80 eV. The interplay among these three processes determines the nanostructure of the resultant metal/inorganic/organic hybrid nanocomposite. It is also possible to manipulate the nanostructure by adjusting the composition and pH of electrolyte, current density, and temperature. Using this approach, we were able to produce fairly homogenous films (Fig. 10c). The fracture SEM studies revealed that the nanocomposite TIMs developed have a peculiar nanostructure in that f−BNNS are localized only at the grain boundaries of copper crystals (Fig. 10d), the manifestation of which on the mechanical and thermal properties will be discussed in the next paragraphs.

3.3.3. Thermal and Mechanical Characterization of Thin Film Nanocomposites

The bulk thermal conductivity of the nanocomposite TIM, measured via the laser flash diffusion technique as well as the phase-sensitive transient thermoreflectance technique, was found to decrease with increasing amount of f-BNNS in the copper matrix, with diminishing returns (Fig. 11a). The reductions due to the presence of organic linker molecules was relatively low (up to 40%, from 370 W/m.K to 211 W/m.K), which is ascribed to the fact that TSC covalently attaches BNNS to copper matrix. This is consistent with the findings of Losego et al.[73] showing that the strength of a single bonding layer directly governs phonon heat transport across an interface. Strong covalent interactions lead to much higher interfacial thermal conductance in comparison to the weak van der Waals interactions due to ability to form an effective gradient for reducing the impedance mismatch. Furthermore, the localization of TSC at the edges of BN nanosheets can guide phonons through the in-plane direction along nanosheets rather than the out-of-plane direction, along which the thermal conductivity of 2-D materials is about two-orders of magnitude lower than that in the in-plane direction.

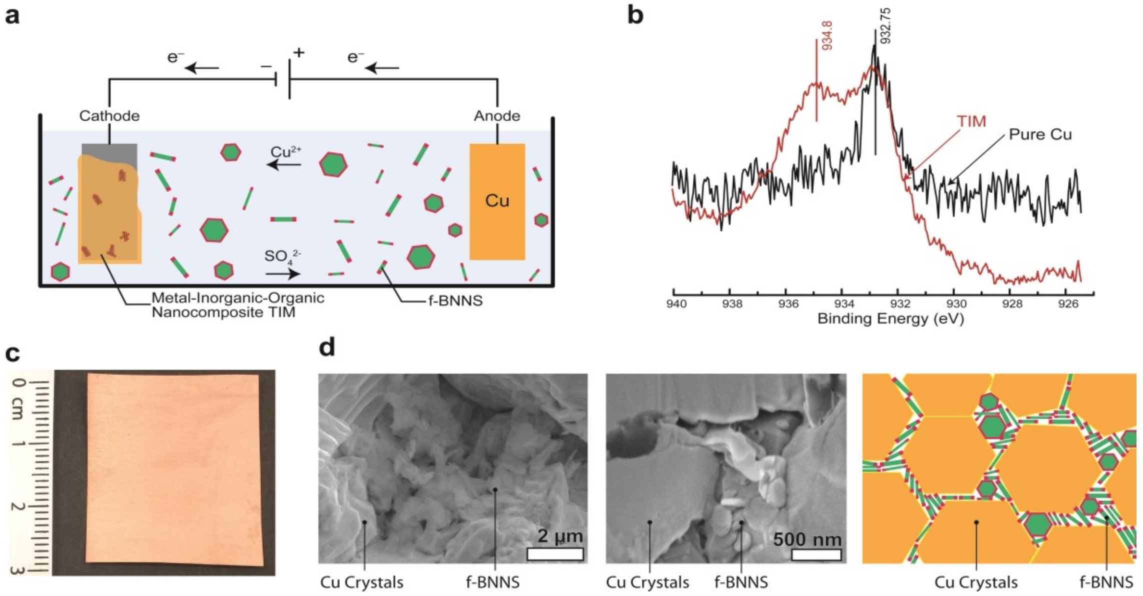

Figure 10. a) Illustration of the chemisorption coupled electrodeposition approach, b) XPS analysis of copper in pure copper and nanocomposite TIM, c) photograph of a typical metal/organic/inorganic nanocomposite TIM, and d) SEM micrographs and schematic illustration showing the distribution of f-BNNS across the copper matrix.

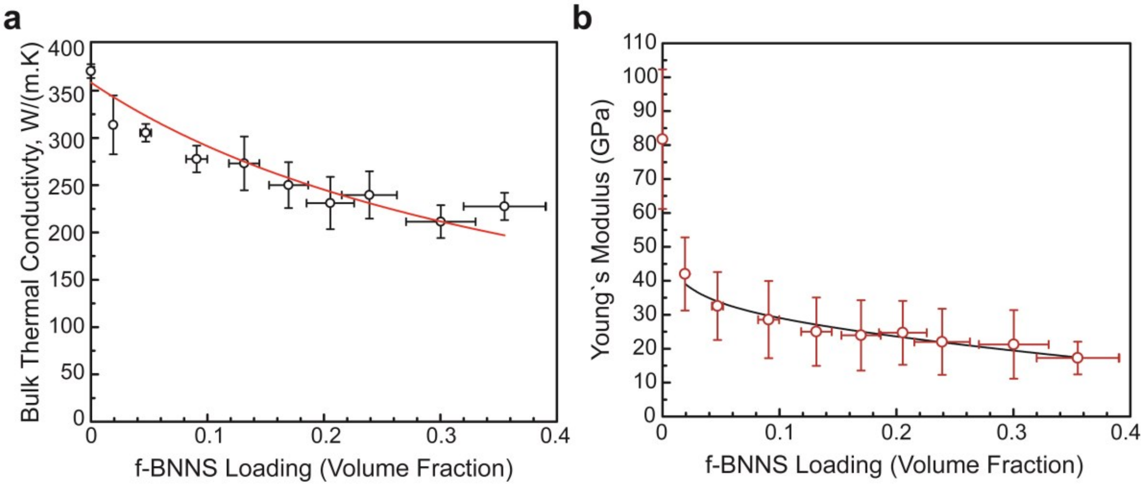

Figure 11. The variation in the bulk thermal conductivity of the hybrid nanocomposite TIM as a function of functionalized boron nitride nanosheet (f-BNNS) loading. The fit is based on the percolation theory. b) The influence of f-BNNS content on the Young's modulus of the hybrid nanocomposite. The fitted line is obtained through the modified Halpin-Tsai model with discontinuous fillers. Error bars represent one standard deviation in both cases.

The details of complex thermal transport across the metal/inorganic/organic nanocomposite can be explained with a combination of phononic and electronic modes. In the absence of f-BNNS, the system is in a percolated regime with interconnected copper microcrystals where the thermal transport is mostly through electrons. As f-BNNS is introduced into the system, while the degree of percolation of copper microcrystals decreases, new phonon bandwidth emerges via f-BNNS linkers owing to an-harmonic phonon-phonon coupling and electron-phonon coupling at the metal-linker interface.[74] Overall, organic linkers, filtering some phonon modes as well as scattering moieties for electron transport, act as a bottleneck to thermal transport and result in a reduction of thermal conductivity of pure BNNS, and thus the overall composite. Bulk thermal conductivities of copper matrix and f-BNNS calculated according to fit explained by Phelan et al[75] were 370 and 100 W/(m.K), respectively, which are in agreement with recent studies.[76] Introduction of f-BNNS in copper grain boundaries replaces a part of electronic thermal transport with phonon thermal transport. As f-BNNS loading is increased, more such sites reduce the thermal conductivity until no new sites are occupied by f-BNNS. We see this region is obtained around the 0.12 volume fraction (Fig. 11a) and beyond this point, no more reduction in thermal conductivity is observed.

When a heat source and a heat sink are coupled through a TIM, the asperities of heat source/sink surface apply compressive stress in the perpendicular direction to the TIMs. Thus, a nanoindentation technique, involving a very similar geometry, is used as the main mechanical characterization technique in this study. As shown in Figure 11b, the Young's modulus of the hybrid nanocomposite gradually decreased with the increasing f-BNNS content in the hybrid nanocomposite, slowly plateauing around 20 GPa. This trend can be attributed to the interplay among metallic bonds between copper atoms; van der Waals interactions between copper microcrystals, between copper microcrystals and BNNS, and between BNNS; the bond strengths of ligand-BNNS pair and ligand-copper microcrystal pair; and buckling or bending of BNNS. In the absence of f-BNNS, the mechanical properties of copper are determined by van der Waals forces and metallic bonds holding copper microcrystals together. When f-BNNS is introduced to the matrix, the van der Waals forces between copper microcrystals decrease due to the screening effects induced by the presence of less polarizable materials and the increased distance between microcrystals, which also causes the disappearance of the short ranged inter-crystalline metallic bonds.[77] However, new forces stemming from the linking of copper to BNNS through thiol/copper and amine/BNNS bonds also arise. Because f-BNNS is only functionalized from the edges, the latter effect cannot balance the former effect, resulting in a reduction in the Young's modulus. As the f-BNNS loading increases, the formation of f-BNNS aggregates between grain boundaries occur. Considering that van der Waals interactions between metals are much higher than that between inorganics or organics, the presence of f-BNNS aggregates, in turn, introduce regions that are held together through weak van der Waals forces in the nanocomposite.

The modulus values were also obtained from the modified Halpin-Tsai model by considering the f-BNNS as randomly oriented discontinuous fillers:[78,79]

$$E_c = \left[{}^{3}\!/_{8} \frac{1+2(l_f/d_f)\mu_L v_f}{1-\mu_L v_f} + {}^{5}\!/_{8} \frac{1+2\mu_T v_f}{1-\mu_T v_f} \right] E_M \qquad [3]$$

where $\mu_L = \frac{(E_f/E_M)-1}{(E_f/E_M)+2(l_f/d_f)}$, $\mu_T = \frac{(E_f/E_M)-1}{(E_f/E_M)+2}$, E_c, E_M, E_f are the elastic moduli of the composite, matrix and filler, respectively, l_f, d_f and v_f are the filler thickness, diameter and volume fraction, respectively. The calculations from the model yielded the elastic moduli of copper and the f-BNNS to be 48.2 GPa and 1.6 GPa, respectively (r^2=0.952). The resultant elastic modulus of pure copper was somewhat lower than the literature value, which is well-known to occur for electrodeposited materials due to the formation of nano- and micro-pores.[80,81] Most organic ligands have elastic moduli less than 1 GPa[82] and the reported out-of-plane bending and in-plane elastic modulus of BNNS are

20-30 GPa[83] and 0.8-1.2 TPa,[84] respectively. In addition, the organic ligands constitute a small fraction of f-BNNS volume (1.4% - 1.2%) due to the functionalization only on the edges. Hence, an effective modulus of 1.6 GPa for the filler implies that f-BNNS behaves closer to the Reuss Model (the lower-bound modulus) where the elastic modulus is averaged via the inverse rule of mixtures.

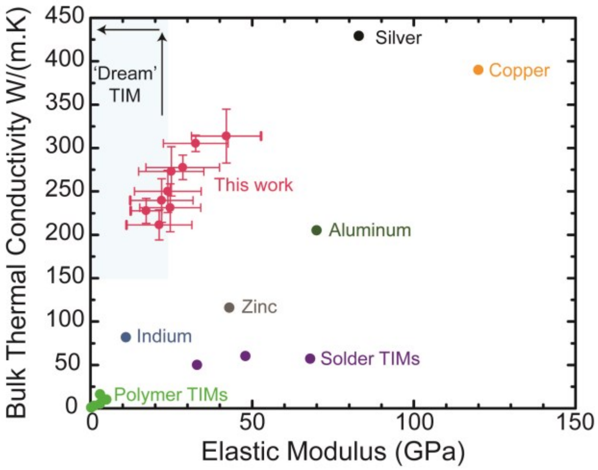

Figure 12. The comparison of bulk thermal conductivity versus elastic modulus values for various types of thermal interface materials and the developed chemically-integrated metal/organic/inorganic nanocomposite thermal interface materials.

3.4. Conclusions

In general, the total thermal resistivity of a TIM strongly depends on its bulk thermal conductivity and Young's modulus, design parameters such as thickness and applied load (or adhesion force), and contact resistance. An ideal TIM should be both highly thermally conductive and mechanically compliant, in order to effectively transport heat between two mating surfaces and to be reliable. Hence, to put the measured properties of the hybrid nanocomposites into perspective, we relied on a bulk thermal conductivity versus Young's modulus plot and compared our values with the current-state-of-art and common TIMs (Fig. 12). While the bulk thermal conductivity of the hybrid TIM was only 40% lower than that of pure copper (the base matrix), the compliance of the hybrid TIM was about 4 times larger than that of pure copper. In comparison to polymer TIMs, the hybrid nanocomposite TIMs lead to one-to-two orders of magnitude increase in the thermal conductivity with only a small loss in softness. The developed TIMs thermally outperforms solder TIMs about three- to five-fold while they have similar or a slightly better mechanical compliance than solder TIMs. The combination of these thermal and mechanical properties gave rise to a total thermal resistance of 0.38±0.10 mm^2.K/W for 30 μm bondline thickness and 0.56±0.10 mm^2.K/W for 50 μm bondline thickness (please see the Supporting Information section for more details) under adhesive load (i.e. no external load is applied). The thermal resistance values contain the contribution from several interfaces and solid layers, but are still very low compared with the traditional TIMs – at least a factor of 5 lower at comparable bondline thicknesses.[65] The chemically-integrated metal/organic/inorganic hybrid nanocomposite provides a promising thermal management solution that can significantly reduce the thermal resistance in high thermal dissipation applications, and can help in achieving the broader goals of compact, high-power-density (electronic) components.

3.5. Supporting Information

3.5.1. Further Details of Synthesis and Characterization of the f-BNNS

Preparation and characterization of BNNS: The h-BN powder (98%, APS: 500μm) dispersed in N-Methyl-2-Pyrrolidone (NMP) was exfoliated by ultrasonic dispersion using a SYCLON ultrasonic cell crusher (Syclon Electr. Instr. Comp., Zhejiang, China). A suitable polar solvent having a similar surface energy to that of h-BN can be efficiently used for exfoliation. For this purpose, NMP (surface energy: 40.5 mJ/m^2 at RT) was selected as the solvent for exfoliation of h-BN (surface energy: 65 mJ/m^2). The dispersion containing the nanosheets was diluted and dropped onto a silicon wafer, and dried at 75 °C for 24 hours for AFM analysis. Height sensor images were obtained via a Bruker Dimension Icon AFM (Bruker, Santa Barbara, CA) at 0.5 Hz scan rate 512 samples/line. Several images were obtained to statistically determine the size and height distribution of BNNS via Nanoscope Analysis Software. Particle size distribution of the BNNS was also confirmed using dynamic light scattering (DLS) (Zetasizer Nano ZS90, Malvern Instr.Inc., Westborough, MA). The size distribution is shown in Figure 13 in supplementary information.

Characterization of f-BNNS: Synthesized f-BNNS was mounted on to a copper tape and placed on an Omicron XPS (Scienta Omicron GmbH, Taunusstein, Germany) for X-ray photoelectron spectroscopy. High resolution XPS spectra were carried out for N, S, C, and O atoms. In addition, pure BNNS and pure thiosemicarbazide were also analyzed to confirm the functionalization. For further confirmation, Infrared and Raman spectroscopies were obtained via a Shimadzu IR Prestige ATR-FTIR (Shimadzu

Scientific Instruments Inc., Columbia, MD) and a high spectral resolution analytical Raman microscope (LabRAM HR Evolution, HORIBA, Ltd., Edison, NJ), respectively.

Characterization of TIMs: f-BNNS content in the nanocomposite thin films was obtained by chemical-elemental analysis. The nanocomposite TIMs were cut into smaller pieces and immersed in an H_2SO_4/HNO_3 acid solution (3:1 in volume fraction) at 40 °C. The solution dissolved the copper content and settled down the f-BNNS. The precipitate was drained out, dried, and weighed. Then, it was put in the acid solution again to remove any possible residual copper. This step was repeated several times until no change in the weight of the f-BNNS was observed. Several samples for each experimental condition were prepared and measured for statistical reliability. The Secondary ion mass spectrometer (SIMS) CAMECA 4F (Ametek Inc., France) has also been used to confirm the mass fraction of thin film nanocomposite samples. The analyzed surfaces were sputtered by the 5.5 keV O_2^+ beam with a current of 15 nA. The diameter of the beam was ~3 μm; the raster was 250x250 μm^2 for all samples. The measured secondary ions were positively charged. Nanocomposite TIMs were prepared with various f-BNNS concentrations in the electrolyte solution ranging from 0 wt.% to 2.5 wt.%.

Mechanical Characterization: Elastic modulus and Poisson`s ratio of the samples were measured by tensile testing via an INSTRON 5944 universal testing instrument (INSTRON, Norwood, MA). For this purpose, the thin film nanocomposite samples were machined as dog-bone-shaped tensile test specimens, which were produced in accordance with a scaled-down ASTM D882 standard.

Thermal Cycling Behavior and Coefficient of Thermal Expansion (CTE): Thermal cycling tests were performed with the DLF-1200 Laser Flash Diffusivity system was used to test the reliability of the produced TIMs. The samples were subjected to thermal cycling between room temperature (RT) and 100 °C for ten cycles. Coefficient of thermal expansion in the produced samples was measured using a thermal mechanical analyzer-TMA (TA Instruments, Newcastle, DE) with a built-in tensile test setup. Rectangular thin film samples were prepared, mounted between the grips in the TMA analyzer, and heated up to 140 °C. The result was compared with those obtained from pure copper and pure silicon.

3.5.2. Synthesis and Characterization of the Filler

Characterization of BNNS: Filler geometry plays an important role in determining the mechanical and thermal properties of composite materials. The AFM micrograph in Figure 13a shows that the BNNS are dispersed as mono- or few-layered structures. The bright features on the nanosheets are assumed to be NMP residues since it is a relatively non-volatile solvent. The size and thickness of the nanosheets were found to be 444±115 nm and 3.05±0.79 nm, respectively, (Fig. 13b and c) by measuring the dimensions of hundred individual nanosheets. Also, the effect of sonication on the particle size distribution was investigated by DLS measurements. Figure 13d indicates the decrease in the particle size with an exponential trend, which implies that the sonication of the h-BN powder can generate sufficient energy to break some of the covalent bonds between B and N atoms, and introduce defects at the edges.

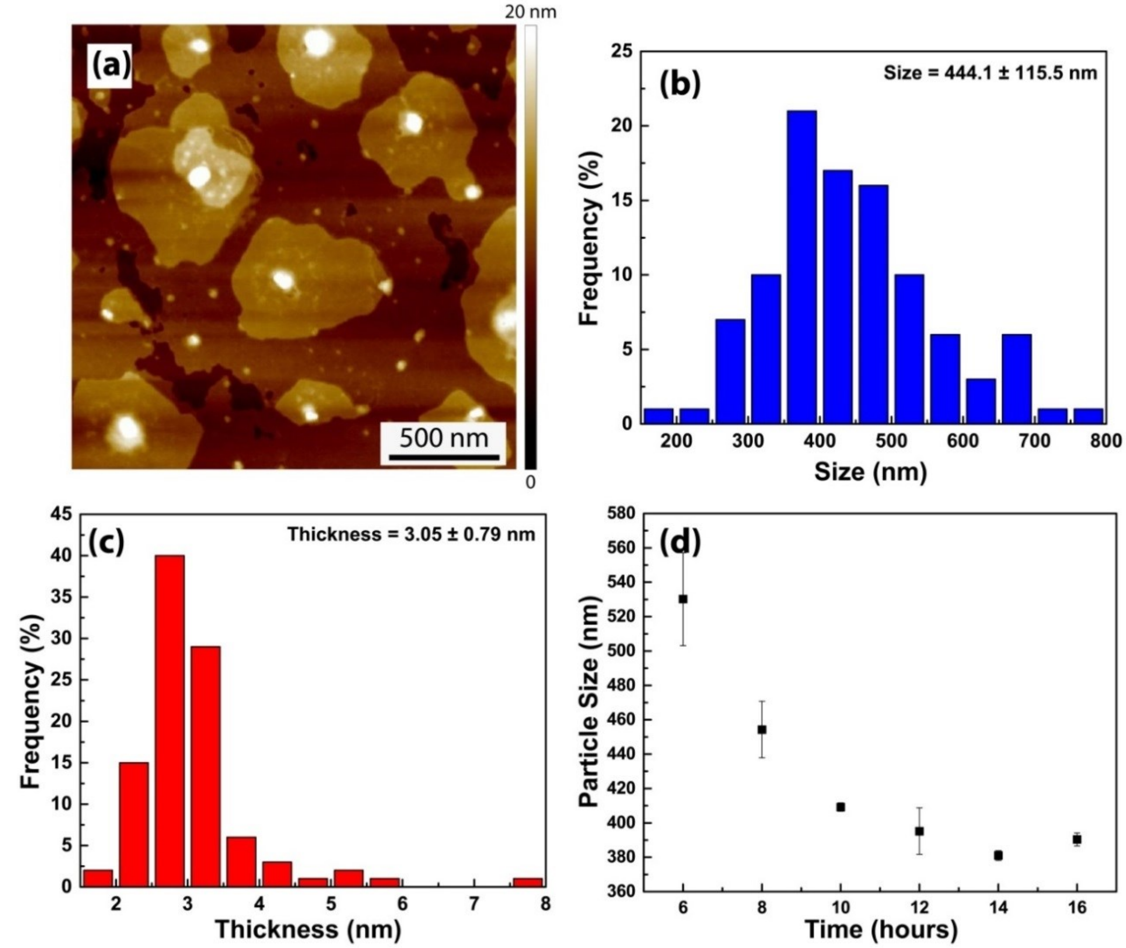

Figure 13. Characterization of BNNS: a) a height sensor image taken from exfoliated BNNS, b & c) frequency distribution of nanoparticle size and thickness of the BNNS, respectively, obtained from AFM images, and d) effect of exfoliation time on particle size distribution.

Functionalization of BNNS: Figure 14a gives the information on XPS data for sulfur oxidation states. It is understood that sulfur bonding state is changed from double bond to single bond. The shift in XPS suggests the presence of S atom in the form of a thiol as shown in the NIST database. To accommodate all above observations, we propose that the tetra coordinated B of the BNNS interacts with the amine nitrogen of TSC. Finally, the S atom undergoes tautomeric transformation to give thiol.

In addition to XPS and RAMAN Spectroscopies obtained from the nanocomposite TIMs, IR spectra of BN nanosheets shown in Figure 14b confirmed the functionalization of BNNS with thiosemicarbazide. The disappearance of peak at 1614 cm^{-1} and the shift of the peak at 1639 cm^{-1} to 1675 cm^{-1} is attributed to the cleavage of amine groups in thiosemicarbazide and the reaction of the remaining amine group with boron atoms on the BNNS. Similarly, the disappearance of peaks at 3255 cm^{-1} and 3362 cm^{-1} can also support these conclusions.

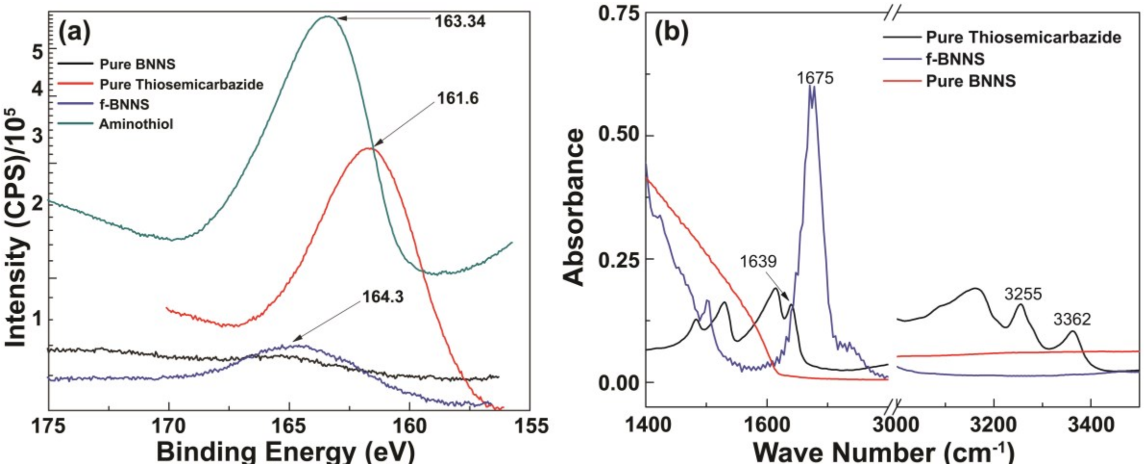

Figure 14. Characterization of functionalization via: a) XPS and b) infrared (IR) spectroscopy for pure BNNS, pure thiosemicarbazide and f-BNNS. XPS scan for a commercial aminothiol (3-Amino-1,2,4-triazole-5-thiol) was also performed for comparison.

Figure 15 presents ^{11}B MAS NMR spectrum of BNNS and f-BNNS. For neat BNNS, there were four major peaks: the largest signals (20.8 ppm and 11.8 ppm) correspond to tricoordinated boron atoms within B−N bonds of planar BN_3 groups, the signal at $\delta = -25.7$ ppm indicates the presence of tetragonal boron atoms (i.e. R_4B-), and the signal at δ = 66.8 ppm suggests the existence of boron atoms with hydroxyl groups. The reaction of BNNS with TSC resulted in shifts only for tetracoordinated boron atoms (from −25.7 ppm to −17.2 ppm) but not for boron from planar BN_3, indicating that the functionalization reaction takes place from the reactive edges of BNNS.

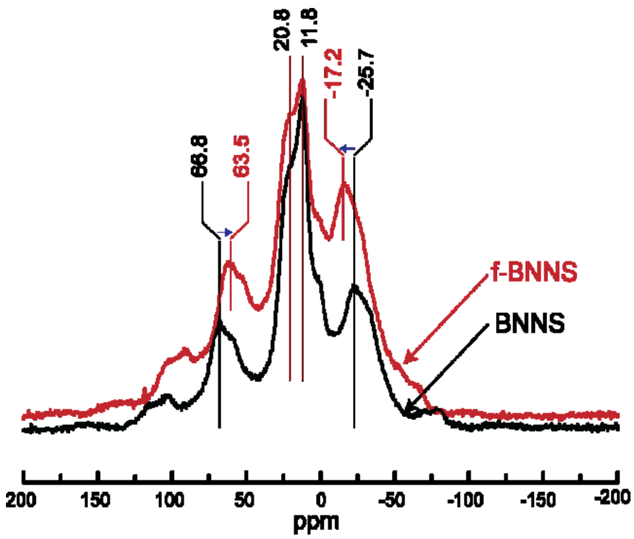

Figure 15. ^{11}B MAS NMR spectra of BNNS and f-BNNS

Figure 9a presents the solid state 1H MAS NMR spectra of BNNS and f-BNNS. There are a total of 8 different H atoms present in BNNS. These correspond to different hydrogens bonded to edge B and N atoms (N_2BH, NBH_2, NBH_3^-, B_2NH, BNH_2, BNH_3^+) and others in $N_2B(OH)$ and $NB(OH)_2$ in no specific order. The major changes are observed as disappearance of peak at δ = 5.01 and shift at δ = 10.71 and -10.12 which correspond to hydrogens attached to edge B(OH), BNH_3^+ and NBH_3^-, respectively. Figure 16 compares Raman spectra of BNNS, f-BNNS and pure thiosemicarbazide.

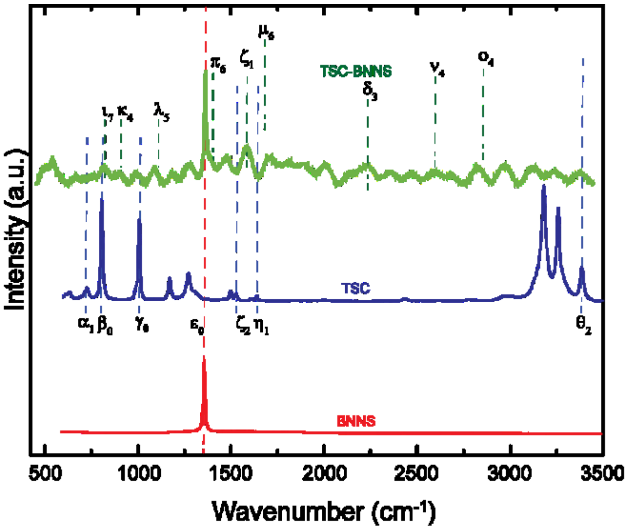

Figure 16. Raman Spectroscopic studies of BNNS, f-BNNS and pure Thiosemicarbazide

3.5.3. Characterization and Performance Evaluation of Nanocomposite TIMs

Surface Characterization and Measurement of f-BNNS Content: Figure 17a-c show the secondary ion micrographs obtained for the thin film nanocomposite samples, which were grown on to Al substrates at various electrolyte solutions (low, intermediate and high, respectively). High intensities of Boron ions were detected on the surface whereas the intensity gradually decreased at the depth of ~1 μm, and eventually stabilized. As expected, the intensity of the B ions on the nanocomposite TIMs is increasing as the concentration of the solution increases. From the intensity vs. time profiles, it was determined that the intensity of f-BNNS in the nanocomposite samples is linearly increasing with the f-BNNS concentration in the electrolyte solution. The f-BNNS loading in the samples corresponding to the intensity of f-BNNS were determined via chemical elemental analysis. Figure 17d shows the f-BNNS content of the nanocomposite samples as a function of solution concentration.

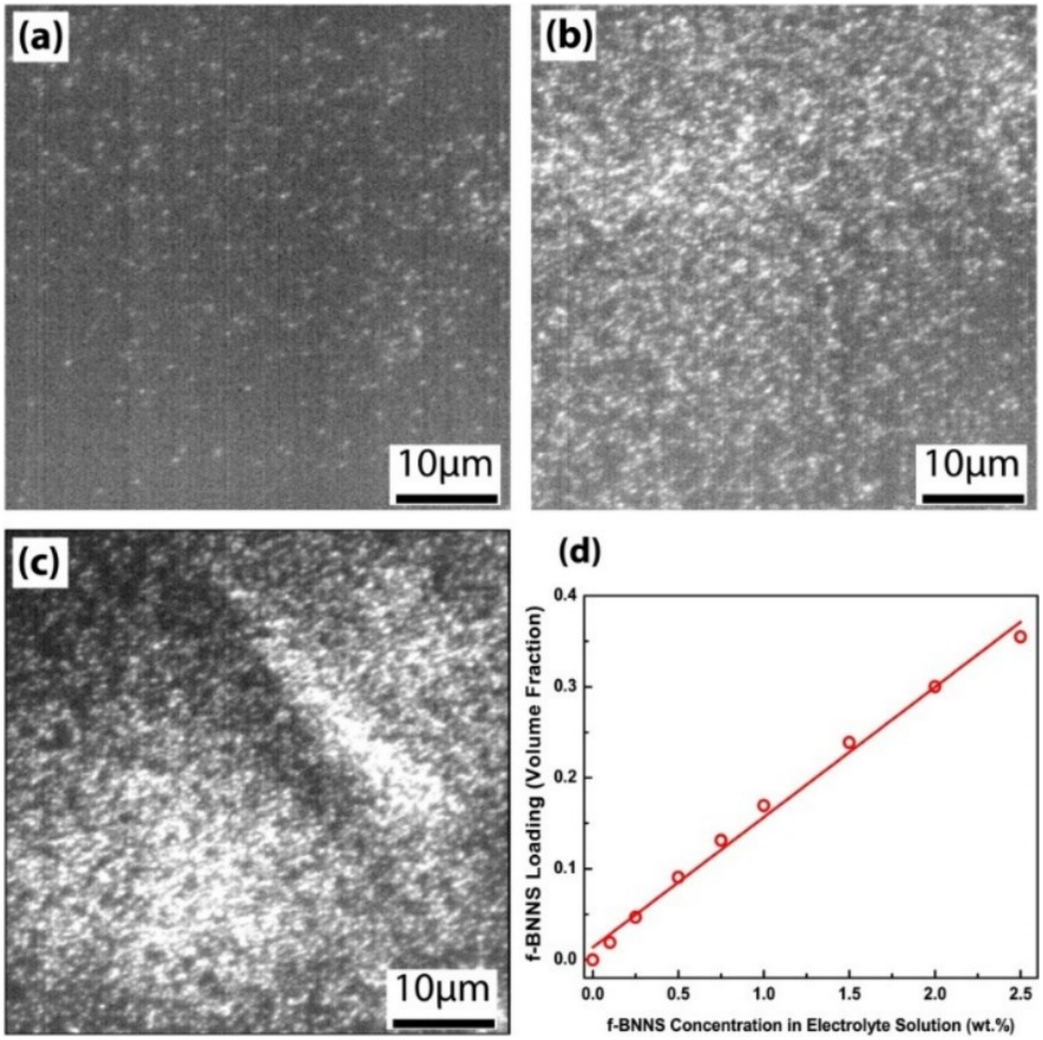

Figure 17. SIMS micrographs (lateral resolution ~3μm) obtained for nanocomposite TIMs at various f-BNNS concentrations in electrolyte solution: a) low (0.1 wt.%), b) intermediate (1.0 wt%) and c) high (2.5 wt.%) concentrations. (White spots indicate B ions) d) f-BNNS loading in nanocomposite TIMs in terms of volume fraction versus f-BNNS concentration in electrolyte solution.

Mechanical Characterization: Nanoindentation technique was used for mechanical characterization of nanocomposite thin film samples. Also, the reduced modulus values obtained from Nanoindentation tests can be converted to Young`s modulus via the Poisson`s ratio. Tensile test specimens were applied a pre-determined tensile strain in the elastic region, the corresponding lateral strain was calculated by using a micrometer, and the Poisson`s ratio was calculated by the following equation;

$$v = -\frac{d\varepsilon_y}{d\varepsilon_x} \qquad [4]$$

The Poisson`s ratio of the nanocomposite samples was measured to be 0.337± 0.05, which is not significantly different from that of pure copper (0.34). Then, the Young's modulus (E_s) of the samples were calculated via Eq. 5,

$$\frac{1}{E_r} = \frac{(1- v_i^2)}{E_i} + \frac{(1-v_s^2)}{E_s} \qquad [5]$$

where subscript i denote indenter properties and E_r is the reduced modulus. The calculated Young`s moduli of nanocomposite samples versus f-BNNS loading response is depicted in Figure 11b.

Thermal Characterization: (i) Laser Flash Diffusivity: Thermal conductivity of free-standing samples was calculated using the measured thermal diffusivity (α), specific heat capacity (c_p), and density (ρ) values as follows:

$$\alpha = K.\rho^{-1}.c_p^{-1} \qquad [6]$$

(ii) Phase-sensitive transient thermoreflectance measurements: Besides the laser flash diffusivity technique, a phase-sensitive transient thermoreflectance (PSTTR) technique was used to measure the thermal properties (including thermal contact resistances and overall thermal resistance/resistivity) of the hybrid nanocomposite materials. The nanocomposite samples were grown on to silicon wafers at varying thicknesses up to 50 μm, following the physical vapor deposition of a 300 nm copper layer on the wafers for electrical conductivity. PSTTR is a modulated optical pump-probe technique that utilizes two lasers to study the thermal properties of multi-layered structures. A pump laser is modulated by a waveform generator and the working frequencies are determined based on the thermal property and thickness of the test samples. The modulated pump laser is directed on to one of the sample surfaces and serves as a heat source. The laser has a $1/e^2$ radius of about 1.5 mm and the maximum power of the laser is 5 W, yielding a maximum heat flux of about 2.8 W/mm^2. The induced thermal wave penetrates through the sample, causing the temperature on the opposite surface to oscillate following the same periodicity. A probe laser is applied to this opposite surface to monitor the thermoreflectance change which is proportional to the temperature oscillation. A photodiode captures the reflected probe laser and transmits the optical signal into a lock-in amplifier, which compares the probe laser signal with the original modulation from the waveform generator to extract the phase shift. A schematic of the PSTTR experiment is shown in Figure 18, and further details about the PSTTR technique are described in another publication.[85] If the thickness, specific heat and density of the hybrid nanocomposite material are accurately measured, then the bulk thermal conductivity can be derived by fitting the relevant heat transfer model to the extracted phase shift. Table 1 lists the parameters used in the heat transfer model to fit the PSTTR data.

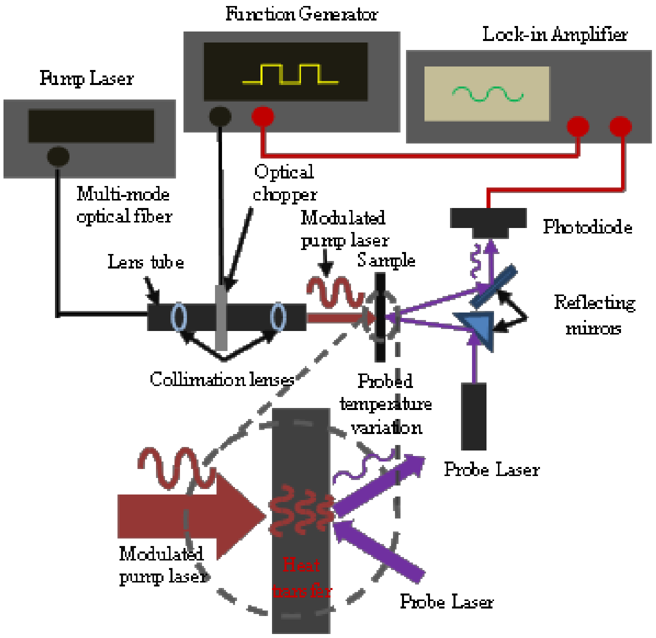

Figure 18. Schematic of the PSTTR technique.

Table 1. Parameters used in the heat transfer model to fit the PSTTR data

Materials	**Layer thickness (µm)**	**Density (kg/m3)**	**Specific heat capacity (J/kg·K)**	**Bulk Thermal conductivity (W/m·K)**
Silicon[2]	100	2330	712	148
Aluminum[86]	3 ~ 5	2702	903	237
Hybrid nanocomposite	30 ~ 50	7332	440	232

The hybrid nanocomposite samples were fabricated in two configurations – single-sided and bonded, as demonstrated in Figure 19a and c, and were characterized following a two-step strategy to comprehensively evaluate the thermal properties and performance. First, because the nanocomposite is relatively thin and soft, it needed to be supported for the PSTTR measurements. Therefore, the hybrid nanocomposite material was electrodeposited onto a substrate to form a single-sided structure. In this research, silicon was used as the substrate because the physical and thermal properties have been comprehensively studied, as listed in Table 1. Another advantage associated with silicon is that a highly-polished surface can be obtained, which enhances the specular reflection of the probe laser. The nanocomposite's thickness varied from 30 to 50 μm, while the silicon substrate was 100 μm thick (Fig. 19b). For these single-sided samples, the bulk thermal conductivity of the hybrid nanocomposite and the interfacial contact resistance were the two fitting parameters. Once these parameters were obtained using PSTTR, the hybrid nanocomposite was then sandwiched between two silicon substrates to fabricate a bonded structure (Fig. 19c). The purpose of preparing the bonded structure was to evaluate the nanocomposite's thermal performance when it was being used in a TIM configuration - *i.e.* sandwiched between two substrates. The single sided sample was placed in a cylindrical die, and rapidly bonded to a bare silicon substrate with a molten aluminum layer (4-5 μm) at 650 °C temperature under nitrogen atmosphere. The physical/thermal properties of the aluminum layer are listed in Table 1, and it is counted as part of the entire interfacial layer. Therefore, when developing the heat transfer model, the interfacial layer was considered to have two solid layers (hybrid nanocomposite and aluminum) and three interfaces. Given that the bulk thermal conductivity of the hybrid nanocomposite, and the contact resistance between the hybrid nanocomposite and silicon substrate were already identified by the characterization of the single-sided samples, only the contact resistances of the other two interfaces (Si-Al and Al-nanocomposite) needed to be determined for the bonded samples. Hence, the four critical unknown parameters were acquired from two independent fitting procedures, and the reliability of the results was consequently very good. By summing the bulk thermal resistances and interfacial contact resistances, the total thermal resistance of the interfacial layer was calculated.

As stated previously, a heat transfer model is required to fit the experimental data, and extract values of the unknown parameters of interest. In this work, the single-sided and bonded samples contained different number of layers. Normally, heat transfer in different configurations may demand different models. Here, due to the similarity between the two structures, we utilize a general heat transfer model that is capable of deriving the phase shift in the structures with arbitrary number of layers. Details on the

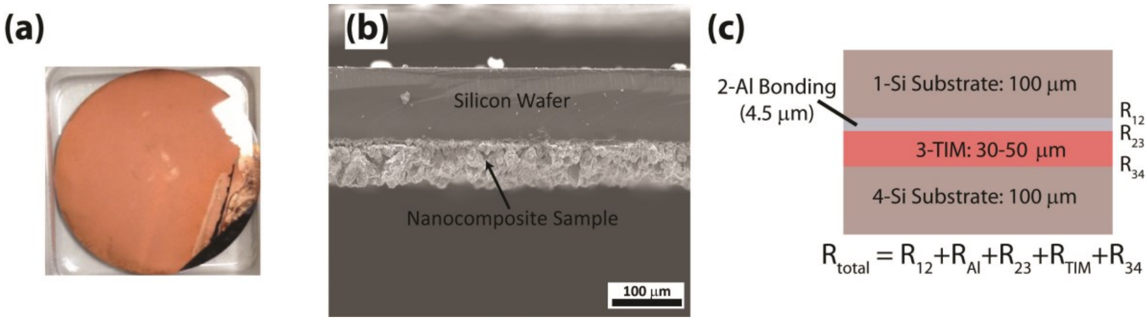

Figure 19. a) Cu/f-BNNS nanocomposite TIMs deposited on silicon substrate, b) a scanning electron micrograph (SEM) of the single-sided samples, in which multiple thickness measurements are made and the average is used in the characterization, and c) cross-section of sandwich configuration of the TIMs between two silicon wafers. Thin aluminum layer was used for diffusion bonding.

development of the heat transfer model and the solutions can be found elsewhere.[87] The general solution is presented in Eq. 7:

$$\Phi = \frac{\pi}{4} + \sum_{i=1}^{n} d_i \sqrt{\frac{\pi f}{\alpha_i}} + tan^{-1}\left[\frac{-\sum_{\substack{i_1, i_2, \dots i_{n-1} \in \{0,1\} \\ i_1+i_2+\cdots+i_{n-1}>1}} \mathrm{Im}\left[(1-j)^{i_1+i_2+\cdots+i_{n-1}}\right] \mathcal{RR}_{12}{}^{i_1} * \mathcal{RR}_{23}{}^{i_2} * \cdots * \mathcal{RR}_{n-1,n}{}^{i_{n-1}}}{1+\sum_{\substack{i_1, i_2, \dots i_{n-1} \in \{0,1\} \\ i_1+i_2+\cdots+i_{n-1}>1}} \mathrm{Re}\left[(1-j)^{i_1+i_2+\cdots+i_{n-1}}\right] \mathcal{RR}_{12}{}^{i_1} * \mathcal{RR}_{23}{}^{i_2} * \cdots * \mathcal{RR}_{n-1,n}{}^{i_{n-1}}}\right] \qquad [7]$$

Here, f is the frequency; α_i and d_i are the thermal diffusivity and the thickness of the *i*-th layer, respectively. $RR_{i,i+1}$ is a lumped parameter that includes all the known and fitting parameters in the adjacent layers i and i+1. This treatment enables convenient calculation of the overall phase shift Φ using programming software such as FORTRAN or MATLAB. The samples in this work contained either two or four layers, so i equals 2 or 4. By substituting the numbers into Equation 4, the relevant theoretical phase shifts were calculated, and were then fitted to the experimental data to determine the best value(s) of the fitting (unknown) parameters. A typical fitting graph is shown in Figure 20. In this figure, discrete experimental data points (blue circles) are very close to the theoretical phase shift values (red solid line) throughout the entire frequency range. Varying the fitting parameters causes the shape or slope of the solid line to change. When the difference between the theoretical solution and the experimental data reaches a minimum value, the values of the fitting/unknown parameters are considered to have been obtained.

Samples of various thicknesses and incorporating various ligands were prepared for a comprehensive investigation of the thermal properties of the hybrid nanocomposites. The fitted bulk thermal conductivity of the nanocomposite ranged from 211 to 277 W/m·K, at the same level as metallic materials and showing significant improvement compared to the polymer-based or solder TIMs. The thermal contact resistances, by virtue of the electrodeposition process and the material's high mechanical compliance, were also significantly reduced to a competitively low level of around 0.1 mm^2·K/W. By adjusting the thickness and BNNS concentration, the total thermal resistance of the valid bonded samples ranged from 0.38 to 0.56 mm^2·K/W for 30 to 50 μm bondline thicknesses, respectively, which are lower than those of almost all traditional TIMs for comparable bondline thicknesses. For comparison, a high-performance commercial-grade thermal grease that we characterized had a thermal resistance around 15 to 30 mm^2·K/W[88] for 30 to 50 μm bondline thicknesses. A novel thermoplastic film material incorporating highly-aligned micron-sized fibers yielded a thermal resistance of about 10 mm^2·K/W1 for 50 to 75 μm bondline thicknesses. Therefore, the hybrid nanocomposite TIM exhibits superior thermal properties which greatly enable the possibility of its application in high power-density components or harsh-environment electronics.

To perform the PSTTR measurements, an automatic data acquisition system was employed to collect the experimental data. For each frequency, the sampling time was 60 seconds and the sampling rate was 10 Hz. Hence, there were a total of 600 extracted phase shifts and the average of them was recorded as the phase shift for any given frequency. The random uncertainty with the data acquisition system was estimated to be 5 degrees, while the systematic uncertainty was about 1 degree. In addition to the uncertainty associated with the measurements, the regression analysis also introduced uncertainty into the system. When fitting the model to the experimental data, the difference between the modeling and experimental results was minimized to achieve the best fit, thereby determining the values of the fitting parameters. However, errors came in to the fitting process because of uncertainties in the other modeling parameters (known and unknown). We implemented a methodology from Malen et al.'s work[89] for the uncertainty analysis. The uncertainty of the fitting parameter was estimated from the uncertainties in the modeling parameters. After the best fit was achieved, each of the modeling parameters was perturbed by a small quantity (its uncertainty), and the regression process was repeated to find the new values of the fitting parameters. Then, the difference between the new and old values was the uncertainty from the fitting process itself. Using this methodology and combining the fitting uncertainty with the

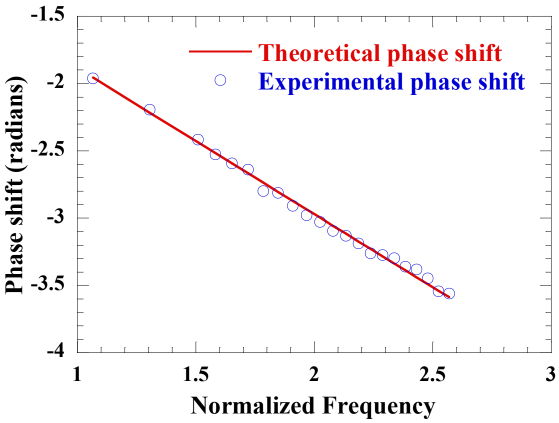

Figure 20. The dependence of phase shifts on normalized frequency for one selected bonded sample. The red solid line is the theoretical phase shift based on the best-fitted value of the fitting parameters, and the circles are experimental data points for the phase shift

experimental uncertainty (random and systematic uncertainty), the overall uncertainty at 95% confidence level was calculated for each fitting parameter.

Thermal Cycling Behavior and Coefficient of Thermal Expansion (CTE): It is crucial to understand the combined effect of time and temperature on the long-term reliability and aging behavior of the developed nanocomposites. Hence, we conducted some "stress tests" by exposing our material via heating-cooling cycles as well to determine if there is any hysteresis in thermal properties. Figure 21 shows the bulk thermal conductivity of pure copper and our nanocomposite TIM as a function of thermal cycling between 25 °C and 100 °C. For 10 cycles, there was no statistical difference in the bulk thermal conductivity of the developed TIMs, indicating its reliability with respect to on/off (heating/cooling) cycles. which have different coefficients of thermal expansion (CTE). When an electronic package contains various insulating and conducting materials device is powered up so that the package is subject

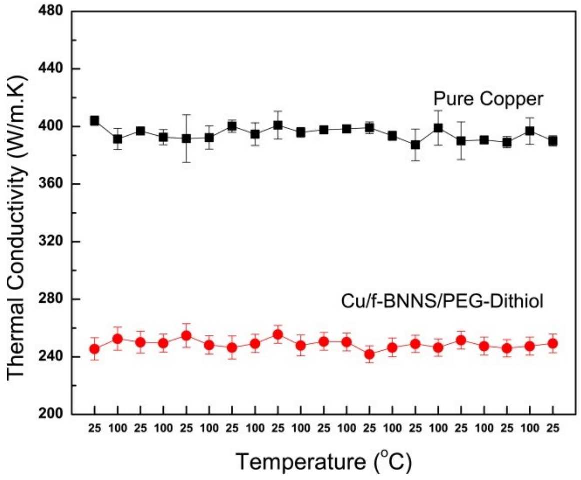

Figure 21. Thermal cycling for electrodeposited pure Cu and hybrid nanocomposite TIMs between 25 ˚C and 100 ˚C

to a temperature change, each material with different CTE deforms at a different rate. This non-uniform CTE distribution typically gives rise to thermally-induced mechanical stresses within the package assembly. Hence, having a CTE value close to semiconductors and heat sink materials are desirable for typical TIMs. For this purpose, we have investigated the CTE behavior of the hybrid nanocomposite TIMs. CTE was measured to be 11pmm/K at 100˚C, which is 40% less than that of pure copper value of 17 ppm/K, indicating the promising potential of the developed material. This value is desirable as it is closer to 2.7 ppm/K for pure silicon than any of the solder materials having values above 20 ppm/K typically or epoxy-based TIMs having values above 30 ppm/K typically. From a broader perspective, CTE values for nanocomposite TIMs are in between silicon and heat sink helping to accommodate expansion on both sides.

CHAPTER IV

EFFECT OF LIGANDS ON THERMAL/MECHANICAL PROPERTIES AND PERFORMANCE AND RELIABILITY COPPER-BASED HYBRID NANOCOMPOSITE TIMS

4.1. Effect of Ligands on the Properties of Copper-based Nanocomposite TIMs

4.1.1. Background

Successful fabrication and characterization of Cu-based organic-inorganic nanocomposite TIMs involving thiosemicarbazide (TSC), as discussed in Chapter III, motivated us to search for other ligands for functionalization of BNNS. Initially, polyethylene glycol dithiol (PEG-D), a free polymeric ligand was added to the process of fabricating the nanocomposite TIMs involving TSC based on the strong interaction potential of thiol functional groups of PEG-D with the metals.[73] Trace amounts of PEG-D (1 wt.%) reduced the elastic modulus and hardness of the nanocomposite TIMs involving TSC about 35% and 29%, respectively, without significantly affecting the thermal properties. The obtained enhanced mechanical and thermal results in presence of the free ligand indicate that PEG-D strongly bonded to the metal crystals and provided additional enhancement in mechanical compliance of the nanocomposite TIMs (Fig. 23).

In the next step, TSC was replaced with various ligands containing different chemical structures and functional end groups. Based on well-established nitrene functionalization of BNNS[90], ligands with amino groups were selected. Additionally, those with chloride and carboxylic acid functional groups were also chosen for possible functionalization reactions. For the metal-ligand side, main functional group was kept as thiols as well as amine groups.[73] This initial step for replacing TSC with other ligands is defined to be PHASE I, the details of which will be given in Figure 22.

In the first phase of the study, although certain literature and chemistry knowledge were employed, the ligand selection was a trial-error process. In PHASE II, a more detailed selection process was followed by interplay of the three functional groups of ligands, two end groups and the central structure, depending on the nature of the interaction that is the point of interest, i.e. while two of those groups were set to be the same the third one was being switched. Detailed chemical structures of the ligands and the corresponding thermal and chemical properties will be included in the next sections.

4.1.2. Materials and Methods

Hexagonal Boron Nitride, h-BN (98%, APS: 0.5 micron), was received from Lower Friction-M.K. IMPEX Corp, (Mississauga, Ontario, Canada). Sulphuric Acid (H_2SO_4, ACS reagent, 95.0-98.0%), Copper (II) Chloride ($CuCl_2$, 99%), Copper Sulfate pentahydrate ($CuSO_4.5H_2O$, ≥98%), Ethylenediamine Tetraacetic acid (EDTA, 99%), and Polyethylene Glycol Dithiol (PEG-D, M_n: 3,400) were obtained from Sigma Aldrich (St. Louis, MI). N-methlyl-2-pyrrolidone (C_5H_9NO, 99%) (NMP) was obtained from VWR (Radnor, PA). Copper sheets were obtained from McMaster Carr (Elmhurst, IL) and Aluminum substrate was obtained from Metals Depot (Winchester, KY). Silicon wafers (Silicon <100> P/Boron, >5000 ohm-cm, doubleside polish, <10 Angstrom R_a) were received from University Wafer (Boston, MA). Thiosemicarbazide (TSC, CH_5N_3S,

>98%), Terepthalic Dihydrazide (TD, $C_8H_{10}N_4O_2$, >90.0%), 4-mercaptobenzoic Acid (4-MBA, >95.0%(GC)(T)), 4-cyanobenzoyl Chloride (4-CBC, C_8H_4ClNO, >98.0%), and 2-mercapto-5-benzimidazole carboxylic acid (2-MBC, $C_8H_6N_2O_2S$, >97%), 4-nitrobenzoyl chloride (4-NBC, $C_7H_4ClNO_3$, >98.0%), 4-bromobenzoyl chloride (4-BBC, C_7H_4BrClO, >98.0%), p-toluoyl chloride (p-TC, C_8H_7ClO, >98.0%), 4-aminobenzenethiol (4-ABT, C_6H_7NS, 98.0%), 4-mercaptotoluene (4-MT, C_7H_8S, >97%), and 3-mercaptopropionic Acid (4-MPA, $C_3H_6O_2S$, >98%) were obtained from TCI America (Portland, OR).

Covalent functionalization of BNNS with thiosemicarbazide (TSC) and terepthalic dihydrazide (TD) was achieved by the same protocol: BNNS with ligand in NMP were mixed with the ratio of 1:10:100 in weight, and heated. The reaction took place at 170 ˚C for 30 hours under nitrogen flow. The obtained product was dialyzed in NMP for 10 hours to remove the unreacted ligands, followed by centrifugation at 3500 rpm for 15 minutes. Next, the supernatant was removed; the precipitate (functionalized BNNS, f-BNNS) was dried at 75 ˚C in a vacuum furnace for further removal of the remaining NMP from f-BNNS powder.

BNNS were functionalized with 2-Mercapto-5-benzimidazolecarboxylic acid (2-MBA) and 4-mercapto benzoic acid (4-MA) with the same method: The ligand the the BNNS were used at a ratio of 5:1 in weight. The ligand was fully dissolved in H_2O and a trace amount of EDTA was added to the aqueous solution. Then, the BNNS was added to the solution and stirred for 12 hours. The stirred solution was rinsed with 5 liters of H_2O, and to remove the excess ligands, the solution containing 2-MBA was filtered with a 400 nm size filter while that containing 4-MA was filtered with a 250 nm one. The residues were collected and dried at 60 ˚C for 24 hours.

The functionalization protocol with 4-cyanobenzoyl chloride (4-CBC), 4-nitrobenzoyl chloride (4-NBC), 4-bromobenzoyl chloride (4-BBC), p-toluoyl chloride (p-TC), 4-aminobenzenethiol (4-ABT), 4-mercaptotoluene (4-MT), and 3-mercaptopropionic Acid (4-MPA) was the same : BNNS and the ligand were mixed in a flask at a ratio of 1:3 in weight, and kept at 125 ˚C for 96 hours under nitrogen flow. A condenser was connected to the flask to prevent the escape of the evaporated ligand. The product of the reaction was rinsed with ethanol for removal of excess ligand. Then, the residual product centrifuged at 4000 rpm for 15 minutes to remove the remaining ethanol. The final product was dried at 50 ˚C for 24 hours.

The functionalization reactions and possible chemical interactions were verified via ATR-FTIR method. The infrared spectra were measured using a Shimadzu IRPrestige-21 system, further details of which were described in Section 3.2.2.

The electrodeposition of Cu/f-BNNS thin film nanocomposite TIMs involving various ligands (TSC, TSC+PEG-D, TD, 2-MBC, 4-MBA, 4-CBC, 4-NBC, 4-BBC, p-TC, 4-ABT, 4-MT and 3-MPA) were achieved with the same electrolyte solution described in Section 3.2.3. The thin film samples were grown onto aluminum sheets and some of these samples were also grown onto the silicon wafers for contact resistance measurements. Microstructural analysis, and mechanical/thermal characterization of Cu-based nanocomposite TIMs were completed by the same techniques described in Sections 3.2.2, and 3.2.4, respectively.

4.1.3. Results and Discussion

«PHASE I»

Figure 22 illustrates the five types of ligands used for functionalization in PHASE I. These functional groups were especially selected due to their bifunctional nature and the presence of amino groups, which can react with defective sites of BNNS, and cyano, thiol and amino groups, all of which can form complexes with copper.

All functionalization reactions were characterized by FTIR analysis, and the selected FTIR spectra for 2-MBC acid are shown in Figure 23. The comparison of spectra for the pure ligand and ligand functionalized BNNS indicates that the peaks at 1525 cm^{-1}, 1608 cm^{-1}, 1740 cm^{-1}, and a broad peak at 3050 cm^{-1} disappeared upon functionalization reaction, suggesting that 2-Mercapto-5-benzimidazolecarboxylic acid indeed reacted with BNNS (Fig. 23).

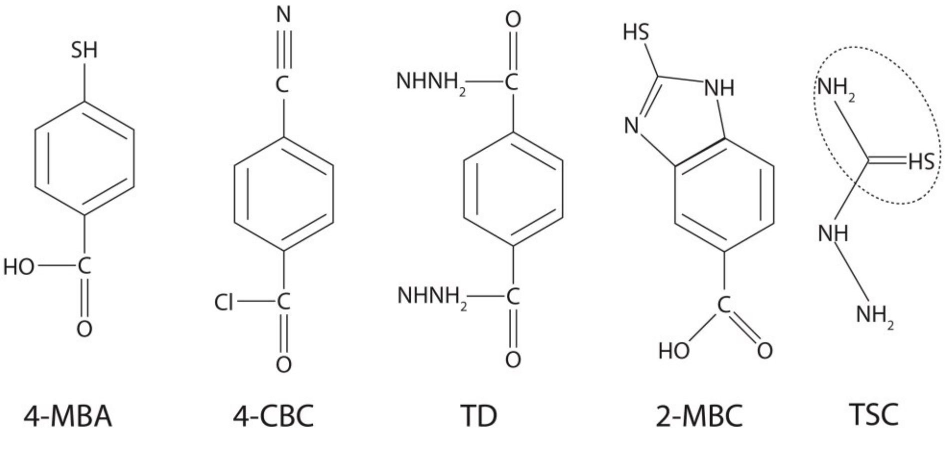

Figure 22. Ligands used in PHASE 1: 4-MBA (4-mercaptobenzoic acid), 4-CBC (4-cyanobenzoyl chloride), TD (terepthalic dihydrazide), 2-MBC (2-mercapto-5-benzimidazole carboxylic acid), and TSC (thiosemicarbazide)

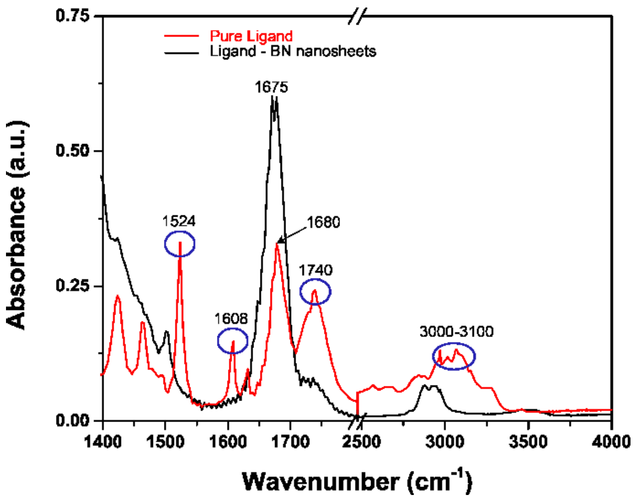

Figure 23. FTIR spectra of pure 2-MBC and f-BNNS with 2-MBC

Figure 24a&b depict the thermal conductivity measurements and nanoindentation test results of the Cu/f-BNNS nanocomposite TIMs, respectively; obtained from the cases of several ligands illustrated in Figure 22. The results from the initial case when PEG-D was added as a free ligand are also compared with the others. It was observed from the figures that the TSC (and TSC with PEG-Dithiol) had the best performance due to highest thermal conductivity, and lowest modulus and hardness value. However, it is important to note that the parametric investigation for each ligand has not yet been performed, which is one of tasks to be completed.

The phase-sensitive transient thermoreflectance (PSTTR) technique, the details were given in Section 3.5.3, was used as the second method to measure the thermal properties of the developed nanocomposite TIMs. For this purpose, the Cu/f- BNNS nanocomposite TIMs with thicknesses in the range of 30-60 µm were electrodeposited onto circular silicon wafers. To maintain the electrical conductivity of the cathode, the Si wafers were initially coated with a 300 nm Cu layer via e-beam evaporation. Figure

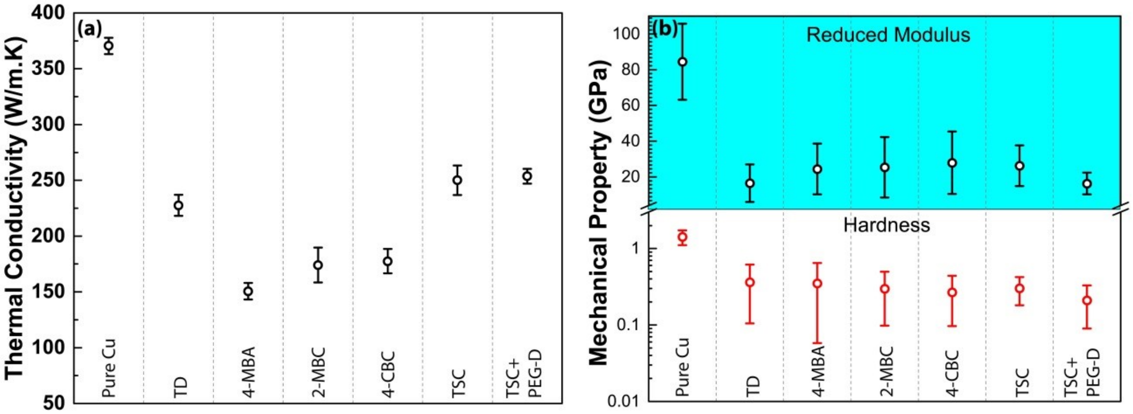

Figure 24. PHASE I: Effect of organic ligands on a) thermal conductivity and b) mechanical properties of Cu/f-BNNS thin film nanocomposite TIMs (Abbreviations: TD-Terepthalic dihydrazide, 4-MBA: 4-Mercaptobenzoic acid, 2-MBC: 2-Mercapto-5-benzimidazolecarboxylic acid, 4-CBC: 4-Cyanobenzoyle chloride, TSC: Thiosemicarbazide, TSC+PEG-D: Thiosemicarbazide with PEG-dithiol)

25a shows the picture of the obtained Cu/f-BNNS nancomposite TIMs involving the TD and TSC. For an initial analysis, Cu/f-BNNS nanocomposite TIMs involving TSC, TSC+PEG-D and TD were measured. Three samples from each condition were measured for error analysis. Contact resistance and overall thermal resistance (sum of the contact resistance at the Si wafer-TIM interface and bulk thermal resistance of the TIM) of the samples are summarized in Table 2a. One sided configuration denotes that the thermal analysis of the samples was performed without sandwiching the TIMs between two Si wafers, as shown in Figure 25b. It is apparent from the results in Table 2a that the single-sided TIM produced with f-BNNS (involving TS functionalization) and 1 wt.% PEG-D gave the minimum overall thermal resistance. It has been shown that TSC has been the best ligand in terms of thermal and mechanical properties among all ligands, in both free standing thermal measurements with DLF and contact resistance measurements with PDTTR. Addition of PEG-D further enhanced the mechanical and thermal properties of the nanocomposite TIMs.

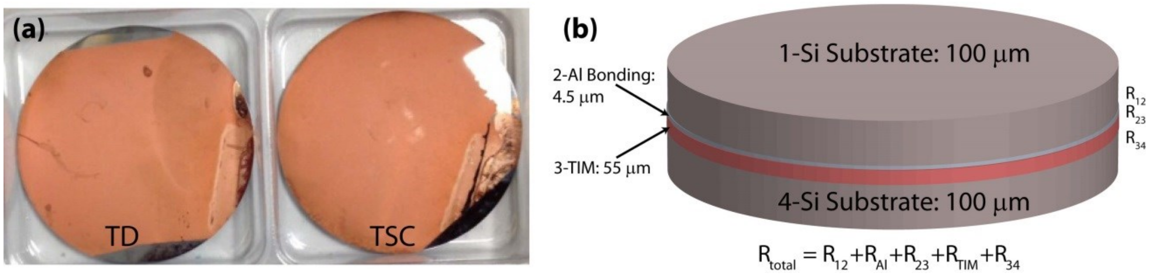

Figure 25. a) Single sided samples that were fabricated by growing Cu/f-BBNS nanocomposite TIMs onto silicon wafers, b) schematic indication of sandwich samples where the single sided samples were attached to a bare silicon wafer with a 4.5 mm aluminum diffusion layer.

Table 2. a) Contact and overall thermal resistance values of pure copper and Cu/f-BNNS thin films involving different ligands (one sided configuration), and b) contact and total thermal resistance values of Cu/f-BNNS nanocomposite TIM involving TS (sandwich configuration). The abbreviations: t: thickness of the TIM, c_p: specific heat capacity, ρ: density, α: thermal diffusivity, K: thermal conductivity, R_{TOT}: overall thermal resistance and R_{12} & R_{23}: thermal contact resistance at Si-Al interface and Al-TIM interface, respectively.

(a) One-sided Configuration

Ligand Type	N/A	Thiosemicarbazide (TS)		TS + PEG-D (for 5 wt.% TS)		Terepthalic Dihydrazide (TD)
Content Type	Pure Cu	f-BNNS		PEG-D		f-BNNS
Concentration (wt.%)		5 wt.%	10 wt.%	1 wt.%	3 wt.%	1 wt.%
Contact resistance ($mm^2 \cdot K/W$)	0.15 ± 0.04	0.1 ± 0.02	0.13 ± 0.03	0.11 ± 0.03	0.17 ± 0.0.3	0.14 ± 0.01
Overall resistance ($mm^2 \cdot K/W$)	0.3 ± 0.02	0.34 ± 0.03	0.32 ± 0.0.1	0.26 ± 0.03	0.3 ± 0.06	0.45 ± 0.01

(b) Sandwich Configuration

t (μm)	c_p (J/kg·K)	ρ (kg/m^3)	α (m^2/s)	K (W/m.K)	R_{12} ($mm^2.K/W$)	R_{23} ($mm^2 \cdot K/W$)	R_{total} ($mm^2 \cdot K/W$)
55	363.1	7026	$7.7*10^{-5}$ ± $5.37*10^{-6}$	196 ± 12.7	0.07 ± 0.01	0.02 ± 0.01	0.47 ± 0.05

The second step of PSTTR measurements was performed with sandwich configuration where the developed TIMs were placed between two silicon wafers and adhered by aluminum diffusion bonding (Fig. 25b). The measurements revealed that the developed nanocomposite TIMs have the lowest measured total thermal resistivity for a TIM with a typical bond line to date, where the minimum value was observed in low melting alloy TIMs.[91]

«PHASE II»

In this phase, a more systematic investigation on functionalization of BNNS with respect to ligand functional groups was performed. Since TSC was determined to be the best ligand in the previous phase, the obtained results from new ligands (Fig. 26) were compared to it. Figure 26a categorizes the selected ligands for metal-ligand interactions into thiol, cyano, bromo, nitro and methyl groups, while the other end group is used in functionalization reaction with BNNS. Moreover, in Figure 26b, setting the metal-ligand interaction group as the thiol, the functional groups that will be employed in functionalization reaction are classified as carboxylic, methyl and amino groups. Finally, the chain structure of the ligands is compared in Figure 26c. 4-MBA, ligand 1, is common for all categories.

Reduced elastic modulus and hardness values of Cu/f-BNNS nanocomposite TIMS involving all abovementioned ligands were obtained and shown in Figure 27, and corresponding thermal conductivity values are depicted in Figure 28. Among all the ligands, mechanical analysis on the nanocomposite TIMs involving TSC and TSC+PEG-D resulted in the lowest elastic modulus and hardness. Mechanical test results of the samples marked as 7 and 8 were close to those of pure Cu, which may be attributed to low affinity of the corresponding ligands (4-MT and 4-MPA) towards the copper matrix. Although these ligands had thiol functional groups, which are known to highly interact with metals, the affinity of the chemical plays a significant role on bonding of the structures.

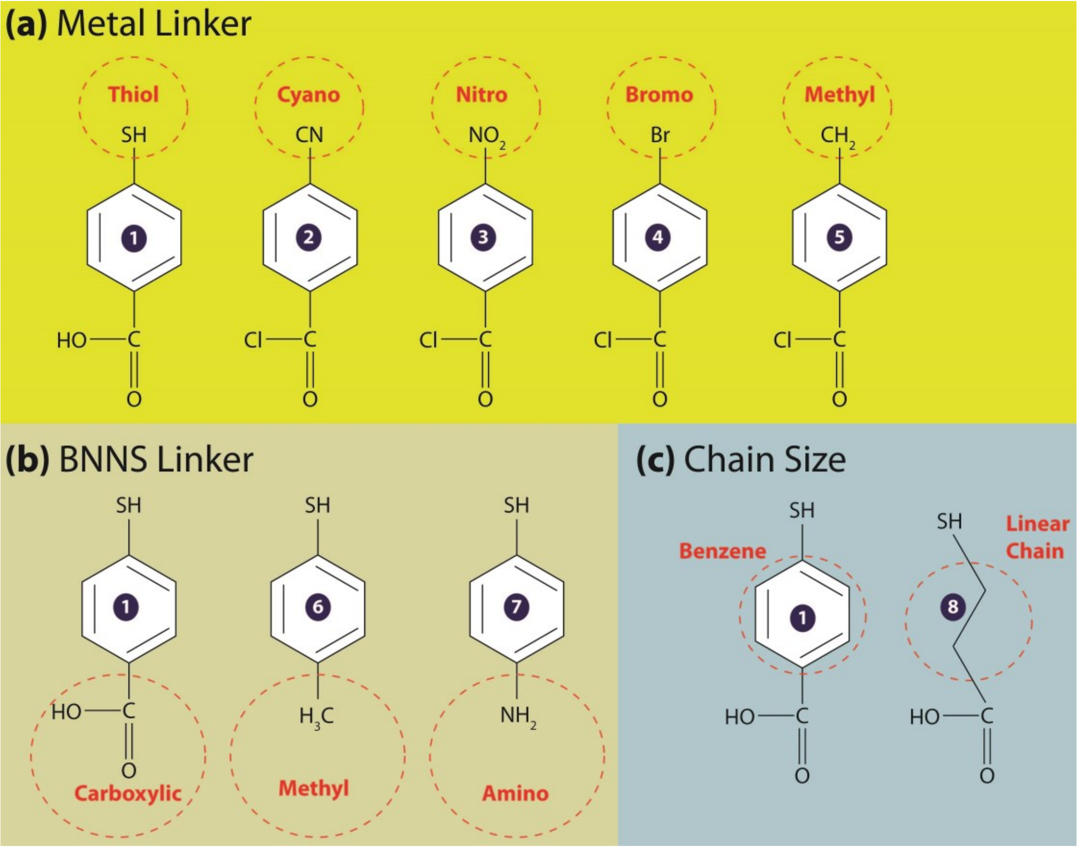

Figure 26. Types of ligands in PHASE II with respect to their functional groups: In Category a) five ligands with varying groups to link to the metal crystals, in Category b) three ligands that may be bonding with the filler, BNNS, and in Category c) ligands having different chain size or central functional group. **Numbering: 1)** 4-MBA (4-mercaptobenzoic acid), **2)** 4-CBC (4-cyanobenzoyl chloride), **3)** 4-NBC (4-nitrobenzoyl chloride), **4)** 4-BBC (4-bromobenzoyl chloride), **5)** p-TC (p-toluyl chloride), **6)** 4-ABT (4-aminobenzenethiol), **7)** 4-MT (4-mercaptotoluene), and **8)** 4-MPA (3-mercaptopropionic Acid). Ligand 1 (4-MBA) is common in all categories.

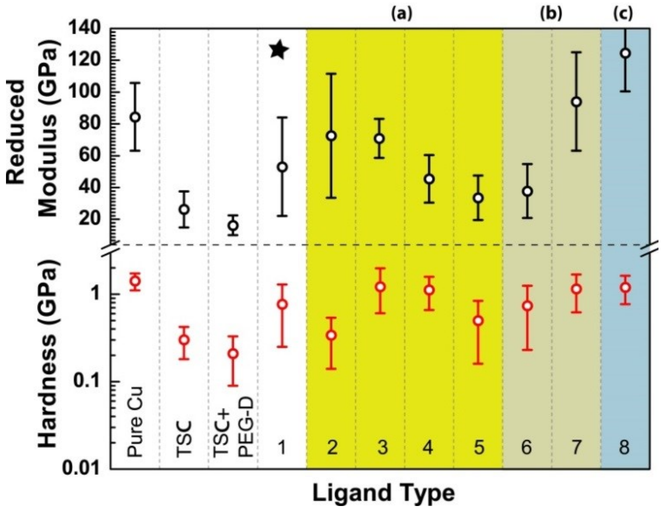

Figure 27. PHASE II: Effect of organic ligands on mechanical properties of Cu/f-BNNS thin film nanocomposite TIMs. **Numbering: 1)** 4-MBA (4-mercaptobenzoic acid), **2)** 4-CBC (4-cyanobenzoyl chloride), **3)** 4-NBC (4-nitrobenzoyl chloride), **4)** 4-BBC (4-bromobenzoyl chloride), **5)** p-TC (p-toluyl chloride), **6)** 4-ABT (4-aminobenzenethiol), **7)** 4-MT (4-mercaptotoluene), and **8)** 4-MPA (3-mercaptopropionic Acid). Ligand 1 (4-MBA) was marked with a star since it is common and compared with all categories.

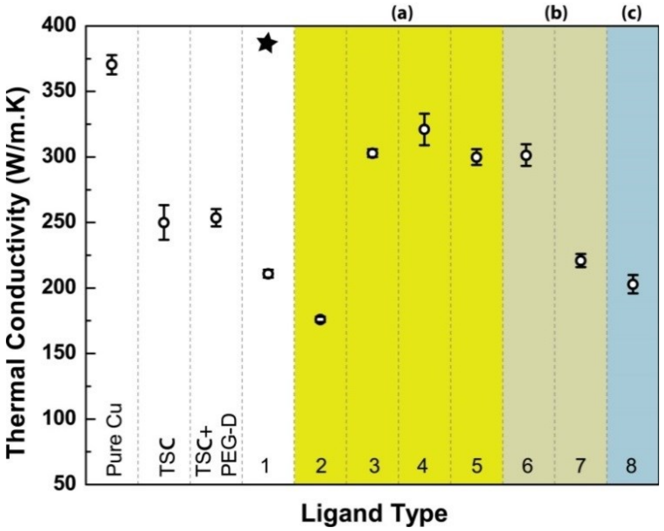

Figure 28. PHASE II: Effect of organic ligands on thermal conductivity of Cu/f-BNNS thin film nanocomposite TIMs. **Numbering: 1)** 4-MBA (4-mercaptobenzoic acid), **2)** 4-CBC (4-cyanobenzoyl chloride), **3)** 4-NBC (4-nitrobenzoyl chloride), **4)** 4-BBC (4-bromobenzoyl chloride), **5)** p-TC (p-toluyl chloride), **6)** 4-ABT (4-aminobenzenethiol), **7)** 4-MT (4-mercaptotoluene), and **8)** 4-MPA (3-mercaptopropionic Acid). Ligand 1 (4-MBA) was marked with a star since it is common and compared with all categories.

It is seen from Figures 27 and 28 that the nanocomposite TIMs corresponding to ligands 5 (p-TC) and 6 (4-ABT) gave comparatively better values than their counterparts in terms of higher thermal conductivity and lower elastic modulus/hardness. Although it is difficult to draw conclusions from the chemical and thermomechanical characterization results, some intuitive results can be obtained from microstructural analysis of the nanocomposite TIMs. Figure 29 depicts the secondary electron micrographs of the selected nanocomposite TIMs involving the ligands 1, 5, 6 and 8. One ligand from each category (Fig. 26) was chosen and the dispersion behavior of f-BNNS in the metal matrix was investigated. It is shown in Figure 29a that the f-BNNS involving ligand 1 is aggregated at grain boundaries with tiny clusters. In Figure 29b&c, for ligands 5 and 6, the filler are shown to have less aggregation and more uniform dispersion, which the more promising thermomechanical test results can be attributed. In Figure 29d, the filler tends to aggregate at certain locations of the nanocomposite at low concentrations. Low level of attachment may be due to the low affinity of the ligand to the metal matrix, which may explain the sample`s mechanical properties similar to pure

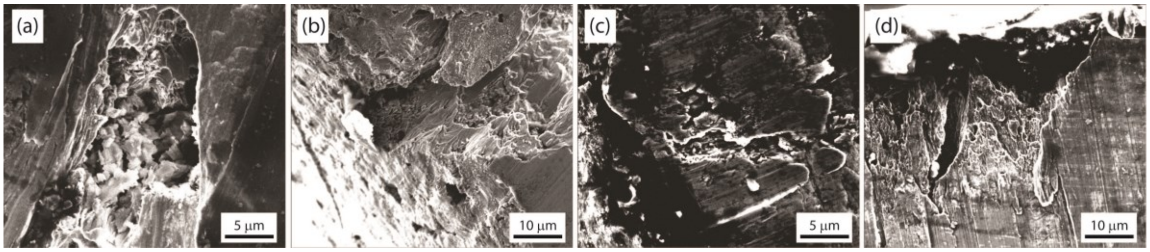

Figure 29. Secondary electron micrographs of the Cu/f-BNNS nanocomposite TIMS involving a) 4-MBA (ligand 1), b) p-TC (ligand 5), c) 4-ABT (ligand 6), and d) 4-MPA (ligand 8)

Cu. On the other hand, its low thermal conductivity may be because of the aggregation and phonon scattering behavior of the ligands (see Chapter III for more detailed discussion on phononic thermal transport).

4.2. Effect of Ligands on Cooling Performance of Nanocomposite TIMs

The most important task of a thermal interface material is to efficiently cool down an electronic system. Hence, cooling performance of TIMs plays a crucial role in their commercial value. Cooling performance of the nanocomposite TIMs was measured using a simple setup where the TIM was placed between an old electronic component and a heat sink, which were disassembled from an old server. The electronic component was heated to 65 °C and its cooling process was observed with an infrared thermal camera (FLIR A655ss IR Camera). The time it takes to cool down the component to 45 °C was recorded for each TIM. The camera records of the thermal performance tests are in the link below:

https://www.youtube.com/watch?v=EJl_XJNhJgo

As an initial evaluation, three samples were compared: (i) first record was taken in absence of a TIM, (ii) a commercially available TIM was tested, and (iii) finally the response from the fabricated nanocomposite TIM (Cu/f-BNNS involving TSC) was recorded. The records indicate that this process took 14:28 seconds, 7:34 seconds and 4:63 seconds with bare heat sink, commercial TIM and our nanocomposite TIM, respectively. Hence, we obtained a 40% higher performance with the developed nanocomposite TIM than the commercial one.

Effect of ligands on cooling performance of the nanocomposite TIMs was also observed following the initial evaluation. The nanocomposite TIMs involving the ligands that were investigated in PHASE I (TSC, TSC+PEG-D, TD, 4-CBC, 2-MBC, 4-MBA) were placed between two mating surfaces and cooling time of each TIM was recorded as shown in the video below;

https://www.youtube.com/watch?v=OpycWTRi-Pc

The shortest cooling time, 5.14 seconds, was obtained by the TIM involving TSC as it resulted in the most promising thermomechanical results. In was unexpected that the sample corresponding to TSC+PEG-D showed lower performance with a cooling time of 11.27 seconds, while that corresponding to 4-CBC cooled down the system in 6.09 seconds.

In summary, the nanocomposite TIMs produced in this project worked very well and gave rise to higher cooling performance than other commercial TIMs. It also needs to be claimed that the commercial TIM used in this experiment contains adhesives that help firmly stick to the heat sink surface and reduce thermal resistance. On the other hand, our nanocomposite TIM did not contain any adhesives, which introduced a higher thermal contact resistance than its commercial counterpart. As a further development of cooling performance, direct deposition of the nanocomposite TIMs on to heat sink/chip surfaces would eliminate the contact resistance. By this way, we expect to further enhance the cooling performance of the nanocomposite TIMs.

4.3. Corrosion Protection Behavior of Nanocomposite TIMs

4.3.1. Background

Corrosion is described as a chemical/electrochemical interaction of a material with the environment causing gradual destruction of the properties of this material, especially metals. It is a significant issue in numerous industries including automotive, energy, aviation, shipping, infrastructure, and electronic industries,[92,93] and its annual cost to U.S. economy is hundreds of billions of dollars.[92,94]Extensive researches have been conducted to inhibit the corrosion in metal surfaces via protective layer coating. In the last few decades, chemically stable and corrosion resistant platinum group metals,[95] electro-active conducting polymers[96,97] and self-assembled monolayers[98] have been used as corrosion resistant coatings on metal surfaces despite their drawbacks such as limited availability, high temperature instability and alteration of the surface properties of metals.[99] Graphene has recently been introduced as an effective corrosion protection material[100–102] on various metals such as copper, gold and nickel, in the form of both individual ultra-thin coating and dispersant in protective polymers.[99,103] However, later investigations have indicated that graphene leads to acceleration of corrosion in long term due to possession of defective sites.[104,105] On the other hand, boron nitride nanosheets (BNNS), a structural analog of graphene, have emerged as an outstanding corrosion inhibitor due to its natural hydrophobicity and impermeability, thermal and chemical stability.[106–108] Corrosion protection of metals and polymers has been reported in presence of BNNS: Li et al. prevented the corrosion of copper surfaces by forming a thin layer of BNNS via chemical vapor deposition,[108] while Sun et al. achieved the same task by coating the copper surface with a polymer composite produced by dispersion of BNNS in polyvinyl butyral (PVB).[106] Also, Yi et al. have shown the oxygen-atom corrosion protection of polymers in presence of BNNS coating.[109]

In electronic systems, metallic components are vulnerable to corrosion due to humidity and temperature, which reduces the yield of these components and ultimately cause electrical failures.[110] Thermal interface materials (TIMs) are major components of electronic systems that are designed to prevent overheating of the other components of the system and enhance their lifetime. Hence, TIMs require enhanced corrosion protection to maintain their performance and reliability, which in turn yields high performance of the whole system. Up on this purpose, corrosion performance of the fabricated metal-based nanocomposite TIMs was investigated. Instead of forming a protective layer on these TIMs as reported in the literature, BNNS were incorporated into copper matrix to form a copper-based nanocomposite. The BNNS were initially functionalized with a soft ligand, thiosemicarbazide (TSC), to prevent the aggregation of individual sheets and provide uniform dispersion in the matrix. Then, copper-based nanocomposite TIMs (Cu/f-BNNS) were fabricated via novel electrocodeposition method, in which the nanocomposite TIMs were grown onto aluminum substrates. The corrosion protection properties of Cu/f-BNNS nanocomposite samples were determined by Tafel polarization. Then, the corrosion activity of Cu-based nanocomposite TIMs was also analyzed by high-resolution scanning electron microscopy (HRSEM), and energy-dispersive X-ray spectroscopy (EDX).

4.3.2. Materials and Methods

Thin film nanocomposite TIMs were grown on aluminum sheets. The aqueous electrolyte solutions were prepared by 1 M $CuSO_4.5H_2O$, 1.8 M H_2SO_4, a trace amount of $CuCl_2$, and 1.25 wt.% f-BNNS. Each solution was transferred to the electroplating cell after sonication for homogenous dispersion of f-BNNS. A pure copper sheet (>99%) and a substrate were used as anode and cathode, respectively. The electrical power source was a Nuvant Powerstat05 Potentiostat (Nuvant Systems Inc., Crown Point, IN). The electrodeposition was carried out at a current density of 10 A/dm^2 and AC frequency of 950 Hz with 30% off time.

All the electrochemical measurements were performed using the Gamry Instruments potentiostat (Interface 1000 model), in a standard three electrode system at 298 K. An aerated solution of 3.5 wt.% NaCl was used as electrolyte throughout the study. The electrochemical cell consists of copper or copper metal matrix composite with an exposed area of 1 cm^2 served as the working electrode, a saturated Ag/AgCl electrode as the reference electrode, and a Pt/Nb mesh electrode of 2 cm diameter as the counter electrode. The working electrode was immersed in the testing solution for 1 hour to reach a quasi-stationary value of the open circuit potential prior to measurement. The potentiodynamic polarization measurements were carried out in the potential range from -300 mV to +300 mV vs open circuit potential with the scanning rate of 0.5 mV/s. All the experiments were repeated for at least 3 times to ensure good reproducibility of the results.

The corrosion current densities (i_{corr}) were determined by extrapolating the linear portion of the anodic polarization curves to E_{corr}. The corrosion rate (CR) was calculated from the corrosion current by using the following equation:

$$CR = 3.268\, x\, 10^{3}\, \frac{Jcorr}{\rho}\left(\frac{MW}{Z}\right) \qquad [8]$$

where MW is molecular weight of copper in g, ρ is the density of Cu (8.92gcm^{-3}) and Z is the number of electrons transferred.

The microstructures of samples before and after polarization were examined using a high-resolution scanning electron microscopy (Tescan LYRA-3 Model GMH Focused Ion Beam Microscope) at an accelerating voltage of 20.0 kV. Additionally, elemental mapping were also performed using energy-dispersive X-ray spectroscopy (Standard EDS Microanalysis System with X-MaxN 50) to determine the presence of each atom in both cases.

4.3.3. Results and Discussion

Figure 30 presents the potentiodynamic polarization curves of pure copper and Cu/f-BNNS nanocomposite TIMs obtained from electrochemical tests. Appearance of lower peak corresponding to Cu/f-BNNS nanocomposite TIM suggests the lower corrosion current passing through the sample, which can be attributed to better anticorrosion performance of Cu/f-BNNS sample than that of pure copper. Corrosion rates that were calculated by using the obtained inputs from electrochemical tests are depicted in Table 3. The corrosion rate of Cu/f-BNNS samples (0.0204±0.005 mmy^{-1}) were found to be near 72% less than that of pure Cu samples (0.0737±0.005 mmy^{-1}), which indicates the superior corrosion performance of the nanocomposite TIMs in presence of f-BNNS.

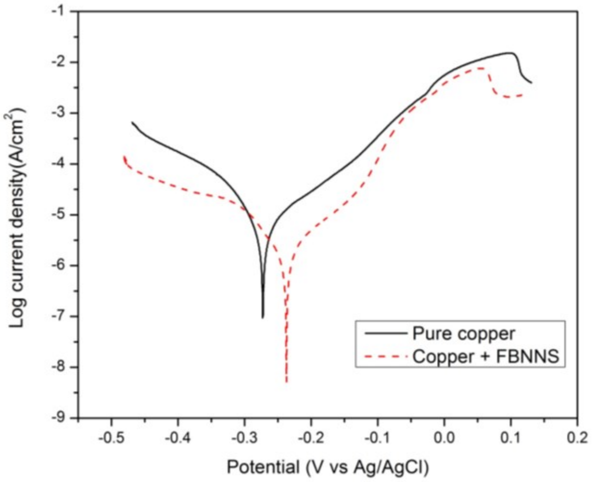

Figure 30. Potentiodynamic polarization curves for a) pure cupper and b) Cu/f-BNNS nanocomposite TIMs

Table 3. Summary of experimental parameters and calculated corrosion rate: E_{corr} represents the potential, J_{corr} is the current density, and β_c and β_a are cathodic and anodic slopes, respectively.

Sample	Parameters				
	E_{corr} (mV)	J_{corr} (μAcm^{-2})	β_c ($mV.dec^{-1}$)	β_a ($mV.dec^{-1}$)	Corrosion rate (mmy^{-1})
Pure Cu	-271	6.33	-143	105	0.0737 ± 0.005
Cu/f-BNNS	-227	1.75	-177	65	0.0204 ±0.005

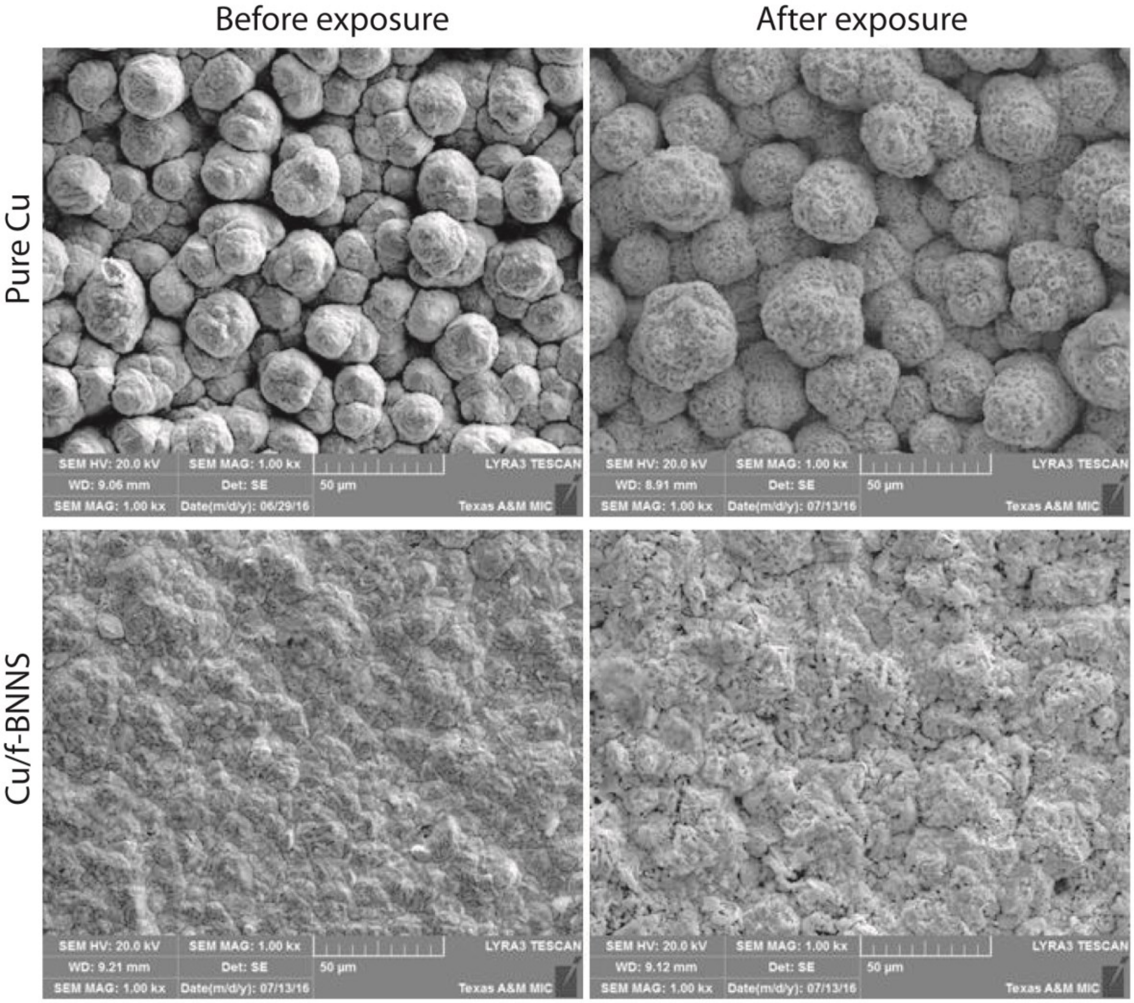

Figure 31. High resolution SEM images obtained from the Pure Cu and Cu/f-BNNS nanocomposite TIMs before and after electrochemical tests

Figure 31 shows the high resolution secondary electron micrographs of the pure Cu and Cu/f-BNNS nanocomposite samples obtained before and after the electrochemical tests. The pure Cu sample has a rough surface and contains numerous pores and grain boundaries, while these vacancies were filled with the f-BNNS in the Cu/f-BNNS nanocomposite TIM. It is clear from the micrographs that the surfaces of both samples were deteriorated upon exposure to the NaCl during the electrochemical test. The degree of deterioration in the Cu/f-BNNS nanocomposite sample is shown to be less severe than that of pure Cu sample, which can be attributed to the enhanced corrosion performance of the nanocomposite sample.

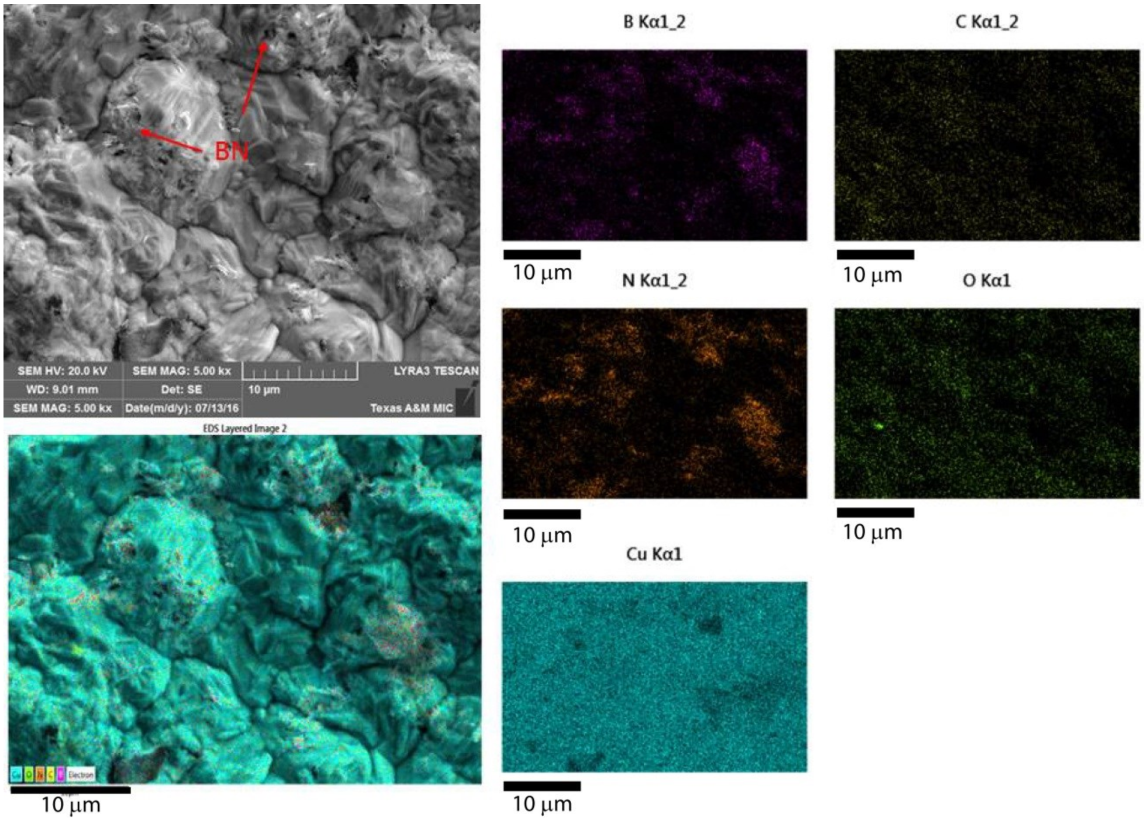

Figure 32. Microstructural analysis before polarization: High resolution FIB microscopy images of Cu/f-BNNS nanocomposite TIMs (left) and EDX mapping of each individual element on these samples (middle and right)

Figure 32 presents the high resolution FIB images of the Cu/f-BNNS nanocomposite sample taken before polarization (two images on the left). The f-BNNS at the copper grain boundaries are obviously shown in the images. To verify the presence of the elemental mapping for each atom was performed via EDX method. In addition to

B, N and Cu atoms, the C and O mapping was obtained to confirm the ligand TSC (middle and right). These maps show that all of the constituents of the nanocomposite, i.e. copper crystals, the filler BNNS and the ligand TSC, are present in the nanocomposite structure. On the other hand, Figure 33 demonstrates the images obtained after polarization, where there is an apparent microstructural change due to application of aerated NaCl solution. The FIB images show higher number of pores after exposure than those before exposure that might be due to disappearance or reorientation of some constituents of the nanocomposite. Detailed information on the microstructural changes

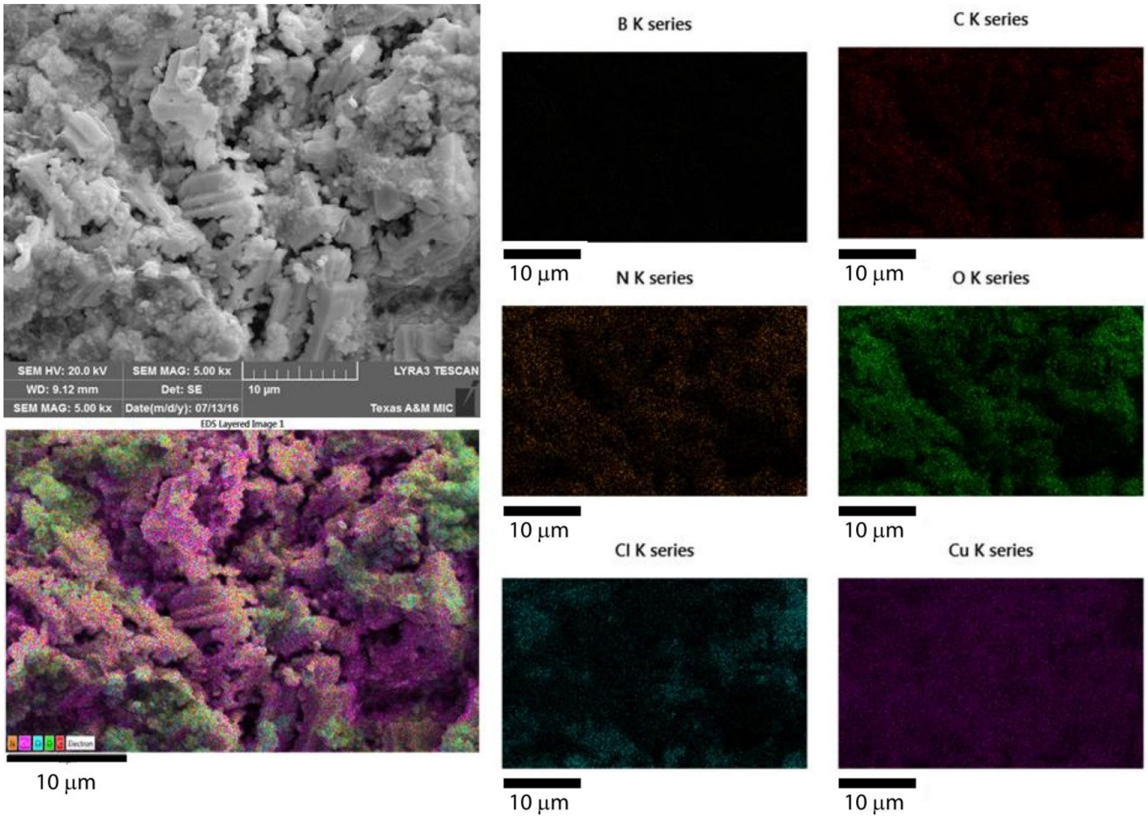

Figure 33. Microstructural analysis after polarization: High resolution FIB microscopy images of Cu/f-BNNS nanocomposite TIMs (left) and EDX mapping of each individual element on these samples (middle and right)

was attained from the elemental mapping images. Cl atom was added to the elemental mapping to show the effect of NaCl on the sample surfaces. After the polarization the boron atoms could not be detected while other elements maintained their presence on the nanocomposite. The possible reason is that the active sites of TSC bind preferentially with copper complexes during the corrosion process, which later causes leaching of the BNNS into the electrolyte. Since the mapping was obtained within 1-2 µm depth from the surface of the nanocomposite, we can state that the BNNS still remain in the copper matrix at high concentrations. However, contribution of TSC to the corrosion performance increased at the expense of BNNS.

4.3.4. Conclusions

Electrochemical analysis indicates that the dispersion of f-BNNS in the copper matrix enhanced the corrosion protection of the TIMs. Surface morphology of the pure Cu and nanocomposite samples was evaluated by high resolution microscopy to obtain a fundamental understanding on the behavior of the samples before and after the corrosion tests. It was concluded from the EDX analyses that the strength of the BNNS-TSC interaction was insufficient to hold the BNNS on the nanocomposite surface while a significant percentage of BNNS still remains dispersed in the metal matrix.

CHAPTER V

EFFECT OF LIGANDS ON THERMAL AND MECHANICAL PROPERTIES OF SILVER-BASED HYBRID NANOCOMPOSITE TIMS

5.1. Introduction

While copper-based nanocomposite TIMs have been the point of focus in the prior chapters of this study, silver-based nanocomposite TIMs will be examined in this chapter. Similar to the method that was used for fabrication of copper-based TIMs, electrocodeposition was a promising approach to create silver-based nanocomposite TIMs involving functionalized BNNS. The electrodeposition setup was modified by replacing the copper anode with silver and $CuSO_4$, the copper salt, to alkali cyanides for silver layer growth on aluminum substrates. Next sections will discuss the functionalization of BNNS with ligands having high affinity to silver matrix, fabrication of Ag-based nanocomposite TIMs and their characterization experiments.

5.2. Background

When two metal surfaces come into contact, the nominal contact area is much smaller than the desired level due to surface roughness and asperities of each surface even when they are in a nanometer scale. The reduced contact area significantly prevents heat transport across this interface. Effective heat dissipation and thermal management is a major issue in most high-tech electronic devices such as personal laptops, supercomputers and smart phones. In addition to the reduced contact area, thermal boundary resistance which stems from electron/photon scattering due to contact mismatch also contributes to inefficient thermal transport.[51] Furthermore, quantum confinement effect at micro-/nano-contacts lead to dispersion of phonons and electrons, which hinder the heat transfer across the boundary.[52] Thermal Interface Materials (TIMs) have been developed to solve these problems. TIMs are expected to be sufficiently soft to conform to the asperities, and reduce the thermal interface resistance.

Technological advances have led to manufacturing of electronic devices that are smaller in size, more powerful, and thus dissipating higher amounts of heat. Current TIMs have failed to keep pace with the increased need of thermal transport. Hence, new types of TIMs, which possess higher thermal conductivities and similar mechanical compliance compared to the conventoinal current TIMs. are required to overcome this issue. Traditional appraoches to develop new class of TIMs have been to incorporate graphene, CNT and several thermally conductive particles[55–62] to soft matrices such as polymers, silicon oil and hydrocarbon oil.[53–55] We have recently shown metal-based nanocomposite TIMs, fabrication of which was achieved by dispersion of ligand functionalized BNNS in copper matrix. These novel type TIMs had superior thermal properties and comparable mechanical compliance over their commercial counterparts (*See Chapter III for details*). As a next step on further improving the thermal/mechanical properties of the developed TIMs, metal matrix was switched to silver due to having softer nature and higher thermal conductivity than those of copper. Silver-based nanocomposite TIMs involving the dispersion of soft ligand functionalized BNNS were produced via electrodeposition technique. For functionalization of BNNS, three out of numerous ligands were selected due to their high reactivity with silver crystals. The effect of these ligands on microstructural, thermal and mechanical properties of the silver-based nanocomposite TIMs was investigated.

5.3. Materials and Methods

5.3.1. Materials

Hexagonal Boron Nitride, h-BN (98%, APS: 0.5 micron) was received from Lower Friction-M.K. IMPEX Corp, (Mississauga, Ontario, Canada). Ethylenediamine Tetraacetic acid (EDTA, 99%), Silver Cyanide (AgCN, 99%), Potassium Cyanide (KCN, 99&), and Potassium Dicyanoargentate ($KAg(CN)_2$, 99%) were received from Sigma Aldrich (St. Louis, MI). 4-bromobenzoyl Chloride (4-BBC, >98%), 4-cyanobenzoyl Chloride (4-CBC, >98.0%), and 2-mercapto-5-benzimidazole carboxylic acid (2-MBC, >97%) were received from TCI America (Portland, OR). Sterling Silver sheets were received from Rio Grande (Albuquerque, NM). Aluminum substrate was obtained from Metals Depot (Winchester, KY).

5.3.2. Functionalization Reactions of Ligands

Functionalization of BNNS with 2-Mercapto-5-benzimidazolecarboxylic acid (2-MBC) was achieved by using the ligand and the BNNS with 5:1 ratio in weight. The ligand was fully dissolved in H_2O and a trace amount of EDTA was added to the aqueous solution. Then, the BNNS was added to the solution and stirred for 12 hours. The stirred solution was rinsed with 5 liters of H_2O, and to remove the excess ligands, it was filtered with a 400 nm pore-size filter. Finally, the residues were collected and dried at 60 ˚C for 24 hours.

Same protocol for functionalization with 4-cyanobenzoyl chloride (4-CBC) and 4-bromobenzoyl chloride (4-BBC) was used: the ligand and the BNNS were mixed in a flask with 3:1 ratio in weight, and kept at 125 ˚C for 96 hours under nitrogen flow. A condenser was connected to the flask to prevent the removal of the evaporated ligand. Then, the reacted product was rinsed with ethanol to remove excess ligand, and the residual product was centrifuged at 4000 rpm for 15 minutes for removal of the remaining ethanol. Final product was dried at 50 ˚C for 24 hours.

Confirmation of each functionalization reaction was achieved via Infrared spectroscopy (Shimadzu IR Prestige ATR-FTIR, Shimadzu Scientific Instruments Inc., Columbia, MD)

5.3.3. Fabrication and Characterization of Silver-based Nanocomposite TIMs

Pure silver, silver with pure BNNS, and silver-based thin film nanocomposite samples involving three ligands (4-BBC, 4-CBC and 2-MBC) were grown onto aluminum substrates with the same procedure as mentioned in Chapter III. The aqueous electrolyte solution was prepared by mixing 3 grams of AgCN and 5 grams of KCN in 100 mL water, and the mixture stirred at 50 ˚C until complete dissolution of the ingredients. Then, 1 gram $KAg(CN)_2$ was added to the stirring solution to increase the cyanide concentration, which increase the conductivity of the solution and also provide the cathode polarization with superior anode corrosion.[111] In addition, the alkali cyanide has been known to facilitate the formation of silver complex ions, which minimizes undesired carbon content in the film. The solutions were transferred to an electroplating cell and, a pure silver sheet and an aluminum substrate were placed as anode and cathode, respectively. Same AC power source (noted in Section 3.2.3) with the same experimental parameters was employed. Since, the filler concentration in the electrolyte solution directly affects the filler loading of the nanocomposite samples; we perturbed the f-BNNS content in the solution to maintain same filler loading in the samples (10-13% in volume). Upon fabrication, the nanocomposites were thoroughly rinsed with water and dried.

Attachment of f-BNNS onto metal was confirmed via X-ray photoelectron spectroscopy. Synthesized Ag-based nanocomposite TIMs were mounted on to a copper tape and placed on an Omicron XPS (Scienta Omicron GmbH, Taunusstein, Germany). High resolution XPS spectra were carried out for Ag and C atoms. Microstructural analysis, mechanical and thermal characterization of Ag-based nanocomposite TIMs were completed by secondary electron microscopy (SEM), laser flash diffusivity (LFD) and nanoindentation techniques, respectively, the details of which were described in Sections 3.2.2, and 3.2.4.

5.4. Results and Discussion

It was shown in the previous chapters that the most promising Cu-based nanocomposite TIMs were obtained in presence of thiosemicarbazide (TSC). However, although both copper and silver are in the same group of the periodic table, TSC-functionalized BNNS interacted with Ag matrix in a different way during electrocodeposition: the integrity of nanocomposites was deteriorated instead of improving in presence of TSC-functionalized BNNS. One possible reason for this difference could be that the standard electrode potential of silver (+0.800 V) is much higher than that of copper (+0.340 V), enabling different oxidation and reduction reactions with ligands.[41] Thus, next step on fabricating Ag-based nanocomposite samples was to parametrically study the affinity of some other ligands. To this end, three different types of ligands were utilized as illustrated in Figure 34. These functional groups were specifically selected due to their bifunctional nature and the presence of thiol, bromo, and cyano groups, all of which can form complexes with silver.

Initially, functionalization of BNNS was achieved with ligands having the same reaction schemes. 4-bromobenzoyl chloride (4-BBC), 4-cyanobenzoyl chloride (4-CBC) and 2-mercapto-5-benzimidazole carboxylic acid (2-MBC) were selected to be the ligands. Figure 34a divides the ligands into three parts, two functional groups (Parts A and C) and a central structure (Part B). The functional group 1 was selected to react with BNNS with a same type of functionalization, and the second functional group to interact with the metal crystals. These two groups play a major role in electron-phonon coupling and phononic transport at the BNNS and metal interface, respectively. It has been reported that interfacial bond strength affects the thermal transport across the metal and inorganic interfaces,[73,112–114] which comprises the interactions on these two functional groups. Considering the most important factor contributing to the thermal transport is metal-linker interaction, functional group 1 and the central structure were kept constant and the functional group related to metal-ligand complex was varied. As such, the effect of the interfacial bond strength at metal-ligand interface on nanocomposite properties could be determined. While 4-CBC and 2-MBC (Fig. 34b and c, respectively) can chemically interact with the metal and form coordination/semi-covalent bond, 4-BBC (Fig. 34d) can physically adsorb onto the metal crystals. This is because the cyano and mercapto (thiol) groups of 4-CBC and 2-MBC can form the chemical interaction while the bromo group of 4-BBC does not provide it. Comparison of 4-BBC to 2-MBC or 4CBC may result in different physical adsorption versus chemical adsorption/reaction, while comparing 2-MBC with 4-CBC can suggest how the strength of chemical interaction affects the nanocomposite properties. Despite the other possible synergistic effects that may influence the properties for organic linkers with significantly different electronic structure distribution, this study aims to determine the expected general trend.

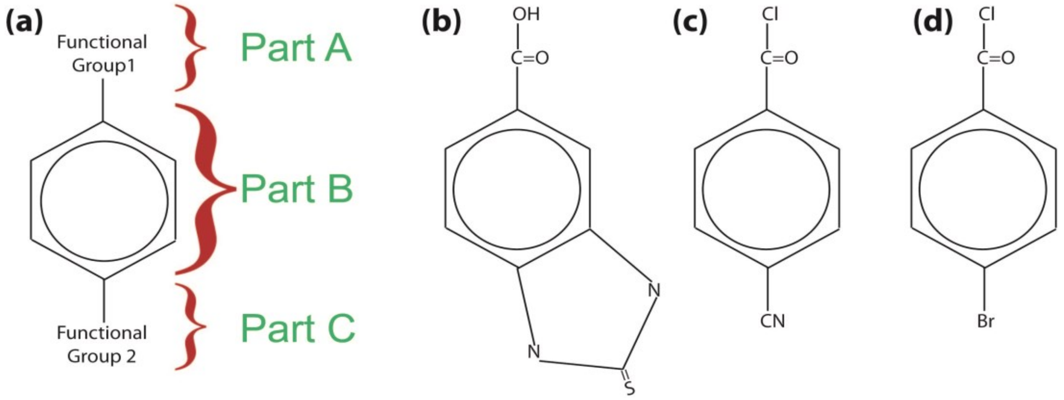

Figure 34. a) Chemical structure of ligands used for metal-ligand-filler bonding. Part A (Functional group 1): Chloride or carboxyl groups which interact with BNNS in a same way, Part B (Central structure): Benzene ring that was constant for all ligands and Part 3 (Functional group 2): Thiol, cyano and bromo groups to interact with Ag crystals. The ligands are b) 2-Mercapto-5-benzimidazolecarboxylic acid (2-MBC), c) 4-cyamobenzoyl chloride (4-CBC) and d) 4-bromobenzoyl chloride (BBC).

Functionalization reactions related to the abovementioned ligands are confirmed with FTIR spectroscopy. Figure 35a shows the FTIR spectroscopy of pure ligand (2-MBC) and filler (BNNS), and functionalized filler with 2-MBC (2-(MBC)-(BNNS)). The shift of peak from 1724 cm^{-1} to 1628 cm^{-1} corresponding to carbonyl group suggests the shift from acid to amide in pure 2-MBC to 2-(MBC)-(BNNS). This is possible because inorganic amine groups of BNNS react with carboxylic acid group of 2-MBC via condensation. Also no change in peaks at 763 cm^{-1} and 2357 cm^{-1} corresponding to C=S (thio urea) and SH (thiolate form) indicate the intact presence of the central structure of the ligand group. The expected reaction scheme related to this functionalization is presented in Figure 35b. FTIR spectra and the corresponding reaction scheme related to the functionalization of 4-CBC are also depicted in Figures 35c and. The shift of peak from 1740 cm^{-1} to 1680 cm^{-1} in between pure 4-CBC and 4-(CBC)-(BNNS) suggests that the reaction occurred at carbonyl group that changes carbonyl chloride into amide. Besides, the peak corresponding to cyano group is unchanged at 2330 cm^{-1} suggesting that there is no change in this group. Moreover, the infrared spectra and the reaction scheme of 4-BBC are given in Figures 35e and f. It is observed that the peak shift from 1766 cm^{-1} to 1651 cm^{-1} (Fig. 35e) corresponds to carbonyl chloride of pure 4-BBC and amide group of 4-(BBC)-(BNNS), respectively. Also, the stationary peak at 636 cm^{-1} corresponding to C-Br suggests the unchanged bromo group. It was eventually confirmed that 2-MBC, 4-CBC and 4-BBC all attach to BNNS via same type of interaction, which will result in the same bond strength. On the other hand, having the mercapto, cyano and bromo groups for metal-ligand interaction, these ligands will react differently while forming the nanocomposite TIMs.

As the next step, X-ray photoelectron spectroscopy (XPS) was employed to verify the ligand-metal interactions. XPS spectra of pure Ag, Ag/BNNS and the three ligands were obtained (Fig. 36). The results verify the expected chemical interaction of 2-MBC and 4-CBC with silver atoms whereas no evident chemical interaction was observed between BNNS and 4-BBC. This is a clear conclusion since two peaks corresponding to composites 2-(MBC)-(BNNS) and 4-(CBC)-(BNNS) show an oxidized shift of 0.25 eV in silver $3d_{5/2}$ peak. However, the composites Ag/BNNS and 4-(BBC)-(BNNS) indicate no such oxidized states of silver.

Figure 37 indicates the pictures taken from the pure Ag, Ag/BNNS and three Ag/f-BNNS nanocomposite TIMs, and the corresponding SEM images. The filler material, either in bare or functionalized form, is observed in grain boundaries of the silver crystals in all of the samples. Figure 37b and c show that the filler materials were trapped in the grain boundaries, i.e. they were poorly adsorbed without chemical integration. However, the filler material involving 4-CBC (Fig. 37d) and 2-MBC (Fig. 37e) have shown better integration with the silver matrix, which agrees well with the XPS spectra.

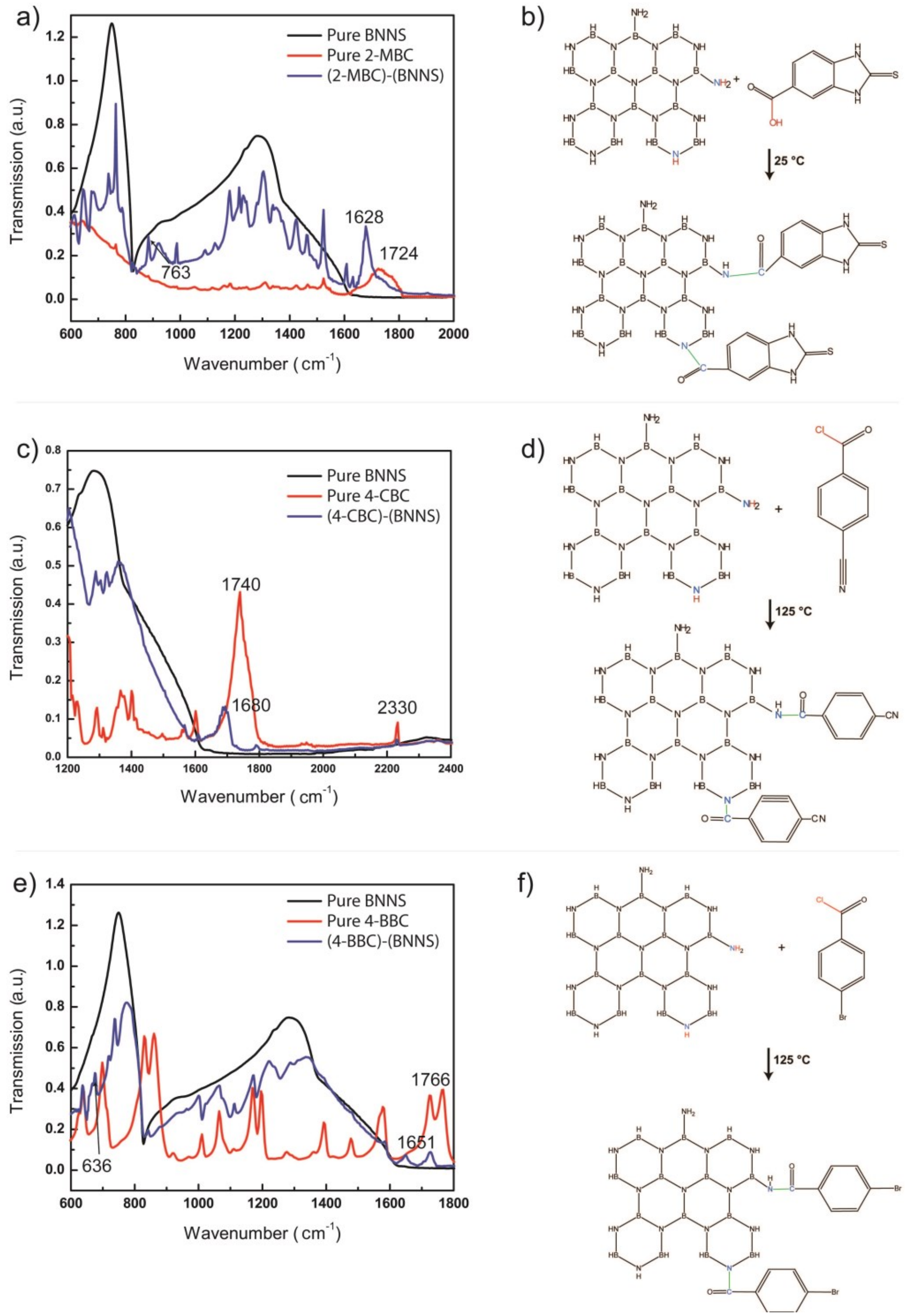

Figure 35. FTIR spectra and corresponding functionalization reaction schemes for the ligands utilized in functionalization of BNNS: a-b) 2-Mercapto-5-benzimidazolecarboxylic acid (2-MBC), c-d) 4-cyamobenzoyl chloride (4-CBC) and e-f) 4-bromobenzoyl chloride (BBC)

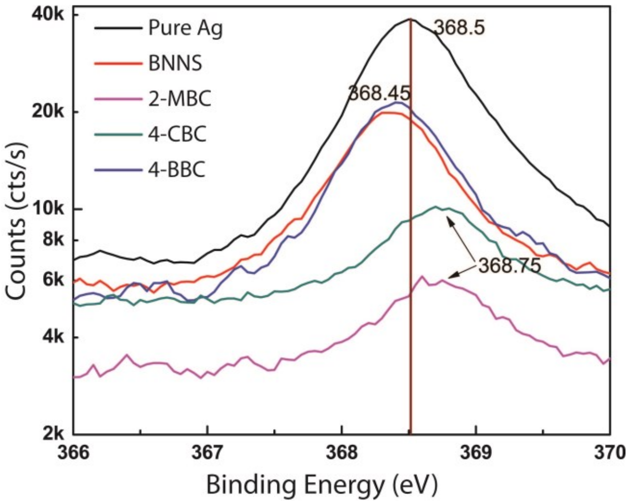

Figure 36. X-ray photoelectron spectra (XPS) of Pure Ag, bare BNNS, 2-MBC, 4-CBC and 4-BBC

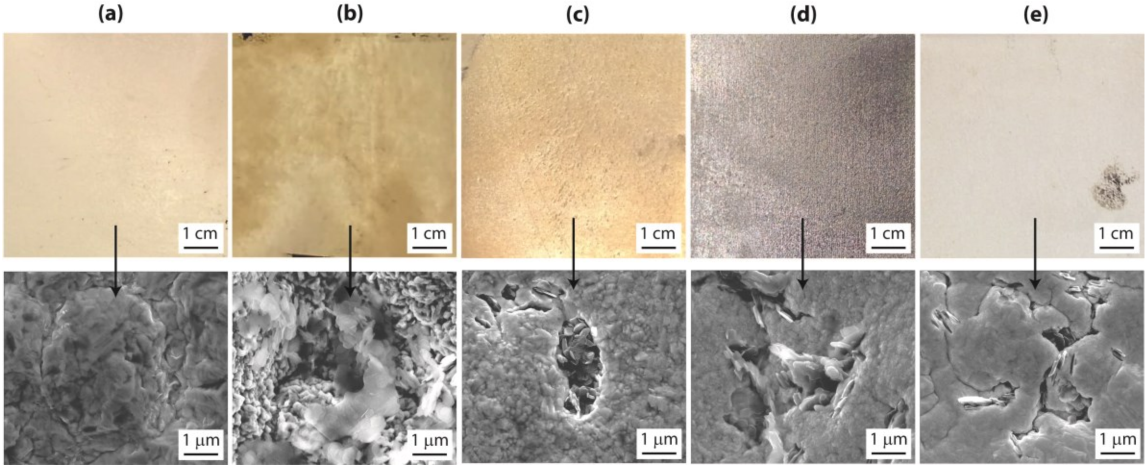

Figure 37. Photos obtained from the silver-based nanocomposites and corresponding SEM images for a) Pure Ag, b) Ag/Pure BNNS, c through e) Ag/f-BNNS involving 4-bromobenzoyl chloride (4-BBC), 4-cyanobenzoyl chloride (4-BBC), and 2-mercapto-5-benzimidazole carboxylic acid (2-MBC).

Thermal conductivity and mechanical properties of the Ag-based nanocomposite TIMs were attained as demonstrated in Figure 38. As the most promising type of nanocomposite TIM that have been developed this project, the nanocomposite properties of Cu/f-BNNS involving TSC were also added to the figures for comparison. It can be stated from Figure 38a that ligand-metal interaction strongly influences the thermal properties. BNNS can be functionalized with the ligands from the defective sites at the edges, hence the phonon transport occurs along the surface of the BNNS, in which the thermal conductivity is higher than 1000 W/m.K.[115] Moreover, bond strength at interface determines the conductivity.[73,114] Strong bonds provide higher thermal conductivities by reducing the acoustic mismatch for phononic conduction. As the f-BNNS disperse in the Ag matrix, they reduce Ag-Ag metallic interaction that hinders the thermal transport. Nevertheless, the electrons can tunnel and travel into adjacent Ag grains due to short length of the ligands. Besides, introduction of f-BNNS contributes to the phononic bandwidth, which can compensate some of the hindered electrical conductivity. An-harmonic electron-phonon coupling at the linker interfaces can also contribute to the thermal transport of the nanocomposite structure.[74,116] Briefly, when f-BNNS are introduced to the metal matrix, they cause the reduction of the electronic thermal transport, but the introduction of phononic transport via BNNS, electronic tunneling at the organic linker interfaces and electron-phonon coupling enable the nanocomposites retrieve some portion of the lost thermal conductivity. The interaction strengths at the filler-ligand and ligand-matrix interfaces significantly affect the quantity of the retrieved thermal conductivity. It is clear from Figure 38a that the nanocomposite TIMs related to 2-MBC have the highest thermal conductivity because they have strong amide and thiol interactions at the BNNS-ligand and ligand-metal interfaces, respectively. Strong linking facilitates high phononic transfer and more electron tunneling. For the nanocomposite involving 4-CBC, having a weaker cyano- interaction at the ligand-metal side results in a reduced thermal conductivity.[117] The nanocomposite related to 4-BBC had the minimum thermal conductivity among the three ligands since these was no chemical interaction at the ligand-metal interface. Weak bonding at this interface acts as a bottle neck to the thermal transport. Also, Ag/f-BNNS involving 4-BBC fillers show marginally lesser thermal conductivity than Ag/BNNS TIMs. This can be attributed to reduced intrinsic thermal conductivity of BNNS as a consequence of the functionalization reaction, and introduction of insufficient phononic contribution to the nanocomposite. Phonons are directed to the direction parallel to the plane of the BNNS upon functionalization, whereas they are more randomly oriented in bare BNNS or BBC-functionalized BNNS. This investigation can be enhanced to the modification of the central structures of the ligands (Part B), but it can be considered to have a negligible influence on the nanocomposite properties due to the length of the ligands that is much shorter than that of metal crystals or fillers. Even though some improvements can be made to Part B of the ligands by introduction of synergistic chain structures which can carry electrons, their contribution to the thermal conductivity will still be several orders of magnitude lower than that of metals.

Figure 5b presents nanoindentation test results of the Ag/f-BNNS nanocomposite TIMs. The reduced elastic modulus and hardness values are high compared to those in Cu/f-BNNS nanocomposite TIM, but a significant improvement on mechanical properties, near three-fold reduction in the stiffness of the pure Ag, was attained. Similar to the thermal properties test results, the nanocomposites with higher chemical integration have more enhanced mechanical test results. As BNNS/f-BNNS settle at the grain boundaries, atomic interactions among silver atoms start to decrease, which in turn leads to the increase in the number of weaker interactions in the metal matrix turning the nanocomposite structure to a softer one.

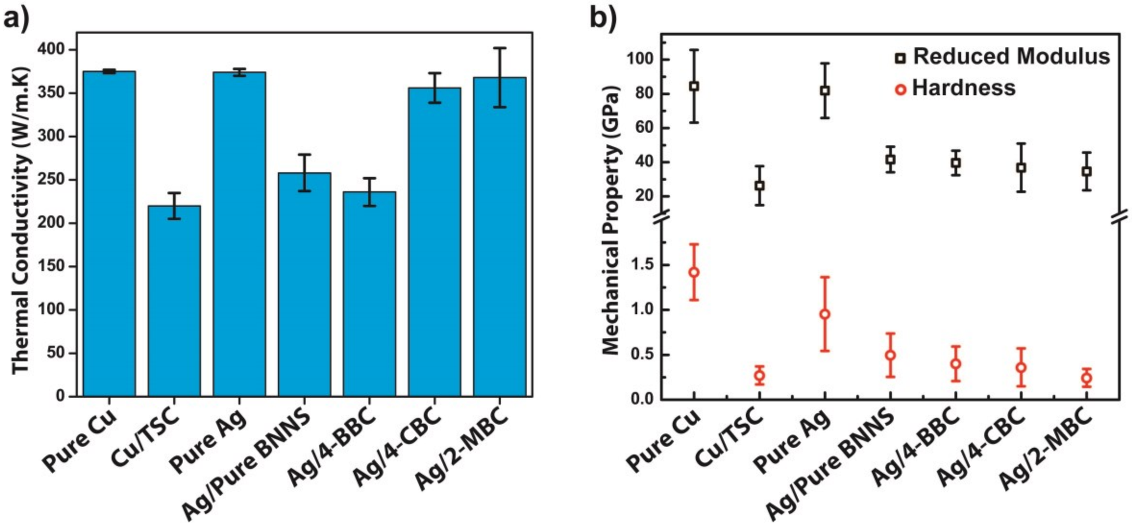

Figure 38. Thermal conductivity and mechanical test results obtained from Pure Ag, Ag/BNNS, and Ag/f-BNNS nanocomposite TIMs involving the ligands 4-BBC, 4-CBC and 2-MBC. The results from Pure Cu and Cu/f-BNNS nanocomposite TIMs involving TSC were also included for comparison

5.5. Conclusions

Ag-based nanocomposite TIMs were fabricated via electrodeposition by using various ligands. These nanocomposite TIMs were around three times more compliant than pure silver, meanwhile they retained the excellent thermal properties of it. Further investigation on these TIMs revealed that the boding strength of the organic ligands that they make with metal crystals directly affects the overall thermal and mechanical properties, i.e. the higher the interaction strength there is at the metal-ligand interface, the higher the thermal conductivity and the better mechanical properties the nanocomposite TIMs will have. It is important to note that, a similar effect can be pronounced if the binding strength of the organic ligand to the filler material is varied by using different functional groups.

CHAPTER VI

SUMMARY AND FUTURE WORK

In Chapter I, a brief overview of thermal interface materials (TIMs) was presented. Significance of the TIMs in electronic systems and thermal management, thermal and mechanical properties of ideal TIMs, production methods and current limitations of traditional TIMs, and the rationale behind selection of a new approach (electrodeposition) to for design and development of metal-based nanocomposite TIMs were discussed.

Chapter II provided a review of electroplating process and electrodeposition of metals. This chapter began with introduction of the electrodeposition process such as types of chemical reactions that occur at the electrodes, elements of an electroplating setup and chemicals used in preparation of the electrolyte solution. Then, physical and electrochemical considerations in electrodeposition were discussed. Those considerations included electrode potential, factors affecting the deposit thickness and quality (current density, diffusion rate, electrolyte concentration, additives and so on), electrodeposition in atomistic level, and possible growth mechanisms (layer deposition, nucleation-coalescence). Furthermore, the details of experimental optimization of electrodeposition were given.

In Chapter III, a comprehensive characterization of copper-based hybrid nanocomposite TIMs involving thiosemicarbazide was given. The significant results obtained in this chapter: Thermally conductive and flexible Cu/f-BNNS nanocomposite

TIMs was fabricated. Elastic modulus values in the range of 15-25 GPa and overall thermal resistance value of 0.45 mm^2.K/W were reported. Compared to the traditional TIMs, much lower thermal resistance and comparable values of elastic moduli were obtained. These results indicate the huge potential of these nanocomposites to be the next generation thermal interface materials.

Chapter IV enhanced the investigation of copper-based hybrid nanocomposites to other organic ligands types, summarized the thermal cooling performance of these TIMs and discussed the corrosion protection behavior of the nanocomposite TIMs developed in the previous chapter. In this first section of this chapter, initially PEG-dithiol was introduced to the hybrid nanocomposite related to thiosemicarbazide, and better mechanical properties were obtained without losing the thermal properties. Then, thiosemicarbazide was replaced with several other ligands and new hybrid nanocomposites were fabricated. Although very good results were obtained from the new TIMs, the nanocomposite involving thiosemicarbazide had the most promising thermal and mechanical properties. This nanocomposite also gave the highest cooling performance in the second section of this chapter. Last section comprised the electrochemical tests and microstructural analysis of the nanocomposite involving thiosemicarbazide. The test results indicated that the presence of f-BNNS reduced the corrosion rate by 72%, even though some portion of BNNS near the surface was detached from the nanocomposite.

In Chapter V, metal matrix was changed to silver and silver-based hybrid nanocomposite TIMs were fabricated with several ligands. Since the new matrix material had a different electrode potential, thiosemicarbazide did not work well. Instead, the nanocomposites were formed via three other ligands, and thermomechanical characterization of these TIMs was performed. It was revealed that the thermal and mechanical properties of the nanocomposite TIMs depend strongly on the interaction strength, which the selected ligand made with silver crystal.

In summary, the recently developed metal-inorganic-organic nanocomposite TIMs have shown to be reliable and compliant, which makes them promising candidates to be the next generation TIMs. And there is still a big potential for further improvement of these nanocomposite TIMs. Completion and commercialization of this product will have a high impact on the electronics that require a TIM for heat flow from a device to a heat sink, and semiconductor chip packaging industry will significantly benefit from this product as well.

Based on the conclusions of this work, future work can be summarized as follows:

(i) To further enhance the cooling performance of the nanocomposite TIMs, experiments on adhesion force will be conducted in order to find a compatible polymer adhesive to directly attach the developed nanocomposite TIMs to heat sink surfaces.

(ii) Thermal conductivity tests with longer heating-cooling cycles (>1000 cycles) to estimate the lifetime of our product.

(iii) Silver also has a great potential to fabricate nanocomposite having better properties than those with copper, due to its better compliance higher thermal conductivity. Discovery of new ligands to complex with silver will continue.

(iv) Preliminary experimental data have been obtained from Indium- and Gallium-based nanocomposite TIMs fabricated via electrodeposition and other techniques. We aim to obtain thermal and mechanical characterization results of these TIMs in a short term.

(v) The building blocks of the produced nanocomposite TIMs involve three main components: matrix, filler and organic ligand. While the matrix sources and the organic ligands were modified, the filler type has never been changed. Despite having great thermal properties and chemical stability, BNNS are hard/ceramic compounds. At nanoscale, they are assumed to be providing the high thermal conductivity of the TIMs. However, as mentioned in the previous sections, the governing factor of thermal transport in the TIMs is assumed to be the transport of electrons. For this purpose, replacing the BNNS with polymer beads as linking agents in metal matrices may bring a great advantage in terms of developing mechanically more compliant TIMs without significant loss of thermal properties.

REFERENCES

1. Sarvar, F., Whalley, D. C. & Conway, P. P. Thermal interface materials - a review of the state of the. in *Electronics Systemintegration Technology Conference, 1st* 1292–1302 (2006).
2. Antec's Formula 7 nano diamond thermal compound (2016). Available at: http://store.antec.com/thermal-paste/formula-7.html.
3. Arctic Silver® 5 High-density polysynthetic silver thermal compound (2016). Available at: http://www.arcticsilver.com/as5.htm.
4. Dolbear, T. P., MacKay, C. A. & Nelson, R. D. Liquid metal paste for thermal and electrical connections. **31,** US 5,056,706 (1991).
5. Kang, S. K., Purushothaman, S. & Simonyi, E. E. Thermally conducting materials and applications for microelectronic packaging. US 6,114,413 (2000).
6. Booth, R. B., Grube, G. W., Gruber, P. A., Khandros, I. Y. & Zingher, A. Y. Liquid metal matrix thermal paste. US 5,198,189 (1993).
7. Xu, Y., Leong, C.-K. & Chung, D. D. L. Carbon Nanotube Thermal Pastes for Improving Thermal Contacts. *Journal of Electronic Materials* **36,** 1181–1187 (2007).
8. Fabris, D. *et al.* Application of Carbon Nanotubes to Thermal Interface Materials. *Journal of Electronic Packaging* **133,** 020902 (2011).
9. Shinozaki, K., Anzai, K., Takano, T. & Tsuge, A. Aluminum nitride-based sintered body of high thermal conductivity. US 4,766,097 A (1988).

10. Nguyen, M. N. & Grundy, J. D. Compliant and crosslinkable thermal interface materials. US 5,989,459 (1999).

11. Wang, W., Yang, X., Fang, Y., Ding, J. & Yan, J. Enhanced thermal conductivity and thermal performance of form-stable composite phase change materials by using β-Aluminum nitride. *Applied Energy* **86,** 1196–1200 (2009).

12. Huang, H., Wu, Y., Liu, C.-H. & Fan, S.-S. Method for making a thermal interface material. **2,** US 7,393,428 B2 (2008).

13. Yu, H. *et al.* Thermal and Insulating Properties of Epoxy/Aluminum Nitride Composites Used for Thermal Interface Material. *Journal of Applied Polymer Science* **124,** 669–677 (2012).

14. Matayabas, J. C. & Koning, P. A. Phase change thermal interface materials including polyester resin. **2,** US 7,408,787 B2 (2008).

15. Bhagwagar, D. E. Thermal interface materials and methods for their preparation and use. **2,** US 6,791,839 B2 (2004).

16. Davison, P. A. & Koning, P. A. Component packaging apparatus, systems, and methods. **1,** US 0,116,387 A1 (2005).

17. Bergin, J. M. Thermal interface material having a zone-coated release linear. **1,** US 6,644,395 B1 (2003).

18. Xu, J. & Fisher, T. S. Enhancement of thermal interface materials with carbon nanotube arrays. *International Journal of Heat and Mass Transfer* **49,** 1658–1666 (2006).

19. Marconnet, A. A., Yamamoto, N., Panzer, M. A., Wardle, B. L. & Goodson, K. E.

Thermal Conduction in Aligned Carbon Nanotube-Polymer Nanocomposites with High Packing Density. *ACS Nano* **5,** 4818–4825 (2011).

20. Gojny, F. H. *et al.* Evaluation and identification of electrical and thermal conduction mechanisms in carbon nanotube/epoxy composites. *Polymer* **47,** 2036–2045 (2006).

21. Yu, A., Ramesh, P., Itkis, M. E., Bekyarova, E. & Haddon, R. C. Graphite Nanoplatelet - Epoxy Composite Thermal Interface Materials. *The Journal of Physical Chemistry C* **111,** 7565–7569 (2007).

22. Shahil, K. M. F. & Balandin, A. A. Graphene-multilayer graphene nanocomposites as highly efficient thermal interface materials. *Nano Letters* **12,** 861–867 (2012).

23. Plumbridge, W. J. Solders in electronics. *Journal of Materials Science* **31,** 2501–2514 (1996).

24. Kariya, Y. & Otsuka, M. Mechanical Fatigue Characteristics of Sn-3. 5Ag-X (X = Bi , Cu , Zn and In) Solder Alloys. *Journal of Electronic Materials* **27,** 1229–1235 (1998).

25. Felton, L. E., Raeder, C. H. & Knorr, D. B. The properties of tin-bismuth alloy solders. *Journal of the Minerals, Metals and Materials Society* **45,** 28–32 (1993).

26. Suraski, D. & Seelig, K. The current status of lead-free solder alloys. *IEEE Transactions on Electronics Packaging Manufacturing* **24,** 244–248 (2001).

27. Harrison, M. R., Vincent, J. H. & Steen, H. A. H. Lead-free reflow soldering for electronics assembly. *Soldering & Surface Mount Technology* **13,** 21–38 (2001).

28. Macris, C. G., Sanderson, T. R., Ebel, R. G. & Leyerle, C. B. Performance, Reliability, and Approaches Using a Low Melt Alloy as a Thermal Interface Material. in *Proceedings of IMAPS* (2004).

29. Tahmaspur, M. & Berhe, M. K. Thermal and Thermo Mechanical Phenomena in Electronic Systems. in *ITHERM*, 737 (2002).

30. Roy, C. K. *et al.* Performance of low melt alloys as thermal interface materials. in *Thermal Measurement, Modeling & Management Symposium (SEMI-THERM), 31st* 235–239 (IEEE, 2015).

31. Gwinn, J. . & Webb, R. . Performance and testing of thermal interface materials. *Microelectronics Journal* **34,** 215–222 (2003).

32. Zan, R., Bangert, U., Ramasse, Q. & Novoselov, K. S. Metal−Graphene Interaction Studied via Atomic Resolution Scanning Transmission Electron Microscopy. *Nano Letters* **11,** 1087–1092 (2011).

33. Zan, R., Bangert, U., Ramasse, Q. & Novoselov, K. S. Interaction of Metals with Suspended Graphene Observed by Transmission Electron Microscopy. *The Journal of Physical Chemistry Letters* **3,** 953–958 (2012).

34. Pakdel, A., Bando, Y. & Golberg, D. Nano boron nitride flatland. *Chemical Society Reviews* **43,** 934–959 (2014).

35. Zeng, H. *et al.* White Graphenes: Boron Nitride Nanoribbons via Boron Nitride Nanotube Unwrapping. *Nano Letters* **10,** 5049–5055 (2010).

36. Wang, C. *et al.* Superior thermal conductivity in suspended bilayer hexagonal boron nitride. *Scientific Reports* **6,** 25334 (2016).

37. Yu, J. *et al.* Interfacial modification of boron nitride nanoplatelets for epoxy composites with improved thermal properties. *Polymer* **53,** 471–480 (2012).

38. Xue, Y., Li, X., Li, H. & Zhang, W. Quantifying thiol–gold interactions towards the efficient strength control. *Nature Communications* **5,** 4348 (2014).

39. Laibinis, P. E. & Whitesides, G. M. Self-assembled monolayers of n-alkanethiolates on copper are barrier films that protect the metal against oxidation by air. *Journal of the American Chemical Society* **114,** 9022–9028 (1992).

40. Kanani, N. *Electroplating: basic principles, processes and practice*. (Elsevier, 2004).

41. Paunovic, M., Schlesinger, M. & Synder, D. D. *Modern Electroplating*. **55,** (John Wiley & Sons Inc., 2011).

42. Bard, A. J. & Faulkner, L. R. *Electrochemical Methods*. (Wiley, 1980).

43. Ibl, N. Some theoretical aspects of pulse electrolysis. *Surface Technology* **10,** (1980).

44. Pesco, A. M. & Cheh., H. Y. in *Modern Aspects of Electrochemistry* 251–293 (Springer US, 1989).

45. Paunovic, M. & Schlesinger, M. *Fundamentals of Electrochemical Deposition*. (Wiley, 2006).

46. Lorenz, W. No Title. *Zeitschrift für Physikalische Chemie* **202,** (1953).

47. Mehl, W. & Bockris, J. Mechanism of electrolytic silver deposition and dissolution. *The Journal of Chemical Physics* **27,** 818–819 (1957).

48. Budevski, E., Staikov, G. & Lorenz, W. J. *Electrochemical Phase Formation and*

Growth. (VCH Publishers, 1996).

49. Ghosh, S. *et al.* Extremely high thermal conductivity of graphene: Prospects for thermal management applications in nanoelectronic circuits. *Applied Physics Letters* **92,** 151911 (2008).

50. Zhang, Y., Dembla, A. & Bakir, M. S. Silicon micropin-fin heat sink with integrated TSVs for 3-D ICs: tradeoff analysis and experimental testing. *IEEE Transactions on Components, Packaging and Manufacturing Technology* **3,** 1842–1850 (2013).

51. Swartz, E. T. & Pohl, R. O. Thermal boundary resistance. *Reviews of Modern Physics* **61,** 605 (1989).

52. Pernot, G. *et al.* Precise control of thermal conductivity at the nanoscale through individual phonon-scattering barriers. *Nature Materials* **9,** 491–495 (2010).

53. Prasher, R. Thermal Interface Materials: Historical Perspective, Status, and Future Directions. *Proceedings of the IEEE* **94,** 1571–1586 (2006).

54. Yu, A. *et al.* Enhanced Thermal Conductivity in a Hybrid Graphite Nanoplatelet - Carbon Nanotube Filler for Epoxy Composites. *Advanced Materials* **20,** 4740–4744 (2008).

55. Wang, X. *et al.* In situ polymerization of graphene nanosheets and polyurethane with enhanced mechanical and thermal properties. *Journal of Materials Chemistry* **21,** 4222–4227 (2011).

56. Stankovich, S. *et al.* Graphene-based composite materials. *Nature* **442,** 282–286 (2006).

57. Biercuk, M. J. *et al.* Carbon nanotube composites for thermal management. *Applied Physics Letters* **80,** 2767–2769 (2002).

58. Jiang, H., Moon, K., Li, Y. & Wong, C. P. Surface functionalized silver nanoparticles for ultrahigh conductive polymer composites. *Chemistry of Materials* **18,** 2969–2973 (2006).

59. Yu, H., Li, L. & Zhang, Y. Silver nanoparticle-based thermal interface materials with ultra-low thermal resistance for power electronics applications. *Scripta Materialia* **66,** 931–934 (2012).

60. Wang, S., Cheng, Y., Wang, R., Sun, J. & Gao, L. Highly thermal conductive copper nanowire composites with ultralow loading: Toward applications as thermal interface materials. *ACS Applied Materials & Interfaces* **6,** 6481–6486 (2014).

61. Warzoha, R. J., Zhang, D., Feng, G. & Fleischer, A. S. Engineering interfaces in carbon nanostructured mats for the creation of energy efficient thermal interface materials. *Carbon* **61,** 441–457 (2013).

62. Chen, H. *et al.* Architecting three-dimensional networks in carbon nanotube buckypapers for thermal interface materials. *The Journal of Physical Chemistry C* **116,** 3903–3909 (2012).

63. Chung, D. D. L. Thermal Interface Materials. *Journal of Materials Engineering and Performance* **10,** 56–59 (2001).

64. White, G. K. Thermal expansion of reference materials: copper, silica and silicon. *Journal of Physics D: Applied Physics* **6,** 2070 (1973).

65. Bar-Cohen, A., Matin, K. & Narumanchi, S. Nanothermal Interface Materials: Technology Review and Recent Results. *Journal of Electronic Packaging* **137,** 040803 (2015).

66. Balandin, A. A. Thermal properties of graphene and nanostructured carbon materials. *Nature Materials* **10,** 569–581 (2011).

67. Yan, Z., Liu, G., Khan, J. M. & Balandin, A. a. Graphene quilts for thermal management of high-power GaN transistors. *Nature Communications* **3,** 827 (2012).

68. Leong, C. K., Aoyagi, Y. & Chung, D. D. L. Carbon black pastes as coatings for improving thermal gap-filling materials. *Carbon* **44,** 435–440 (2006).

69. Zhi, C., Bando, Y., Tang, C. & Golberg, D. Boron nitride nanotubes. *Materials Science and Engineering R: Reports* **70,** 92–111 (2010).

70. Lin, Y. & Connell, J. W. Advances in 2D boron nitride nanostructures: nanosheets, nanoribbons, nanomeshes, and hybrids with graphene. *Nanoscale* **4,** 6908 (2012).

71. Lindsay, L. & Broido, D. A. Enhanced thermal conductivity and isotope effect in single-layer hexagonal boron nitride. *Physical Review B* **84,** 155421 (2011).

72. Pham, T. *et al.* Nanoscale structure and superhydrophobicity of sp2-bonded boron nitride aerogels. *Nanoscale* **7,** 10449–10458 (2015).

73. Losego, M. D., Grady, M. E., Sottos, N. R., Cahill, D. G. & Braun, P. V. Effects of chemical bonding on heat transport across interfaces. *Nature Materials* **11,** 502–506 (2012).

74. O'Brien, P. J. *et al.* Bonding-induced thermal conductance enhancement at inorganic heterointerfaces using nanomolecular monolayers. *Nature Materials* **12,** 118–22 (2013).

75. Phelan, P. E. & Niemann, R. C. Effective Thermal Conductivity of a Thin, Randomly Oriented Composite Material. *Journal of Heat Transfer* **120,** 971–976 (1998).

76. Jo, I. *et al.* Thermal conductivity and phonon transport in suspended few-layer hexagonal boron nitride. *Nano Letters* **13,** 550–554 (2013).

77. Min, Y., Akbulut, M., Kristiansen, K., Golan, Y. & Israelachvili, J. The role of interparticle and external forces in nanoparticle assembly. *Nature Materials* **7,** 527–538 (2008).

78. Halpin, J. C. & Kardos, J. L. The Halpin-Tsai equations: A review. *Polymer Engineering and Science* **16,** 344–352 (1976).

79. Rafiee, M. A. *et al.* Enhanced mechanical properties of nanocomposites at low graphene content. *ACS Nano* **3,** 3884–3890 (2009).

80. Li, Y., Jia, W. Z., Song, Y. Y. & Xia, X. H. Superhydrophobicity of 3D porous copper films prepared using the hydrogen bubble dynamic template. *Chemistry of Materials* **19,** 5758–5764 (2007).

81. Fabricius, G. & Sundholm, G. The effect of additives on the electrodeposition of copper. *Transactions of Institute of Metal Finishing* **83,** 194–198 (2005).

82. Mammeri, F., Le Eric, B., Rozes, L. & Sanchez, C. Mechanical properties of hybrid organic-inorganic materials. *Journal of Materials Chemistry* **15,** 3787–

3811 (2005).

83. Li, C., Bando, Y., Zhi, C., Huang, Y. & Golberg, D. Thickness-dependent bending modulus of hexagonal boron nitride nanosheets. *Nanotechnology* **20,** 385707 (2009).

84. Kudin, K. N., Scuseria, G. E. & Yakobson, B. I. C2F, BN, and C nanoshell elasticity from ab initio computations. *Physical Review B* **64,** 235406 (2001).

85. Feng, X., King, C., Devoto, D., Mihalic, M. & Narumanchi, S. Investigation of thermal interface materials using phase-sensitive transient thermoreflectance technique. in *Thermal and Thermomechanical Phenomena in Electronic Systems (ITherm)* 1296–1307 (2014). doi:10.1109/ITHERM.2014.6892430

86. Incropera, F. P., Lavine, A. S. & DeWitt, D. P. *Fundamentals of Heat and Mass Transfer*. (John Wiley & Sons Inc., 2011).

87. Feng, X., King, C. & Narumanchi, S. General multilayer heat transfer model for optical-based thermal characterization techniques. *International Journal of Heat and Mass Transfer* **93,** 695–706 (2016).

88. Narumanchi, S., Mihalic, M., Kelly, K. & Eesley, G. Thermal interface materials for power electronics applications. in *Thermal and Thermomechanical Phenomena in Electronic Systems (ITHERM),* 395–404 (2008).

89. Malen, J. A. *et al.* Optical Measurement of Thermal Conductivity Using Fiber Aligned Frequency Domain Thermoreflectance. *Journal of Heat Transfer* **133,** 081601 (2011).

90. Sainsbury, T. *et al.* Covalently Functionalized Hexagonal Boron Nitride

Nanosheets by Nitrene Addition. *Chemistry: A European Journal* **18,** 10808–10812 (2012).

91. Roy, C. K. *et al.* Application of Low Melt Alloys as Compliant Thermal Interface Materials: A Study of Performance and Degradation under Thermal Duress. *Electronics Cooling* 26–31 (2015).
92. Koch, G. H., Bronger, M. P. H., Thompson, N. G., Virmani, Y. P. & Payer, J. H. *Corrosion Costs and Preventive Strategies in the United States, Supplement to Materials Performance*. (2001).
93. Stupnisek-Lisac, E. & Cinotti, V. Atmospheric corrosion inhibitors for copper in the electronics industry. *Journal of Applied Electrochemistry* **29,** 117–122 (1999).
94. Krishnamurthy, A. *et al.* Superiority of Graphene over Polymer Coatings for Prevention of Microbially Induced Corrosion. *Scientific Reports* **5,** 1–12 (2015).
95. Pushpavanam, M., Raman, V. & Shenoi, B. A. Rhodium—Electrodeposition and applications. *Surface Technology* **12,** 351–360 (1981).
96. Gelling, V. J., Wiest, M. M., Tallman, D. E., Bierwagen, G. P. & Wallace, G. G. Electroactive-conducting polymers for corrosion control: 4. Studies of poly (3-octyl pyrrole) and poly (3-octadecyl pyrrole) on aluminum 2024-T3 alloy. *Progress in Organic Coatings* **43,** 149–157 (2001).
97. Tallman, D. E., Spinks, G., Dominis, A. & Wallace, G. G. Electroactive conducting polymers for corrosion control. *Journal of Solid State Electrochemistry* **6,** 73–84 (2002).
98. Lusk, A. T. & Jennings, K. Characterization of self-assembled monolayers formed

from sodium S-alkyl thiosulfates on copper. *Langmuir* **17,** 7830–7836 (2001).

99. Prasai, D., Tuberquia, J. C., Harl, R. R., Jennings, G. K. & Bolotin, K. I. Graphene : Corrosion-Inhibiting Coating. *ACS Nano* **6,** 1102–1108 (2012).

100. Luechinger, N. A., Athanassiou, E. K. & Stark, W. J. Graphene-stabilized copper nanoparticles as an air-stable substitute for silver and gold in low-cost ink-jet printable electronics. *Nanotechnology* **19,** 445201 (2008).

101. Kirkland, N. T., Schiller, T., Medhekar, N. & Birbilis, N. Exploring graphene as a corrosion protection barrier. *Corrosion Science* **56,** 1–4 (2012).

102. Krishnamurthy, A. *et al.* Passivation of microbial corrosion using a graphene coating. *Carbon* **56,** 45–49 (2013).

103. Chang, C.-H. *et al.* Novel anticorrosion coatings prepared from polyaniline/graphene composites. *Carbon* **50,** 5044–5051 (2012).

104. Zhou, F., Li, Z., Shenoy, G. J., Li, L. & Liu, H. Enhanced Room-Temperature Corrosion of Copper in the Presence of Graphene. *ACS Nano* **7,** 6939–6947 (2013).

105. Sun, W. *et al.* Inhibiting the Corrosion-Promotion Activity of Graphene. *Chemistry of Materials* **27,** 2367–2373 (2015).

106. Sun, W., Wang, L., Wu, T., Pan, Y. & Liu, G. Communication — Multi-Layer Boron Nitride Nanosheets as Corrosion-Protective Coating Fillers. *Journal of the Electrochemical Society* **163,** 16–18 (2016).

107. Liu, Z. *et al.* Ultrathin high-temperature oxidation-resistant coatings of hexagonal boron nitride. *Nature Communications* **4,** 2541 (2013).

108. Li, L. H., Xing, T., Chen, Y. & Jones, R. Boron nitride nanosheets for metal protection. *Advanced Materials Interfaces* **1,** (2014).

109. Yi, M., Shen, Z., Zhao, X., Liang, S. & Liu, L. Boron nitride nanosheets as oxygen-atom corrosion protective coatings. *Applied Physics Letters* **104,** 143101 (2014).

110. Lopez, B. G. *et al.* Corrosion of metals at indoor conditions in the electronics manufacturing industry. *Anti-Corrosion Methods and Materials* **54,** 354–359 (2007).

111. Schlesinger, M. *Electroless and electrodeposition of silver.* (John Wiley & Sons, Inc., 2010).

112. Hopkins, P. E. *et al.* Manipulating thermal conductance at metal-graphene contacts via chemical functionalization. *Nano Letters* **12,** 590–595 (2012).

113. Ong, W.-L., Rupich, S. M., Talapin, D. V, McGaughey, A. J. H. & Malen, J. A. Surface chemistry mediates thermal transport in three-dimensional nanocrystal arrays. *Nature Materials* **12,** 410–5 (2013).

114. Wang, Y., Yang, C., Pei, Q. X. & Zhang, Y. Some Aspects of Thermal Transport across the Interface between Graphene and Epoxy in Nanocomposites. *ACS Applied Materials and Interfaces* **8,** 8272–8279 (2016).

115. Ouyang Tao *et al.* Thermal transport in hexagonal boron nitride nanoribbons. *Nanotechnology* **21,** 245701 (2010).

116. Ordonez-Miranda, J., Alvarado-Gil, J. J. & Yang, R. The effect of the electron-phonon coupling on the effective thermal conductivity of metal-nonmetal

multilayers. *Journal of Applied Physics* **109,** 094310 (2011).

117. Bishop, K. J. M., Wilmer, C. E., Soh, S. & Grzybowski, B. A. Nanoscale Forces and Their Uses in Self-Assembly. *Small* **5,** 1600–1630 (2009).

118. Yegin, C., Zhang, M., Talari, J. V. & Akbulut, M. Novel hydraulic fracturing fluids with improved proppant carrying capacity and pH-adjustable proppant deposition behavior. *Journal of Petroleum Science and Engineering* **145,** 600-608 (2016).

119. Arthur, J. D., Bohm, B. & Layne, M. *Hydraulic Fracturing Considerations for Natural Gas Wells of the Marcellus Shale*. (2009).

120. Gaillard, N., Thomas, A. & Favero, C. Novel Associative Acrylamide-based Polymers for Proppant Transport in Hydraulic Fracturing Fluids. in *SPE International Symposium on Oilfield Chemistry* (2013).

121. Al-Muntasheri, G. A. A Critical Review of Hydraulic-Fracturing Fluids for Moderate- to Ultralow- Permeability Formations Over the Last Decade. in *SPE Production and Operations Conference and Exhibition*, 243–260 (2014).

122. Jung, H. B. *et al.* Stimuli-responsive/rheoreversible hydraulic fracturing fluids as a greener alternative to support geothermal and fossil energy production. *Green Chemistry* **17,** 2799–2812 (2015).

123. Samuel, M. *et al.* Viscoelastic Surfactant Fracturing Fluids: Applications in Low Permeability Reservoirs. in *SPE Rocky Mountain Regional/Low-Permeability Reservoirs Symposium and Exhibition* (2000).

124. Warplnskl, N. R. & Laboratories, S. N. Hydraulic Fracturing in Tight , Fissured

Media. *Journal of Petroleum Technology* **43,** 146–152 (1991).

125. Al-Muntasheri, G. A. A Critical Review of Hydraulic Fracturing Fluids over the Last Decade. *SPE Western North American and Rocky Mountain Joint Regional Meeting*, 169552 (2014).

126. Montgomery, C. in *Effective and Sustainable Hydraulic Fracturing*, 3–25 (2013).

127. Wang, Q., Dan, Y. & Wang, X. G. A New Polymer Flooding Agent Prepared Through Intermacromolecular Complexation. *Journal of Macromolecular Science, Part A* **34,** 1155–1169 (1997).

128. Zhang, S., She, Y. & Gu, Y. Evaluation of polymers as direct thickeners for CO2 enhanced oil recovery. *Journal of Chemical & Engineering Data* **56,** 1069–1079 (2011).

129. Crews, J. B. & Huang, T. New Remediation Technology Enables Removal of Residual Polymer in Hydraulic Fractures. in *SPE Annual Technical Conference and Exhibition* (2010).

130. Mahto, V. & Sharma, V. P. Rheological study of a water based oil well drilling fluid. *Journal of Petroleum Science and Engineering* **45,** 123–128 (2004).

131. Li, M.-C., Wu, Q., Song, K., Qing, Y. & Wu, Y. Cellulose nanoparticles as modifiers for rheology and fluid loss in bentonite water-based fluids. *ACS Applied Materials & Interfaces* **7,** 5006–5016 (2015).

132. Al-Muntasheri, G. A., Nasr-El-Din, H. A. & Hussein, I. A. A rheological investigation of a high temperature organic gel used for water shut-off treatments. *Journal of Petroleum Science and Engineering* **59,** 73–83 (2007).

133. Zhao, Y., Zhou, J., Xu, X., Liu, W. & Zhang, J. Synthesis and characterization of a series of modified polyacrylamide. *Colloid and Polymer Science* **287,** 237–241 (2009).

134. Al Hashmi, A. R. *et al.* Rheology and mechanical degradation of high-molecular-weight partially hydrolyzed polyacrylamide during flow through capillaries. *Journal of Petroleum Science and Engineering* **105,** 100–106 (2013).

135. Sinclair, A. R., Terry, W. M. & Kiel, O. M. Polymer emulsion fracturing. *Journal of Petroleum Technology* **26,** 731–738 (1974).

136. Cramer, D. D., Woo, G. T. & Dawson, J. C. Development and Implementation of a Low-Polymer-Concentration Crosslinked Fracturing Fluid for Low-Temperature Applications. in *SPE Eastern Regional Meeting* (2004).

137. Fu, D.-K., Fedorov, A., Prudnikov, A., Mauth, K. & Lungwitz, B. New Polymer Fluid for Hydraulic Fracturing in Russia. in *SPE Production and Operations Conference and Exhibition* (2010).

138. Guo, J., Lu, H., Zhou, B., Xia, A. & Li, Z. A New Fracturing Fluid of Low Concentration. in *IADC/SPE Asia Pacific Drilling Technology Conference and Exhibition* (2012).

139. Siggel, L. *et al.* TPM's : A New Class of Viscoelastic Solutions for Enhanced Oil Recovery. in *SPE EOR Conference at Oil and Gas West Asia* (2014).

140. Wever, D. A. Z., Picchioni, F. & Broekhuis, A. A. Polymers for enhanced oil recovery: A paradigm for structure–property relationship in aqueous solution. *Progress in Polymer Science* **36,** 1558–1628 (2011).

141. Gall, B. L., Sattler, A. R., Maloney, D. R. & Raible, C. J. Permeability Damage to Natural Fractures Caused by Fracturing Fluid Polymers. in *SPE Rocky Mountain Regional Meeting*, 11–13 (1988).

142. Samuel, M. M. *et al.* Polymer-Free Fluid for Fracturing Applications. *SPE Drill. & Completion* **14,** 240–246 (1999).

143. Ahmadi, M. & Shadizadeh, S. Implementation of a high-performance surfactant for enhanced oil recovery from carbonate reservoirs. *Journal of Petroleum Science and Engineering* **110,** 66–73 (2013).

144. Ahmadi, M. A., Galedarzadeh, M. & Shadizadeh, S. R. Wettability Alteration in Carbonate Rocks by Implementing New Derived Natural Surfactant: Enhanced Oil Recovery Applications. *Transport in Porous Media* **106,** 645–667 (2014).

145. Nourani, M., Tichelkamp, T., Gaweł, B. & Øye, G. Method for Determining the Amount of Crude Oil Desorbed from Silica and Aluminosilica Surfaces upon Exposure to Combined Low-Salinity Water and Surfactant Solutions. *Energy & Fuels* **28,** 1884–1889 (2014).

146. Sinz, D. K. N., Hanyak, M. & Darhuber, A. a. Self-Induced Surfactant Transport along Discontinuous Liquid–Liquid Interfaces. *The Journal of Physical Chemistry Letters* **4,** 1039–1043 (2013).

147. Barati, R. & Liang, J.-T. A review of fracturing fluid systems used for hydraulic fracturing of oil and gas wells. *Journal of Applied Polymer Science* **131,** 40735 (2014).

148. Chen, Y., Pope, T. L. & Lee, J. C. Novel CO2-Emulsified Viscoelastic Surfactant

Fracturing Fluid System. in *SPE European Formation Damage Conference* (2005).

149. Tang, J., Quinlan, P. & Tam, K. C. Stimuli responsive Pickering emulsions: Recent advances and potential applications. *Soft Matter* **11,** 3512–3529 (2015).
150. Kefi, S. *et al.* Expanding Applications for Viscoelastic Surfactants. *Oilfield Review* **16,** 10–23 (2004).
151. Sun, X., Liang, X., Wang, S. & Lu, Y. Experimental study on the rheology of CO2 viscoelastic surfactant foam fracturing fluid. *Journal of Petroleum Science and Engineering* **119,** 104–111 (2014).
152. Chu, Z., Dreiss, C. a & Feng, Y. Smart wormlike micelles. *Chemical Society Reviews* **42,** 7174–7203 (2013).
153. Rogers, S. a., Calabrese, M. a. & Wagner, N. J. Rheology of branched wormlike micelles. *Current Opinion in Colloid & Interface Science* **19,** 530–535 (2014).
154. Su, X., Cunningham, M. F. & Jessop, P. G. Switchable viscosity triggered by CO2 using smart worm-like micelles. *Chemical Communications* **49,** 2655–2657 (2013).
155. Yang, J. *et al.* Instant gel formation of viscoelastic surfactant fracturing fluids by diluting through lamellar liquid crystal. *Journal of Petroleum Science and Engineering* **125,** 90–94 (2015).
156. Zhang, Y. *et al.* Smart wormlike micelles switched by CO2 and air. *Soft Matter* **9,** 6217–6221 (2013).
157. Luo, X., Wang, S., Wang, Z., Jing, Z. & Lv, M. Experimental research on

rheological properties and proppant transport performance of GRF–CO_2 fracturing fluid. *Journal of Petroleum Science and Engineering* **120,** 154–162 (2014).

158. Willberg, D. M. *et al.* Determination of the Effect of Formation Water on fracture Fluid Cleanup Through Field Testing in the East Texas Cotton Valley. in *SPE Annual Technical Conference and Exhibition* (1997).

159. Neurath, G. B., Dünger, M., Pein, F. G., Ambrosius, D. & Schreiber, O. Primary and secondary amines in the human environment. *Food and Cosmetics Toxicology* **15,** 275–282 (1977).

160. Lelais, G. & Seebach, D. β2-amino acids—syntheses, occurrence in natural products, and components of β-peptides1,2. *Peptide Science* **76,** 206–243 (2004).

161. De Visscher, J., Soenen, H., Vanelstraete, A. & Redelius, P. A Comparison of the zero shear viscosity from oscillation tests and repeated creep test. in *Proceedings of the 3rd Eurasphalt and Eurobitume Congress*, 1501–1513 (2004).

162. Chen, I., Yegin, C., Zhang, M., Akbulut, M. & Texas, A. Use of pH-Responsive Amphiphilic Systems as Displacement Fluids in Enhanced Oil Recovery. *SPE Journal* **19,** 1035–1046 (2014).

163. De Gennes, P. G. Dynamics of Entangled Polymer Solutions. I. The Rouse Model. *Macromolecules* **9,** 587–593 (1976).

164. Candau, S. J., Hirsch, E., Zana, R. & Delsanti, M. Rheological Properties of Semidilute and Concentrated Aqueous Solutions of Cetyltrimethylammonium Bromide in the Presence of Potassium Bromide. *Langmuir* **5,** 1225–1229 (1989).

165. Graue, A., Ramsdal, J. & Fernø, M. A. Mobilization of Immobile Water: Connate-Water Mobility During Waterfloods in Heterogeneous Reservoirs. *Society of Petroleum Engineers* **20,** 88–98 (2014).

166. Fu, Y., van Berk, W. & Schulz, H.-M. Hydrogeochemical modelling of fluid–rock interactions triggered by seawater injection into oil reservoirs: Case study Miller field (UK North Sea). *Applied Geochemistry* **27,** 1266–1277 (2012).

167. Yousef, A. A., Al-saleh, S., Al-kaabi, A. & Al-Jawfi, M. Laboratory Investigation of the Impact of Injection-Water Salinity and Ionic Content on Oil Recovery From Carbonate Reservoirs. *SPE Reservior Evaluation & Engineering* **14,** 578–593 (2012).

168. Millero, F. J., Feistel, R., Wright, D. G. & Mcdougall, T. J. The composition of Standard Seawater and the definition of the Reference-Composition Salinity Scale. *Deep-Sea Research I* **55,** 50–72 (2008).

169. Arrhenius, S. The Viscosity of Solutions. *Biochemical Journal* **11,** 112 (1917).

170. Armstrong, K., Card, R. & Navarrete, R. Advanced fracturing fluids improve well economics. *Oilfield Review* **7,** 34–51 (1995).

171. Wang, W. *et al.* Hydraulic Fracturing in Low Temperature Horizontal Wells. in *SPE Oil and Gas India Conference and Exhibition* 127266 (Society of Petroleum Engineers, 2010).

172. Zhao, H., Nasr-El-Din, H. & Al-Bagoury, M. A New Fracturing Fluid for HP/HT Applications. in *SPE European Formation Damage Conference* (2015).

173. Kruijf, A. S. De, Roodhart, L. P. & Davies, D. R. Relation between chemistry and

flow mechanics of borate-crosslinked fracturing fluids. *SPE Production & Facilities* **8,** 165–170 (1993).

174. Renaud, M., Mauret, E. & Chhabra, R. P. Power-Law Fluid Flow Over a Sphere: Average Shear Rate and Drag Coefficient. *The Canadian Journal of Chemical Engineering* **82,** 1066–1070 (2004).

175. Chen, S. & Rothstein, J. P. Flow of a wormlike micelle solution past a falling sphere. *Journal of Non-Newtonian Fluid Mechanics* **116,** 205–234 (2004).

176. Liberatore, M. W. *et al.* Microstructure and shear rheology of entangled wormlike micelles in solution. *Journal of Rheology* **53,** 441–458 (2009).

177. Malhotra, S. & Sharma, M. M. Settling of spherical particles in unbounded and confined surfactant-based shear thinning viscoelastic fluids: An experimental study. *Chemical Engineering Science* **84,** 646–655 (2012).

178. Mena, B., Manero, O. & Leal, L. The influence of rheological properties on the slow flow past spheres. *Journal of Non-Newtonian Fluid Mechanics* **26,** 247–275 (1987).

179. Wang, S. *et al.* A study of relation between suspension behavior and microstructure and viscoelastic property of guar gum fracturing fluid. *Journal of Petroleum Science and Engineering* **124,** 432–435 (2014).

180. Chen, I.-C. *et al.* Transport of Polymeric Nanoparticulate Drug Delivery Systems in the Proximity of Silica and Sand. *Environmental Science & Technology* **49,** 3575–3583 (2015).

181. Barbot, E., Vidic, N. S., Gregory, K. B. & Vidic, R. D. Spatial and temporal

correlation of water quality parameters of produced waters from devonian-age shale following hydraulic fracturing. *Environmental Science & Technology* **47,** 2562–2569 (2013).

182. Vengosh, A., Jackson, R. B., Warner, N., Darrah, T. H. & Kondash, A. A critical review of the risks to water resources from unconventional shale gas development and hydraulic fracturing in the United States. *Environmental Science & Technology* **48,** 8334–48 (2014).

183. Norman, L., Vitthal, S. & Terracina, J. New Breaker Technology for Fracturing High-Permeability Formations. in *SPE European Damage Symposium* (1995).

184. Vitorge, E., Szenknect, S., Martins, J. M. F. & Gaudet, J.-P. Size- and concentration-dependent deposition of fluorescent silica colloids in saturated sand columns: transport experiments and modeling. *Environmental Science. Processes & Impacts* **15,** 1590–1600 (2013).

185. Hamaker, H. The London—van der Waals attraction between spherical particles. *Physica* **4,** 1058–1072 (1937).

186. Prieve, D. C. & Ruckenstein, E. The surface potential of and double-layer interaction force between surfaces characterized by multiple ionizable groups. *Journal of Theoretical Biology* **56,** 205–228 (1976).

187. Yegin, C. *et al.* The effect of nanoparticle functionalization on lubrication performance of nanofluids dispersing silica nanoparticles in an ionic liquid. *Journal of Tribology* [In Print].

188. Huang, H. *et al.* Carbon quantum dot/CuS_x nanocomposites towards highly

efficient lubrication and metal wear repair. *Nanoscale* **7,** 11321–11327 (2015).

189. Spikes, H. Friction Modifier Additives. *Tribology Letters* **60,** 1–26 (2015).

190. Meng, Y., Su, F. & Chen, Y. Synthesis of nano-Cu/graphene oxide composites by supercritical CO2-assisted deposition as a novel material for reducing friction and wear. *Chemical Engineering Journal* **281,** 11–19 (2015).

191. Mu, L. *et al.* Self-Lubricating Polytetrafluoroethylene/Polyimide Blends Reinforced with Zinc Oxide Nanoparticles. *Journal of Nanomaterials* **2015,** 8 (2015).

192. Zhang, Z. J., Simionesie, D. & Schaschke, C. Graphite and Hybrid Nanomaterials as Lubricant Additives. *Lubricants* **2,** 44–65 (2014).

193. Ahmed, N. S. & Nassar, A. M. *Lubricating Oil Additives*. (INTECH Open Access Publisher, 2011).

194. Yadgarov, L. *et al.* Tribological studies of rhenium doped fullerene-like MoS_2 nanoparticles in boundary, mixed and elasto-hydrodynamic lubrication conditions. *Wear* **297,** 1103–1110 (2013).

195. Adhvaryu, A. & Erhan, S. Z. Epoxidized soybean oil as a potential source of high-temperature lubricants. *Industrial Crops and Products* **15,** 247–254 (2002).

196. Martins, R. *et al.* Friction coefficient in FZG gears lubricated with industrial gear oils: Biodegradable ester vs. mineral oil. *Tribology International* **39,** 512–521 (2006).

197. Gusain, R. & Khatri, O. P. Fatty acid ionic liquids as environmentally friendly lubricants for low friction and wear. *RSC Advances* **6,** 3462–3469 (2016).

198. Lathi, P. S. & Mattiasson, B. Green approach for the preparation of biodegradable lubricant base stock from epoxidized vegetable oil. *Applied Catalysis B: Environmental* **69,** 207–212 (2007).

199. Boyde, S. Green lubricants. Environmental benefits and impacts of lubrication. *Green Chemistry* **4,** 293–307 (2002).

200. Luna, F. M. T. *et al.* Assessment of biodegradability and oxidation stability of mineral, vegetable and synthetic oil samples. *Industrial Crops and Products* **33,** 579–583 (2011).

201. Norrby, T. Environmentally adapted lubricants – where are the opportunities? *Industrial Lubrication and Tribology* **55,** 268–274 (2003).

202. Kheireddin, B., Lu, W., Chen, I.-C. & Akbulut, M. Inorganic nanoparticle-based ionic liquid lubricants. *Wear* **303,** 185–190 (2013).

203. Plechkova, N. V & Seddon, K. R. Applications of ionic liquids in the chemical industry. *Chemical Society Reviews* **37,** 123–150 (2008).

204. Castner, E. W., Margulis, C. J., Maroncelli, M. & Wishart, J. F. Ionic liquids: structure and photochemical reactions. *Annual Review of Physical Chemistry* **62,** 85–105 (2011).

205. Song, Z. *et al.* Green Ionic Liquid Lubricants Prepared from Anti-Inflammatory Drug. *Tribology Letters* **60,** 38 (2015).

206. Payne, Samantha M. Kerton, F. M. Solubility of bio-sourced feedstocks in 'green' solvents. *Green Chemistry* **12,** 1648–1653 (2010).

207. Kulacki, K. J. & Lamberti, G. A. Toxicity of imidazolium ionic liquids to

freshwater algae. *Green Chemistry* **10,** 104–110 (2008).

208. Sheldon, R. A. Green solvents for sustainable organic synthesis: state of the art. *Green Chemistry* **7,** 267–278 (2005).

209. Arora, H. & Cann, P. M. Lubricant film formation properties of alkyl imidazolium tetrafluoroborate and hexafluorophosphate ionic liquids. in *Tribology International* **43,** 1908–1916 (2010).

210. Yao, M., Fan, M., Liang, Y., Zhou, F. & Xia, Y. Imidazolium hexafluorophosphate ionic liquids as high temperature lubricants for steel-steel contacts. *Wear* **268,** 67–71 (2010).

211. Otero, I. *et al.* Ionic liquids based on phosphonium cations As neat lubricants or lubricant additives for a steel/steel contact. *ACS Applied Materials and Interfaces* **6,** 13115–13128 (2014).

212. Pejaković, V., Tomastik, C., Dörr, N. & Kalin, M. Influence of concentration and anion alkyl chain length on tribological properties of imidazolium sulfate ionic liquids as additives to glycerol in steel–steel contact lubrication. *Tribology International* **97,** 234–243 (2016).

213. Li, H. *et al.* Addition of low concentrations of an ionic liquid to a base oil reduces friction over multiple length scales: a combined nano-and macrotribology investigation. *Physical Chemistry Chemical Physics* **18,** 6541–6547 (2016).

214. Song, Z., Liang, Y., Fan, M., Zhou, F. & Liu, W. Ionic liquids from amino acids: fully green fluid lubricants for various surface contacts. *RSC Advances* **4,** 19396–19402 (2014).

215. Cai, Z. *et al.* Comparison of the tribological behavior of steel–steel and Si 3 N 4–steel contacts in lubricants with ZDDP or ionic liquid. *Wear* **319,** 172–183 (2014).

216. Wu, J. *et al.* High load capacity with ionic liquid-lubricated tribological system. *Tribology International* **94,** 315–322 (2016).

217. Tiago, G. *et al.* Novel ionic liquids for interfacial and tribological applications. *Colloids and Surfaces A: Physicochemical and Engineering Aspects* **472,** 1–8 (2015).

218. Watanabe, S., Nakano, M., Miyake, K., Tsuboi, R. & Sasaki, S. Effect of Molecular Orientation Angle of Imidazolium Ring on Frictional Properties of Imidazolium-Based Ionic Liquid. *Langmuir* **30,** 8078–8084 (2014).

219. Han, Y., Qiao, D., Zhang, L. & Feng, D. Study of tribological performance and mechanism of phosphonate ionic liquids for steel/aluminum contact. *Tribology International* **84,** 71–80 (2015).

220. Espinosa, T., Sanes, J., Jim??nez, A. E. & Berm??dez, M. D. Surface interactions, corrosion processes and lubricating performance of protic and aprotic ionic liquids with OFHC copper. *Applied Surface Science* **273,** 578–597 (2013).

221. Arcifa, A., Rossi, A., Espinosa-Marzal, R. M. & Spencer, N. D. Influence of environmental humidity on the wear and friction of a silica/silicon tribopair lubricated with a hydrophilic ionic liquid. *ACS Applied Materials & Interfaces* (2016).

222. Werzer, O., Cranston, E. D., Warr, G. G., Atkin, R. & Rutland, M. W. Ionic liquid nanotribology: mica–silica interactions in ethylammonium nitrate. *Physical*

Chemistry Chemical Physics **14,** 5147–5152 (2012).

223. Espinosa, T. *et al.* Ultra-Low Friction with a Protic Ionic Liquid Boundary Film at the Water-Lubricated Sapphire–Stainless Steel Interface. *Tribology Letters* **53,** 1–9 (2014).

224. Wang, H., Qiao, D., Zhang, S., Feng, D. & Lu, J. Tribological performance and lubrication mechanism of alkylimidazolium dialkyl phosphates ionic liquids as lubricants for Si_3N_4-Ti_3SiC_2 contacts. *Journal of Nanomaterials* **2014,** 6 (2014).

225. Somers, A. E. *et al.* Ionic liquids as antiwear additives in base oils: influence of structure on miscibility and antiwear performance for steel on aluminum. *ACS Applied Materials & Interfaces* **5,** 11544–11553 (2013).

226. Gusain, R. *et al.* Self-assembled thin film of imidazolium ionic liquid on a silicon surface: Low friction and remarkable wear-resistivity. *Applied Surface Science* **364,** 878–885 (2016).

227. Totolin, V., Minami, I., Gabler, C., Brenner, J. & Dörr, N. Lubrication mechanism of phosphonium phosphate ionic liquid additive in alkylborane–imidazole complexes. *Tribology Letters* **53,** 421–432 (2014).

228. Yu, B. *et al.* Oil-miscible and non-corrosive phosphonium-based ionic liquids as candidate lubricant additives. *Wear* **289,** 58–64 (2012).

229. Qu, J. *et al.* Synergistic Effects Between Phosphonium-Alkylphosphate Ionic Liquids and Zinc Dialkyldithiophosphate (ZDDP) as Lubricant Additives. *Advanced Materials* **27,** 4767–4774 (2015).

230. Shi, Y., Mu, L., Feng, X. & Lu, X. Friction and wear behavior of CF/PTFE

composites lubricated by choline chloride ionic liquids. *Tribology Letters* **49,** 413–420 (2013).

231. Mu, L. *et al.* Ionic Grease Lubricants: Protic [Triethanolamine][Oleic Acid] and Aprotic [Choline][Oleic Acid]. *ACS Applied Materials & Interfaces* **8,** 4977–4984 (2016).

232. Mahrova, M. *et al.* Pyridinium based dicationic ionic liquids as base lubricants or lubricant additives. *Tribology International* **82,** 245–254 (2015).

233. Taher, M. *et al.* Halogen-free pyrrolidinium bis (mandelato) borate ionic liquids: some physicochemical properties and lubrication performance as additives to polyethylene glycol. *RSC Advances* **4,** 30617–30623 (2014).

234. Yu, B., Liu, Z., Zhou, F., Liu, W. & Liang, Y. A novel lubricant additive based on carbon nanotubes for ionic liquids. *Materials Letters* **62,** 2967–2969 (2008).

235. Sanes, J., Carrión, F. J. & Bermúdez, M. D. Effect of the addition of room temperature ionic liquid and ZnO nanoparticles on the wear and scratch resistance of epoxy resin. *Wear* **268,** 1295–1302 (2010).

236. Yu, B. *et al.* Ionic liquid modified multi-walled carbon nanotubes as lubricant additive. *Tribology International* **81,** 38–42 (2015).

237. Pu, J. *et al.* Preparation and tribological study of functionalized graphene–IL nanocomposite ultrathin lubrication films on Si substrates. *The Journal of Physical Chemistry C* **115,** 13275–13284 (2011).

238. Khare, V. *et al.* Graphene–ionic liquid based hybrid nanomaterials as novel lubricant for low friction and wear. *ACS Applied Materials & Interfaces* **5,** 4063–

4075 (2013).

239. Fan, X., Wang, L. & Li, W. In Situ Fabrication of Low-Friction Sandwich Sheets Through Functionalized Graphene Crosslinked by Ionic Liquids. *Tribology Letters* **58,** 1–12 (2015).

240. Fan, X. & Wang, L. Ionic liquids gels with in situ modified multiwall carbon nanotubes towards high-performance lubricants. *Tribology International* **88,** 179–188 (2015).

241. Fan, X. & Wang, L. Highly Conductive Ionic Liquids toward High-Performance Space- Lubricating Greases. *ACS Applied Materials & Interfaces* **6,** 14660–14671 (2014).

242. Fan, X. *et al.* Study of the conductivity and tribological performance of ionic liquid and lithium greases. *Tribology Letters* **53,** 281–291 (2014).

243. Carrión, F. J., Sanes, J., Bermúdez, M.-D. & Arribas, A. New single-walled carbon nanotubes–ionic liquid lubricant. application to polycarbonate–stainless steel sliding contact. *Tribology Letters* **41,** 199–207 (2011).

244. Gusain, R. & Khatri, O. P. Ultrasound assisted shape regulation of CuO nanorods in ionic liquids and their use as energy efficient lubricant additives. *Journal of Materials Chemistry A* **1,** 5612–5619 (2013).

245. Peng, D.-X., Chen, C.-H., Kang, Y., Chang, Y.-P. & Chang, S.-Y. Size effects of SiO2 nanoparticles as oil additives on tribology of lubricant. *Industrial Lubrication and Tribology* **62,** 111–120 (2010).

246. Xie, H. M. *et al.* Effect of SiO2 nanoparticles as lubricating oil additives on the

cold-rolling of AZ31 magnesium alloy sheet. *Materials Research Innovations* **19,** 127–132 (2015).

247. Liu, G., Cai, M., Zhou, F. & Liu, W. Charged polymer brushes-grafted hollow silica nanoparticles as a novel promising material for simultaneous joint lubrication and treatment. *Journal of Physical Chemistry B* **118,** 4920–4931 (2014).

248. Rahman, I. A. *et al.* An optimized sol–gel synthesis of stable primary equivalent silica particles. *Colloids and Surfaces A: Physicochemical and Engineering Aspects* **294,** 102–110 (2007).

249. Marini, M., Pourabbas, B., Pilati, F. & Fabbri, P. Functionally modified core-shell silica nanoparticles by one-pot synthesis. *Colloids and Surfaces A: Physicochemical and Engineering Aspects* **317,** 473–481 (2008).

250. Bourlinos, A. B. *et al.* Surface-Functionalized Nanoparticles with Liquid-Like Behavior. *Advanced Materials* **17,** 234–237 (2005).

251. Akbulut, M., Belman, N., Golan, Y. & Israelachvili, J. Frictional Properties of Confined Nanorods. *Advanced Materials* **18,** 2589–2592 (2006).

252. Chen, Y. L., Xu, Z. & Israelachvili, J. Structure and interactions of surfactant-covered surfaces in nonaqueous (oil-surfactant-water) media. *Langmuir* **8,** 2966–2975 (1992).

253. Padgurskas, J., *et al.* Tribological properties of lubricant additives of Fe, Cu and Co nanoparticles. *Tribology International* **60,** 224–232 (2013).

254. Akbulut, M. Nanoparticle-based lubrication systems. *J Powder Metall Min* **1,**

e101 (2012).

255. Moshkovith, A. *et al.* Friction of fullerene-like WS2 nanoparticles: effect of agglomeration. *Tribology Letters* **24,** 225–228 (2006).

256. Rapoport, L., Fleischer, N. & Tenne, R. Fullerene-like WS_2 Nanoparticles: Superior Lubricants for Harsh Conditions. *Advanced Materials* **15,** 651–655 (2003).

257. Bartz, W. J. Solid lubricant additives—effect of concentration and other additives on anti-wear performance. *Wear* **17,** 421–432 (1971).

258. Verma, A., Jiang, W., Abu Safe, H. H., Brown, W. D. & Malshe, A. P. Tribological Behavior of Deagglomerated Active Inorganic Nanoparticles for Advanced Lubrication. *Tribology Transactions* **51,** 673–678 (2008).

259. Gulzar, M. *et al.* Tribological performance of nanoparticles as lubricating oil additives. *Journal of Nanoparticle Research* **18,** 223 (2016).

260. Song, X. *et al.* Synthesis of monodispersed $ZnAl_2O_4$ nanoparticles and their tribology properties as lubricant additives. *Materials Research Bulletin* **47,** 4305–4310 (2012).

261. Yang, Y., Singh, J. & Ruths, M. Friction of aromatic thiol monolayers on silver : SFA and AFM studies of adhesive and non-adhesive contacts. *RSC Advances* **4,** 18801–18810 (2014).

262. Ueno, K., Inaba, A., Kondoh, M. & Watanabe, M. Colloidal Stability of Bare and Polymer-Grafted Silica Nanoparticles in Ionic Liquids. *Langmuir* **24,** 5253–5259 (2008).

APPENDIX A

PH-RESPONSIVE SUPRAMOLECULAR ASSEMBLIES AS HYDRAULIC FRACTURING FLUIDS WITH ENHANCED AND ADJUSTABLE PROPPANT CARRYING CAPACITY*

A.1. Abstract

In hydraulic fracturing, the design of the fracturing fluids is a crucial step in optimizing the effectiveness of natural gas and oil recovery. Herein, we describe a supramolecular solution with highly adjustable, reversible viscosity behavior, enabling control over the mobility, settling, and deposition of proppants. The supramolecular solution was obtained by complexation of an amino amide and maleic acid in an aqueous solution. The rheological properties of the developed fracture fluid involving this supramolecular solution and proppant (silica sand) were characterized by frequency sweep, tixotropy tests and settling studies. It was found that for a 2 wt.%. solution, the zero frequency viscosity could be adjusted by a factor of 1600 by changing pH from 3.8 at to 8.3 in a reversible fashion. Settling studies revealed that the sedimentation velocity of sand particles decreased by five orders of magnitude from 2.3×10^{-3} m/s to 5.3×10^{-8} m/s upon an increase in pH from 4 to 8 in a reversible manner. Moreover, the supramolecular solution was found to maintain the rheological integrity even at NaCl

---

*Reprinted with permission from "Novel hydraulic fracturing fluids with improved proppant carrying capacity and pH-adjustable proppant deposition behavior." by Cengiz Yegin, Ming Zhang, Jyothsna Varsha Talari, and Mustafa Akbulut. *Journal of Petroleum Science and Engineering* 145 (2016): 600-608.[118] Copyright 2016 by Elsevier.

concentrations above those of seawater. The significant reduction in the rate of proppant sedimentation and enhancement in the sedimentation stability were ascribed to the increased viscosity and the intermolecular and interparticulate interactions between proppant and microscale networks and entanglements. In summary, supramolecular assembly of an amino amide and maleic acid has a potential to be effective fracturing fluids due to its highly pH adjustable viscosity and proppant carrying capacity, reliability at high salinities, and availability of its bio-based precursors in a sustainable manner.

A.2. Introduction

Technological advances in horizontal drilling and hydraulic fracturing have led to a considerable increase in U.S. oil and shale gas production in recent years.[119–122] Hydraulic fracturing involves the fracturing of low permeability reservoirs to recover the natural resources trapped in the shale formations.[123–125] A typical fracking fluid consists of water, proppant (mainly sand), viscosity modifying agents, and several other chemicals.[126] The proppant is suspended in fracturing fluid and transferred to the fissures to maintain the opening of these fractures during recovery. Therefore, characteristics of the fracturing (fracking) fluid play a crucial role in increased production efficiency.

In the last decades, the use of polymer based viscosity modifying agents for fracturing fluids such as poly(acrylic acid),[127] poly(vinyl alcohol),[128] guar gum and its derivatives (such as hydroxypropyl and corboxymethyl hydroxypropyl guar),[129] cellulose[130,131] and other poly(acrylamide) based polymers[198,132–134] has been reported. Polymer-based fracturing fluids have successfully been implemented in many fields in different countries.[135–138] However, most polymers generally suffer from poor salt and temperature tolerance, and also lose a downhole viscosity due to shear degradation on injection.[139,140] Furthermore, the formation of polymer residues and fouling during flowback can significantly reduce the well productivity.[141,142] As an alternative approach, aqueous based viscoelastic surfactant solutions have also attracted attention for enhanced oil recovery[143–146] and/or as hydraulic fracturing fluids.[147–151] The formation of rod-/worm-like micelles and/or gel structure, and their resulting entanglements account for the viscoelastic nature of such solutions.[152–156] Viscoelastic surfactant solutions lead to an improved permeability due to the elastic nature of proppant transport and the formation of a better fracture geometry.[142,157]

To further improve the current state-of-art in hydraulic fracturing, more effective fluids must be developed to satisfy the needs of fracturing. In particular, the newly designed fluids should have: (1) high viscosity during injection and pumping for efficient proppant transfer well to fractured fissures, and (2) low viscosity during flowback in order to; (i) leave the proppant in the fracture and (ii) prevent formation of any residue in these fissures, which will reduce the reservoir permeability.[158] Here, we report a pH responsive viscoelastic system obtained by supramolecular assembly of an amino amide and maleic acid in aqueous solutions to satisfy the abovementioned requirements. The rheological properties of the developed supramolecular system with proppant were examined as a function of pH, concentration of the solution, concentration of NaCl, and temperature. Moreover, the settling time of proppant (sand) was measured to quantify the sedimentation stability as a function of pH. The amino amide building block of the system was synthesized from stearic acid and N,N-dimethyl-1,3-propanediamine. While the former is a sustainable and environmentally friendly material obtained from cocoa butter, the latter is reaction product of dimethylamine and β-alanine, both of which are widely distributed in animals and plants.[159,160]

A.3. Materials and Methods

A.3.1. Materials and Sample Preparation

Maleic acid (>98%), N,N- dimethyl-1,3-propanediamine (DMPDA, >99%), and sodium fluoride (NaF, 99%) were purchased from Alpha Aesar (Ward Hill, MA). Aluminum oxide, (Al_2O_3, 150 mesh), hydrochloric acid (37%), stearic acid (95%), sodium hydroxide (≥97.0%) and sodium chloride, (NaCl, ≥98.0%) were obtained from Sigma Aldrich (St. Louis, MO). Sand (pure, 40-100 mesh) was supplied from Acros Organics (Geel, Belgium). Details of the synthesis of the pH-responsive supramolecular system were described in a previous work (Chen et al., 2014). Commonly used sand concentrations in hydraulic fracturing operations vary from 4 to 10 wt.% (Arthur et al., 2009). As such, a fixed sand concentration of 7 wt.% was employed in all experiments.

A.3.2. Rheological Measurements

A rotational rheometer (MCR301, Anton Paar GmbH, Graz, Austria) was used to conduct steady and dynamic rheology experiments. The rheometer was attached with a double gap cylindrical geometry (DG 26.7), with an effective cup length of 45 mm, and internal and external measuring gaps of 0.42 mm and 0.47 mm. respectively. Dynamic viscosity measurements were performed as a function of the shear rate between 10^{-3} s^{-1} and 10^{3} s^{-1}. Zero frequency viscosity for each condition were determined by extrapolating viscosity versus shear rate curves at low shear rates. In rheological studies, the main parameters of interest were solution concentration (0.5, 1, 1.5, 2, and 3 wt.%), pH (3.8, 5.3, 7.0, 8.3, and 9.6), temperature (22, 40, 58, 76, 94, 100, 110 and 120°C), and salt concentration (NaCl, 0.1, 0.5, 1, 3 and 5 wt.%). Effect of time on viscosity was tested at various temperatures (30, 60, 90 and 120 °C) and at a constant shear rate of 8.5 s^{-1}. Experiments in each condition were repeated at least three times for the statistical analysis.

A.3.3. Sand Sedimentation Studies

To study the proppant sedimentation in supramolecular solution, surface colored sand particles (GSB-5, Ceroglass Technologies Inc., Columbia, TN) in the same size range as pure sand were used in rheological studies to improve visibility in supramolecular solution. In these experiments, first, the pH of supramolecular solutions was adjusted to 4, 6, 8 and 10 using 0.05 M HCl or NaOH. Then, surface colored sand (7 *wt.* %) was added into the vials having a fixed volume of supramolecular solution and thoroughly agitated and well-stirred. For all solutions, photos were taken with a digital camera at various times until particles completely (>95%) settled down. The experiments were conducted at room temperature and 93 °C (200 °F).

A.3.4. Microstructural Analysis

To observe microstructural changes in the supramolecular solution and the interaction of the solution with proppants, images were taken via an Olympus BX51 optical microscope (Olympus America Inc., Melville, NY) at pH values of 3.8 and 8.3. Moreover, secondary electron micrographs were obtained at pH 4 and pH 8 via an FEI Quanta 650 ESEM (FEI, Hilsboro, OR) (Accelerating voltage: 10kV, and Pressure: 4 Torr-Low vacuum mode).

A.3.5. Zeta Potential Measurements

Zeta potential measurements were performed via Malvern Zetasizer Nano ZS instrument. Four solutions with pH 4, 6, 8 and 10 were diluted five times, 7 wt.% milled sand (submicron size) was added to each solution, and they were thoroughly stirred. Similar to the zeta potential measurements of the suspension, the zeta potential of bare solution and bare sand (in DI water) were also measured.

A.4. Results and Discussion

A.4.1. Effect of pH and Concentration

Figure 39a shows the effect of pH on the viscosity behavior of the supramolecular solution at a concentration of 2 wt.%. For all shear rates, viscosity increased with increasing pH and reached a maximum at pH 8.3. For a given pH, the supramolecular solution displayed a shear thinning behavior. Above the pH level of 8.3, the viscosity decreased with further increasing pH. The influence of pH on the viscosity can be better observed from the zero frequency viscosity (μ_0) curves (Fig. 39b). μ_0 is the measure of a maximum viscosity that a material can reach at very low shear rates, and indicates the resistance of the supramolecular solution against (i) sedimentation and (ii) deformation under long term loading.[161] μ_0 is effective when performing static proppant settling tests.

This switchable viscosity mechanism was ascribed to the complexation arising from protonation of amino groups and deprotonation of carboxyl groups. Considering that maleic acid has pK_a values of pK_{a1}=1.9 and pK_{a2}=6.1, maleic acid fully (~99%) dissociates one of carboxyl group above pH 3.9 and two of carboxyl groups above pH 8.1.[161] Likewise, given that pK_a of the amino-amide is 9.4, the amino-amide completely protonates below pH 7.4.[162] Hence, there exists an optimum pH value that leads to maximum electrostatic interactions of building blocks. At high values of pH, the lack of charge on the amino-amide is likely to be responsible for the decrease in complexation and viscosity.

Since a large amount of fracturing fluid is used in hydraulic fracturing, a significant factor that affects the cost of operation is the concentration of gelling agent used in the fracturing fluid. Figure 40a shows the viscosity as a function of shear rate at various concentrations at a given pH value of 8.3, at which the maximum viscosity was attained. To better illustrate the effect of concentration, the zero shear rate viscosity (μ_0) was also plotted as a function of concentration. These two parameters were found to be related to each other with a power law dependence: $(\mu_0/\mu_{solvent} -1)\propto C^a$ in accordance with in agreement with a reptation model.[163,164] At pH 8, the exponent for the supramolecular solution was found to be 2.1, which is greater than that for polyacrylamide solution (i.e. 1.0) with the same concentration range.[162] In other words, a wide range of viscosity can be obtained by altering the concentration of supramolecular solution, which is a desirable property in the context of viscosity adjustability.

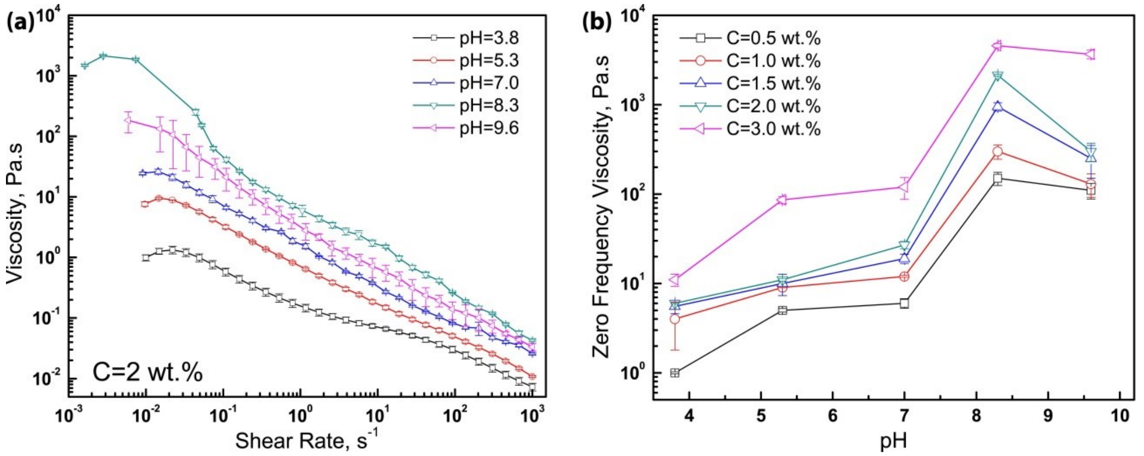

Figure 39. a) Effect of pH on the viscosity of the supramolecular solution at a concentration near 2 wt.%, and b) zero frequency viscosity as a function of pH where the values were extracted from the viscosity vs. shear rate curves in Figure 39a.

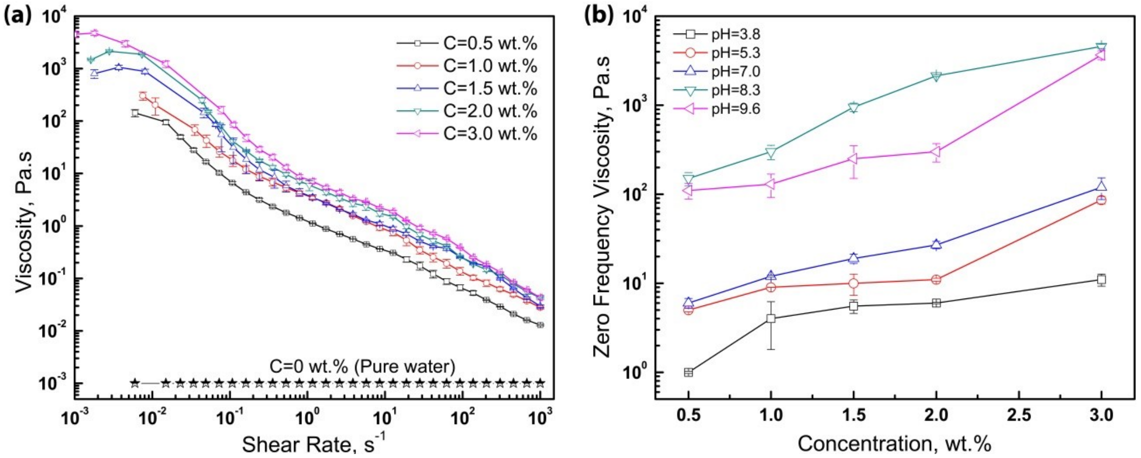

Figure 40. a) Effect of concentration on the viscosity of the supramolecular solution at a pH of 8.3, and b) zero frequency viscosity as a function of concentration where the values were extracted from the viscosity vs. shear rate curves in Figure 40a.

A.4.2. Effect of Salinity

Many oil reservoirs contain connate water with high concentration of salts.[164] In addition, seawater is the primary source of the injection water to increase oil projection, enhance recovery, and extend field life.[166,167] Therefore, the viscosity of the supramolecular system needs to be investigated in the presence of salt. In particular, NaCl was selected as the salt additive since seawater mainly consists of NaCl at average concentrations ranging from 3.2% to 3.6%.[168] Figure 41 demonstrates the effect of NaCl concentrations on the viscosity. At low and intermediate shear rates, the viscosity did not change noticeably with respect to salinity even up to 5 wt.% salt concentrations. On the other hand, the influence of salt was pronounced at high shear rates. However, the rheological integrity of the supramolecular solution was still preserved, and the solution was still highly viscous: namely, there was no total breakage and disintegration of the supramolecular assembly even up to 5 wt.% salt concentrations. Increased viscous dissipation at higher shear rates and the resultant disruptions in nanostructure of the supramolecular solution are presumably responsible for the differences in salt tolerance with respect to the shear rate. Overall, the supramolecular solution displayed a promising salt tolerance.

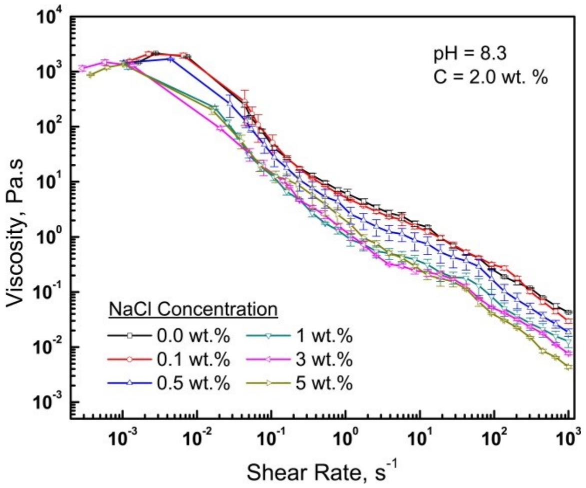

Figure 41. Effect of NaCl concentration the viscosity of supramolecular solution at a pH of 8.3 and concentration of 2 wt.%

A.4.3. Effect of Temperature

In drilling operations, since there is a temperature gradient from the ground to reservoirs at deep shale formations, it is important to examine how the supramolecular system behaves at elevated temperatures. Figure 42a displays the viscosity as a function of shear rates at eight different temperatures starting from 22 ºC up to 120 ºC. The solution viscosity decreased with temperature as expected. The temperature dependence of the viscosity is shown in Figure 42b with an Arrhenius type relation, $\mu=\mu_0 \exp(E_a/RT)$.[169] The activation energy (E_a) of the solution system was determined by the slope of the line on Arrhenius type plot and calculated to be 51.5 kJ/mol or 20.7kT (Fig. 42b). The E_a value of the supramolecular solution in the presence of sand is close to that of the bare solution with E_a at 21.1kT.[162] The change is minor mostly due to the small volume percentage of the sand in the supramolecular solution (less than 3%). Compared with a polyacrylamide solution, a commonly used polymer solution in displacement fluids with the E_a value of 6.4 kT, the activation energy for the supramolecular system is three times greater than that for polyacrylamide at the same concentration. Considering the operating temperatures at several reservoirs varying from 25 °C to 90 °C, such as the fields at Rock Spring (WY), Chaoyanggou (China), El Reno (OK) and Alberta (Canada) (Armstrong et al., 1996; Gaillard et al., 2013; Samuel et al., 2000, 1999; Wang et al., 2010),[120,123,142,170,171] our supramolecular system is less sensitive to temperature and less likely to suffer from thermal gradients in natural gas and oil reservoirs. Effect of time on the viscosity was also observed via tixotropy tests to confirm the long term reliability of the supramolecular solution system. Figure 42c indicates the viscosity measurements at four different temperatures from 30 °C to 120 °C. In all measurements except that at 120 °C, the viscosity initially decreases, eventually stabilize, and maintains its stability for more than six hours. At 120 °C the viscosity is relatively more stable, but shows some minor fluctuations which can be attributed to partial evaporation of water and phase separation. The long term viscosity behavior of the supramolecular solution at high temperature is comparable to polyacrylamide based gel,[132] and guar fluid.[172] Regarding its aqueous based nature, it can be claimed that the supramolecular solution maintains its viscous nature up to near 95 °C for long term operations.

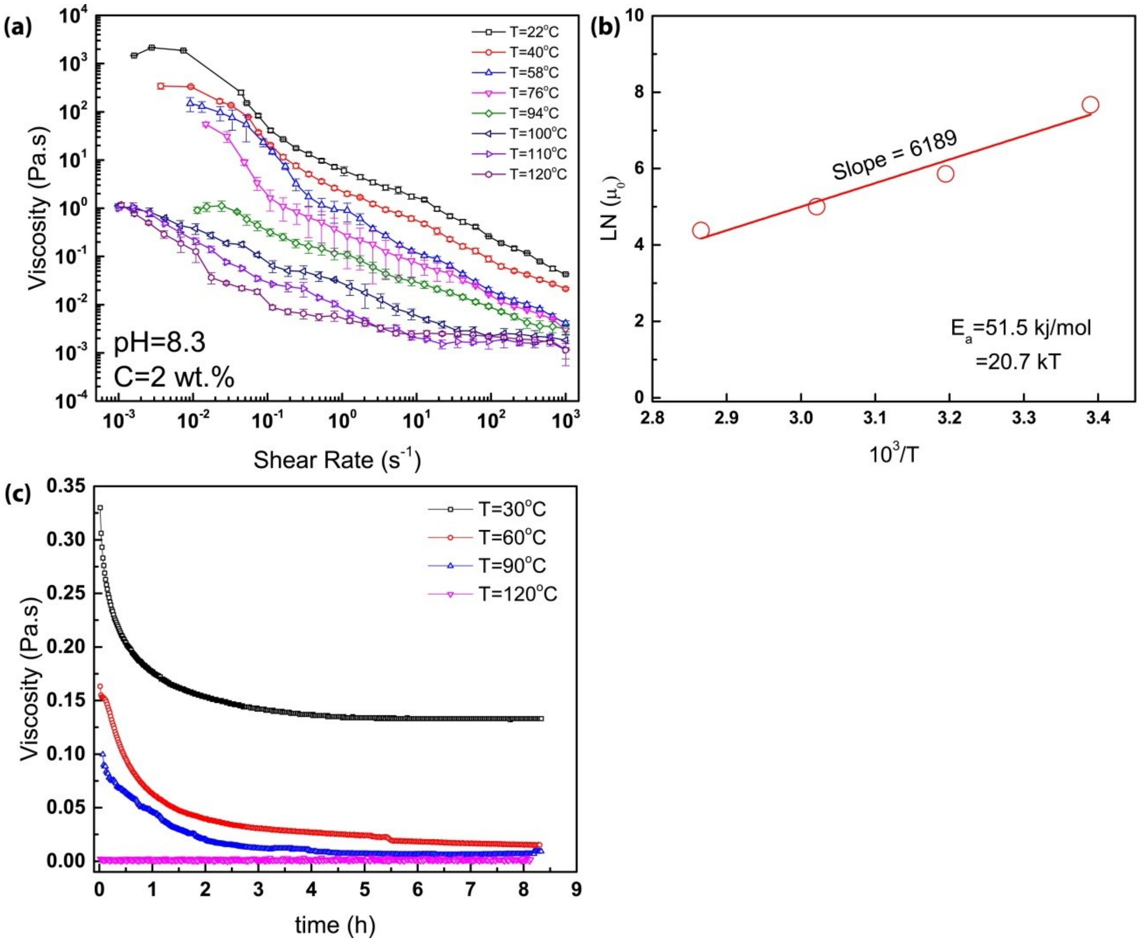

Figure 42. a) Effect of temperature on the viscosity of supramolecular solution at the operating temperatures of 22°C, 40°C, 58°C, 76°C, 94°C, 100°C, 110°C and 120°C. b) Natural logarithm of the corresponding zero frequency viscosities (μ_0) of supramolecular solution is plotted vs. 1/T in an Arrhenius type plot. c) Viscosity vs. time response of the supramolecular solution at temperatures 30°C, 60°C, 90°C, 120°C at a shear rate of 8.5 s^{-1}. In all figures, the solution pH and concentration are 8.3 and 2 wt.%, respectively.

A.4.4. Sand Sedimentation Studies

Settling of proppants is an important phenomenon influencing the efficiency of fracturing fluids. As such, the settling time of sand suspension in the supramolecular solution was investigated as a function of solution pH (Fig. 43). It was found that while the complete settling occurred within several seconds (~10 s) for solution of pH 4, and no settling was observed within 2 hours for solution of pH 6, pH 8 and pH 10. The complete settling (<95%) took place in 2 days and 5 days at pH 6 and pH 8, respectively. In other words, by changing pH from 4 to 8, the settling time can be increased from a few seconds to several days using the supramolecular solution described here. Further increasing the pH of the solution from pH 8 to pH 10, the settling time decreased to below 3 days. Settling velocity was $2.3 \pm 1.1 \times 10^{-3}$, $2.4 \pm 0.3 \times 10^{-7}$, $5.3 \pm 0.5 \times 10^{-8}$ m/s and $1.3 \pm 0.2 \times 10^{-7}$ m/s for solution of pH 4, pH 6, pH 8 and pH 10 respectively. Generally, proppant suspensions with settling velocities smaller 8×10^{-5} m/s (or 0.5 cm/min) are considered to be near perfect proppant suspension.[173] As such, the supramolecular solution can be claimed to demonstrate excellent proppant-carry capacity at pH 6, pH 8 and pH 10. Hydraulic fracturing application and recovery usually take about a week for greater depths. Due to their extremely slow settling time, the supramolecular suspensions described here are likely to conduct the proppants to the fissures through the whole well bore without significant sedimentation even for a week-long operation. *(See Support Information for high temperature settling tests)*

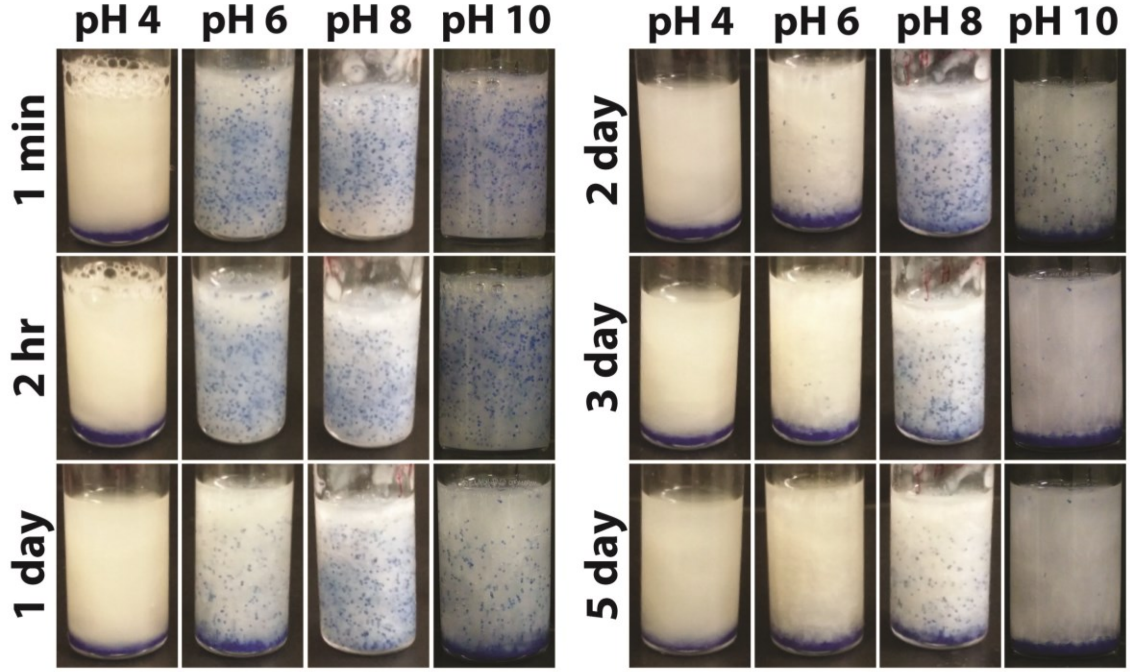

Figure 43. Particle settling in supramolecular solutions of pH 4, pH 6, pH 8, and pH 10 with time. The times for particles to completely settle down (>95%) in solutions of pH 4, pH 6, pH 8, and pH 10 were 10±5 s, 27±3 hrs, 5±0.5 days, and 2±0.3 days, respectively. The diameter of the vials was 1.5 cm and the height of the liquid level was 2.3 cm.

As a first approximation, the settling velocity, v_s, of proppant can be estimated using the Stoke's Law, which is expressed as:

$$v_s = \frac{2R^2(\rho_p - \rho_l)g}{9\mu} \qquad [9]$$

where R is the particle radius; ρ_p and ρ_l are the densities of particle and liquid, respectively; μ is the viscosity of solution. For the supramolecular solution developed, viscosity is a function of shear rate, $\dot{\gamma}$, (Fig. 39). For low Reynolds number regime, the average shear rate for a sphere settling in fluid can be calculated as:[174]

$$\dot{\gamma} = \frac{\sqrt{6}v_s}{2R} \tag{10}$$

Using on the viscosity based on average settling shear rate, ρ_p = 2.48 g/cm^3, ρ_l = 0.86 g/cm^3, and R = 175 µm, the settling velocity is calculated using Eq. 10 and compared with the experimentally measured settling velocity as a function of pH (Fig. 44).

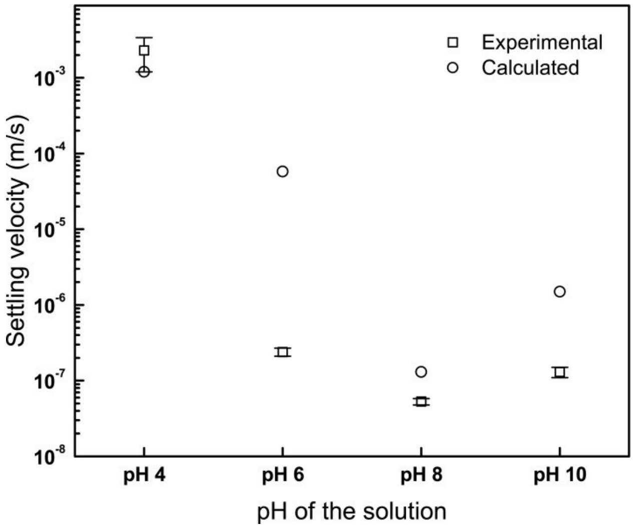

Figure 44. Experimental and calculated settling velocities of sand particle in the supramolecular solution

Similar to experimental settling velocities, calculated settling velocities decreased when increasing the pH of solution up to pH 8 and then increased after further increasing to pH 10. At pH 4, the experimental and calculated settling velocities were in a close agreement (*p*>0.2 with a t-test) where the supramolecular solution does not form any networks and entanglements. However, the experimental results were significantly (*p*<0.001) lower than the calculated results at pH 6, pH 8 and pH 10. Similar significant deviations from the Stoke's Law-based models have previously been observed in various systems, especially in viscoelastic wormlike micelle suspensions.[175–178] Microstructure networks in fracture fluids were found to decrease the settling velocity and increase the proppant suspension behavior.[179] One possible reason for this difference is the increased drag due to the strong inhomogeneous extensional flow near a sphere and the micellar deformation and strain hardening as reported by Chen and Rothstein.[175]

Alternatively, the differences in experimental and calculated values can also be ascribed to other factors influencing the drag force. For micellar suspensions, the drag can also be related with the Deborah number, De ($De = v_s \times \lambda / R$, where λ is the relaxation time): the drag could increase at high Deborah numbers.[175] Hence, at pH 6, the increased drag might be due to the larger relaxation time, which increases due to the formation of entangled supramolecular nanostructures upon changing from pH 4 to 6. In this study, the formation of networks and entanglements at high pH was experimentally confirmed using optical microscopy (Fig. 45a&b, marked with red circles, *more images with different magnifications are available in Supplementary Information*). At pH 8, the smaller settling velocity and shear rate due to high viscosity may decrease the Deborah number and thus decrease the increment of the drag. As for the solution of pH 10, the viscosity at pH 10 was between that at pH 6 and that at pH 8, and thus the increment of the drag was lower than that at pH 6 and higher than that at pH 8.

Furthermore, the intermolecular interactions between the settling particles and suspended supramolecular networks may play a role on the increased settling time at pH 8. To support this hypothesis, we calculated the interaction force between a nanocylinder and a sphere silica particle (300 µm in diameter) using the DLVO theory. Regarding the dimensions of the nanocylinder, we previously demonstrated that these networks and entanglements were essentially layered nano-cylinders with diameter of 400-500 nm and length of 10-20 µm using cryo-TEM.[162] Based on the zeta-potential, ζ of 40 mV and -54 mV, for nanocylinder and silica, respectively and the Hamaker constant of 1×10^{-20} J;[180] the total interaction force between the nanocylinder and silica was estimated to be ~1 *mg* at a distance of 100 nm and ~10 *mg* at a distance of 1 nm. Here, *m* denotes the mass of the silica particle (*Supplementary Information for the further details*). This analysis suggests that when the sand particle occasionally approaches/encounters the suspended supramolecular network during the settling, relatively strong intermolecular forces can arise, thereby preventing/hindering the particular settling (Fig. 45c).

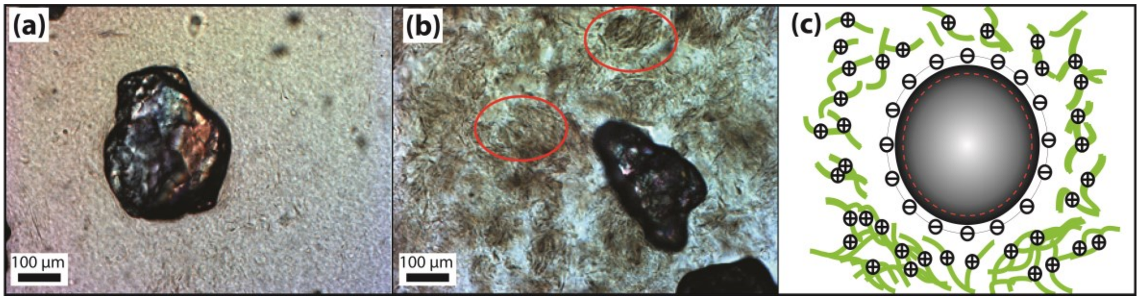

Figure 45. Micrographs of the sand particles in supramolecular solution at a) pH 4 and b) pH 8 (red circles indicates the network structure and entanglements. c) An illustration explaining the influence of intermolecular forces on the particle settling. The interaction zone between the sand particle and the supramolecular networks and entanglements is highlighted using the regions with dashed line. (See Supporting Information for more optical images, environmental SEM analysis and zeta potential measurements)

A.4.5. Application Potential

In hydraulic fracturing, initially, a high fracturing viscosity is desired to enable the effective transport and deposition of large volumes of proppant (sand) into the fissures. The apparent viscosity of commercially used fracturing fluids is generally 50 to 2000 times larger than that of water.[120] The supramolecular system described here could satisfy this viscosity range at concentrations as low as 0.5 *wt.*% for shear rates ranging from 0.1 s^{-1} to 1000 s^{-1}. After the pressure pumping operation is completed and the pressure on the fluid is released, the base fluid but not proppant must readily flow back into the well and not leave residues that impair permeability and conductivity of the fracture.[124] The supramolecular system can readily address this issue due to its highly adjustable nature of the viscosity with pH: Once the proppants reach the fissures, the viscosity of the system can be reduced by an external pH stimulus such as citric acid, which is natural and highly biodegradable acid. The reduced viscosity can, in turn, lead to the enhanced deposition of the proppants.

Aside from the highly adjustable viscosity behavior, the described supramolecular system has a great potential to be used as a fracturing fluid due to its sustainable nature. Stearic acid, one of the building blocks of the amphiphilic system is an environmentally friendly material obtained from cocoa butter. The other one, N,N-dimethyl-1,3-propanediamine has been shown to be a biodegradable molecule as a result of activate sludge and the half-life tests where photochemical-oxidative degradation in the atmosphere by OH radicals is 3.2 hours (NTP, 2004). As such, the harmful effects of hydraulic fracturing[181,182] due to fracturing fluids may be decreased up on use of such a supramolecular system.

Regarding commercial adjustable viscosity fracturing fluids, borate cross-linked fracturing fluids are the most widely used aqueous-based cross-linked fluid systems in use today.[126,173,183] The viscosity of a borate fracturing fluid and the proppant settling velocity can change 10-20 fold at a shear rate of 40 s^{-1} by changing pH from 8 to 10.[173,183] Meanwhile, the supramolecular system in this study shows the similar variations in viscosity at the same shear rate upon changing pH from 3.8 to 8.3. However, borate cross-linked fracturing fluids display poor stability in presence of seawater,[173] while our supramolecular system maintains its rheological integrity even up to 5 wt.% NaCl concentrations.

Salts of amine with aliphatic groups (e.g. ClearFRAC™) are commercial viscoelastic based fracturing fluids that have been used in more than 2000 fracturing jobs around the world.[142] The described supramolecular system has certain advantages over such viscoelastic fluids: At around 23 °C and a shear rate of 100 s^{-1}, while the supramolecular system required a concentration of 2.0 wt.% to achieve a viscosity of 380 cp, commercial fluids based on long chain amine salts needed a concentration of 4.0 wt.% to yield 400 cp.[142] In other words, similar gelling performance can be achieved with a smaller amount of material using the supramolecular system. For fracturing fluids based on amine salts with aliphatic groups at 23 °C and 4.0 wt.%, the viscosity decreases from 420 cp to 380 cp by adjusting pH from 8 to 4, which is not responsive to pH.[142] For our system, the viscosity decreases from 380 cp to 8 cp by adjusting pH from 8 to 4, indicating a ~40 fold improvement in the adjustability of viscosity.

A.5. Conclusion

This paper presents a highly pH tunable, salt tolerant, supramolecular fracturing fluid involving aminoamide and maleic acid in an aqueous solution. The viscosity of the supramolecular solution with proppant (sand) was investigated as a function of solution concentration, pH, temperature and salt concentration. As the solution pH increased, the viscosity increased up to a pH of 8.3. Further increases in pH decreased the viscosity. At a concentration of 2 wt.%, by altering pH from 4 to 8 or vice versa, the sedimentation time of sand particles can be adjusted about five orders of magnitude. At pH 8 and 2 wt.%, supramolecular solution displayed a very high proppant carrying ability with an extremely low sand sedimentation velocity of 5.3×10^{-8} m/s. The viscosity showed an exponential increase with concentration with a larger exponential coefficient than that of conventionally used viscosity modifier, polyacrylamide solution. Salinity did not significantly affect the viscosity of the supramolecular fracturing fluid with NaCl concentrations up to 5 wt.%, which makes the fluid compatible with sea water. The viscosity of the supramolecular fracturing fluid decreased with increasing temperature with the activation energy of 20.7 kT. The pH responsive supramolecular solution described in this work has a potential to significantly improve proppant transport and deposition, to decrease the damage on fracture during the flowback period, and to reduce environmental impact due to their natural building blocks and high biodegradability.

A.6. Supporting Information

A.6.1. Microstructural Analysis

Optical images were taken to investigate the structural changes on the samples with low and high pH, and dispersion of the silica particles in the solution. Figures 46a through c indicate images of the supramolecular solution with a pH of 3.8, while Figures 46d through f show that of pH 8.3. The network structure and entanglement are clearly observed in high magnification images (Fig 46c and S46). The degree of entanglement and network formation increases when the pH increases from 3.8 to 8.3. Thus the supramolecular solution may provide a sufficient force around the sand due to the entanglement and prevents the sedimentation. This helps to increase transfer capacity of the fracking fluid.

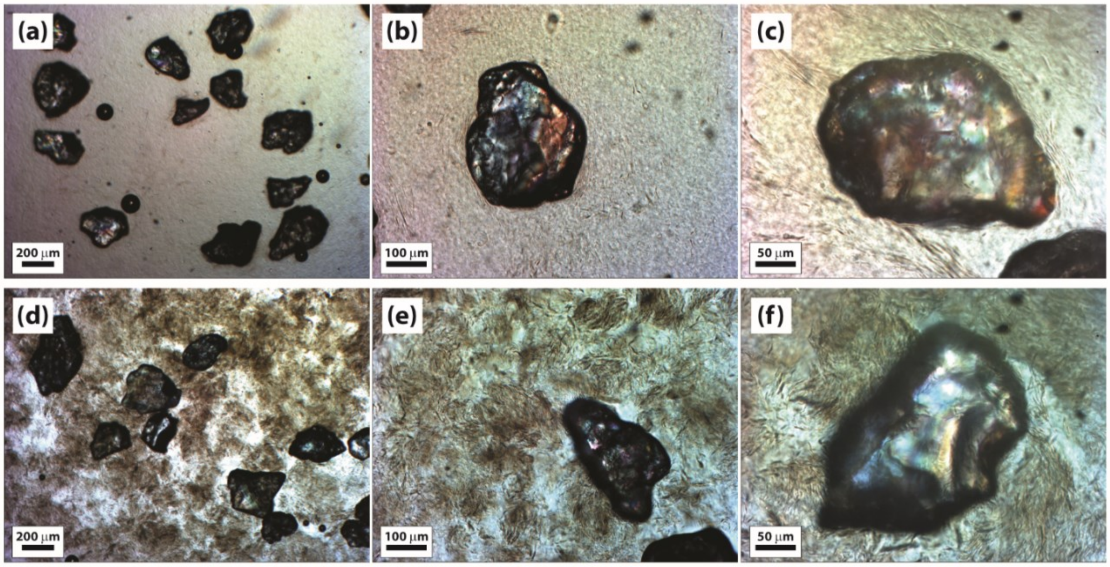

Figure 46. Optical micrographs of the supramolecular solution containing 7wt% silica sand for the pH 3.8 (a-c) and pH 8.3 (d-f).

Environmental SEM analysis was performed to obtain higher resolution micrographs and support the optical images. Figure 47 indicate the secondary electron micrographs of the supramolecular solution and sand particles. These micrographs show more details about the interaction of the supramolecular solution with the proppant. At pH 4, the sand particles easily sediment since the solution does not provide sufficient force to suspend these particles due to decrease in complexation and dissociation of the micellar structure (Fig. 47a-b). The network formation due to complexation is pronounced more at pH 8 (Figure 47c-d), which increase the viscosity, and hinders the sand movement[149]. At this pH, the proppants are buried in the solution, and their boundaries are not shown clearly since the network structure covers these proppants. As such, imaginary boundaries were drawn to identify the boundaries of the proppants in the solution.

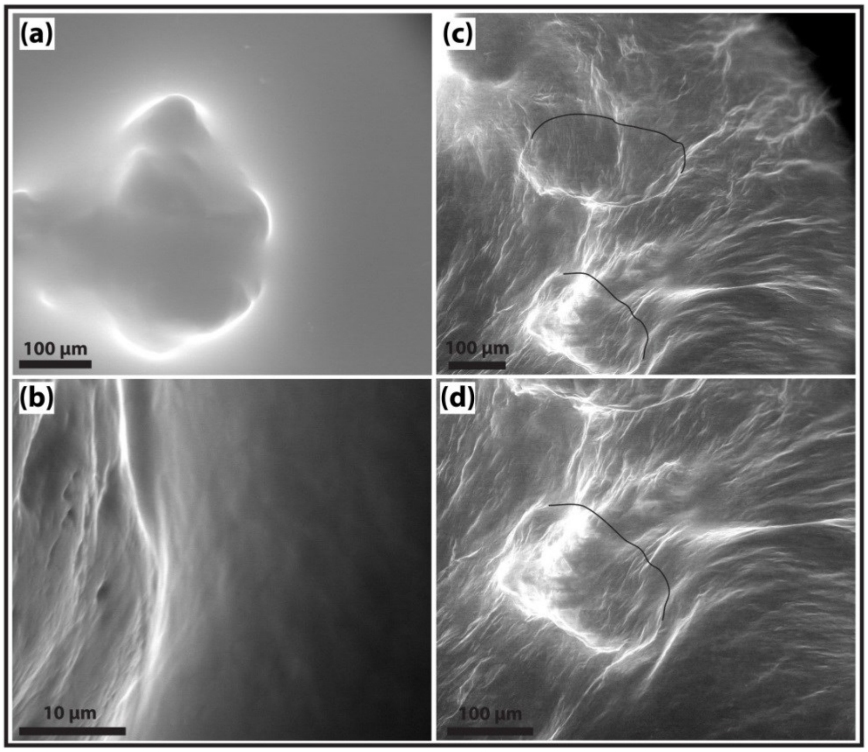

Figure 47. ESEM Micrographs of the sand particles in supramolecular solution at (a, b) pH 4 and (c, d) pH 8. Imaginary boundaries of sand particles were drawn on micrographs obtained at pH 8.

A.6.2. Zeta Potential Measurements

Figure 48 (or Table 4) indicates the zeta potential measurements of the bare supramolecular solution, bare sand, sand suspension solution. The measured zeta potential of bare sand agrees well with the theoretical results.[184] In all measurements, zeta potential gradually decreases with increasing pH. These measurements suggest the formation of a supramolecular network in the form of a shell around the sand suspended in the solution. Therefore, a positive surface charge occurs in presence of the supramolecular solution.

Table 4. Zeta potential measurements of sand, supramolecular solution, and the solution with sand dispersed in it, as a function of pH.

pH	**Zeta Potential (mV)**		
	Surfactant+Sand	Bare Sand	Bare Surfactant
4	41.5 ± 1.35	-10.05 ± 1.04	42.9 ± 2.08
6	21.6 ± 0.85	-18.33 ± 2.72	28.2 ± 1.61
8	19.53 ± 0.23	-48.27 ± 1.89	19.97 ± 1.21
10	8.01 ± 0.8	-51.03 ± 0.25	9.48 ± 1.3

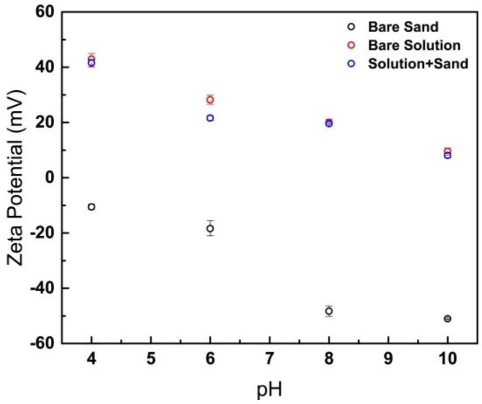

Figure 48. Zeta potential measurements of sand, supramolecular solution, and the solution with sand dispersed in it, as a function of pH.

A.6.3. Sand Sedimentation Tests at High Temperature

Sand sedimentation study of the supramolecular solution system was performed at 93 °C (200 ˚F) to test the reliability of this solution system at elevated temperatures (Fig. 49). The settling of proppants was observed with time at pH 6, pH 8 and pH 10. pH 4 was excluded since the solution did not show proppant suspension ability at room temperature settling tests. No settling was observed in the solutions in the first five minutes, while the solution with pH 6 dissociated and complete settling occurred in 10 minutes. Even though some dissociation occurred in the other solutions, they were still suspending significant amount of the proppants. At pH 10, the settling completed in 20 minutes, while the proppants were still suspended at pH 8 after 30 minutes. Eventually, dissociation and complete phase separation was observed in the pH 8 solution at 40 minutes, settling completed. Similar to the room temperature settling tests, pH 8 provides the best proppant carrying capacity at high temperatures. This solution system has much better proppant carrying capacity than guar fluid at all temperatures, and is comparable to the novel viscosifier that has recently been reported.[172]

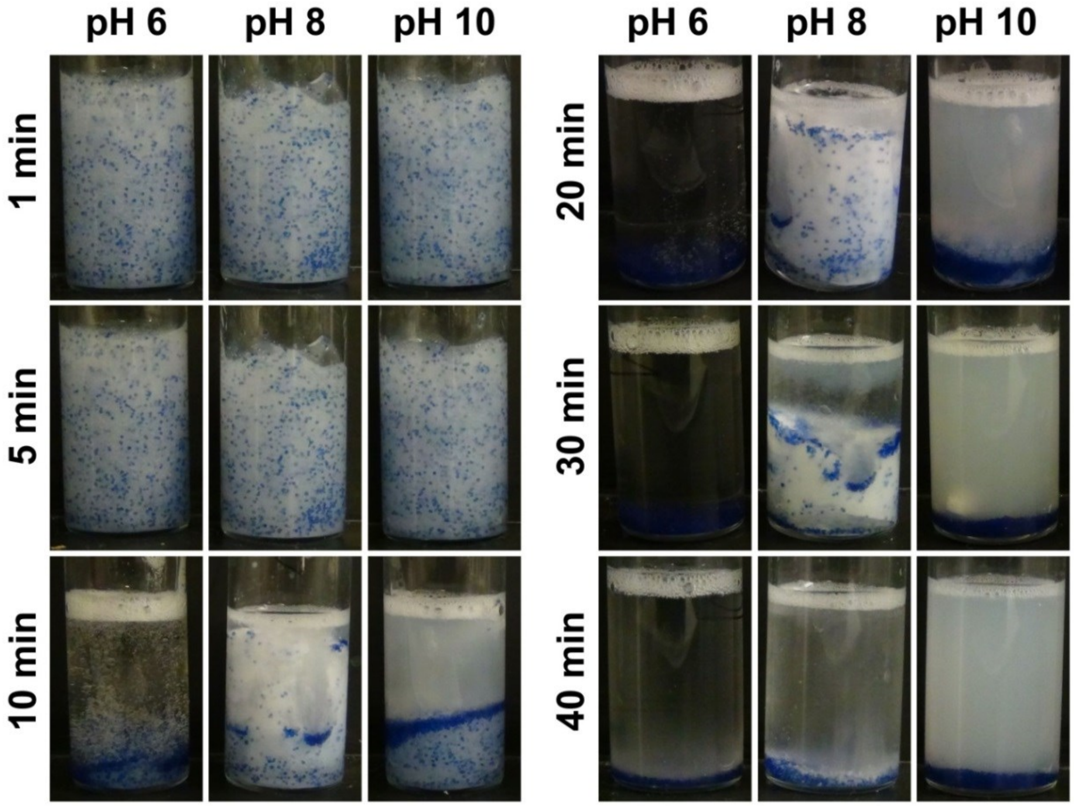

Figure 49. Proppant settling study at 93 ˚C (~200 ˚F). Particle settling in supramolecular solutions was observed at pH 6, pH 8, and pH 10 with time. The times for particles to completely settle down (>95%) in solutions of pH 6, pH 8, and pH 10 were less than 10 min, between 10 min and 20 min, and between 30 min and 40 min. The diameter of the vials was 1.5 cm and the height of the liquid level was 2.3 cm.

A.6.4. Calculation of Interaction Force

The interaction force between a sand particle and a nano-cylinder and a sphere silica particle involves van der Waals interaction and double-lay interaction. Since the size of nano-cylinder (500 nm in diameter and 10 µm in length) is much smaller than the silica particle (300 µm in diameter), the nano-cylinder could be approximated as a series of smaller sphere particles (500 nm in diameter) with the number of L/2R$_2$, where L is the length of the nano-cylinder and R$_2$ is the radius of the nano-cylinder.

The van der Waals force between two sphere particles at short distance (h << R$_1$ or R$_2$) can be calculated by:[185]

$$F_{VW}(h) = \frac{AR_1R_2}{(R_1+R_2)6h^2} \qquad [11]$$

where *A* is the Hamaker coefficient and *A* $\sim 1\times10^{-20}$ J for most organic molecular/water/silica system; [180] *h* is the distance between the two spheres.

The double layer interaction energy between two sphere particles is given as;[186]

$$F_{DL}(h) = 64\pi\varepsilon_0\varepsilon\left(\frac{kT}{e}\right)^2 tanh(e\psi_1)\tanh(e\psi_2)\frac{R_1R_2}{(R_1+R_2)}e^{-\kappa h}\cdot(-\kappa) \qquad [12]$$

where ε is the dielectric constant of the medium; ε_0 is the permittivity of free space; e is the electron charge; *k* is Boltzmann constant; T is temperature; ψ_1 and ψ_2 are the surface potential of the nano-cylinder and silica surface, respectively; and κ^{-1} is the Debye length. Surface potential of silica sand is -54 mV while the surface potential of nano-cylinder is about 40 mV (from imine materials).[179] With ε = 78.38 and κ^{-1} = 65 nm for water medium. The whole force at different distance could calculated and $F(h$=100 nm) ~1 mg while $F(h$=1 nm) ~10 mg, where m denotes the mass of the silica particle.

APPENDIX B

THE EFFECT OF NANOPARTICLE FUNCTIONALIZATION ON LUBRICATION OF NANOFLUIDS DISPERSING SILICA NANOPARTICLES IN AN IONIC LIQUID*

B.1. Abstract

Recently, ionic liquids (ILs) have received attention as lubricants owing to their intriguing properties such as tunable viscosity, high thermal stability, non-flammability, and corrosion resistance. In this work, we investigate how the incorporation of octadecyltrichlorosilane (OTS) functionalized silica nanoparticles in 1-butyl-3-methylimidazolium (trifluoromethysulfony)imide, influences the tribological properties and rheological properties of IL under boundary lubrication and elastohydrodynamic conditions, respectively. It was found that coefficient of friction depended on the concentration of NPs in IL with a concave upward functional trend with a minimum at 0.05 wt.% for bare silica NPs and at 0.10 wt.% for OTS-functionalized silica NPs. For steel-steel contact, the presence of functionalized nanoparticles in IL decreased the coefficient of friction by 37% compared to IL and 17% compared to IL with bare silica NPs. While IL with bare NPs demonstrated a shear thinning behavior for all concentrations, IL with functionalized NPs showed a Newtonian behavior at low

---

*Reprinted with permission from "The effect of nanoparticle functionalization on lubrication performance of nanofluids dispersing silica nanoparticles in an ionic liquid" by Cengiz Yegin, Wei Lu, Bassem Kheireddin, Ming Zhang, Peng Li, Younjin Min, Hung-Jue Sue, Mufrettin M. Sari and Mustafa Akbulut. *Journal of Tribology,* [In Print].[187] Copyright 2016 by ASME Journals.

concentrations and shear thinning behavior at high concentrations. Overall, this study provides insights into the anti-friction and anti-wear additives for lubrication systems.

B.2. Introduction

Friction and wear result in waste of resources, reduction in lifetime of mechanical components, increase in production costs, high-energy consumption, and hence high CO_2 emissions.[188–190] As such, lubrication is essential to increase the efficiency, reliability and operational safety of mechanical systems.[191] Since the discovery of mechanical devices, numerous lubricants have been developed and used to minimize wear and friction.[192] Typically, lubricants consist of a base fluid and one or more additive(s), the total amount of which can vary from less than 1% to 30% depending on the application.[193] The base oil refined from the petroleum, the function of which is to lubricate and to act as a carrier of additives, is categorized under two classes: mineral oil (solvent refined, hydrotreated, or hydrocracked petroleum crude oil) and synthetic oil. The additives are often used to impart useful properties into the lubrication system such as anti-wear, antioxidation, corrosion inhibition, anti-foam, pour-point reduction, and viscosity index improvement.[189,194]

The key challenges associated with mineral oils are that (i) they form waxes at low temperatures, resulting in poor flow properties, (ii) they are vulnerable to oxidation at continuous high temperature operations (i.e. 180 ˚C),[195,196] causing sludge and acid buildup, and (iii) there are environmental concerns regarding high emissions due to their volatility and poor biodegradability.[197–199] While synthetic oils such as polyalphaolefins and polyolesters alleviate some of the above-mentioned problems owing to their relatively higher thermal stability, lower volatility, and enhanced biodegradation,[200] these issues are not fully resolved.[201] There is still a room for improvement to push thermal stability and non-volatility of base oils to higher levels without compromising the lubrication efficiency. In this context, ionic liquids (ILs), also known as neoteric solvents, have received a great attention as synthetic base oils because of their intriguing properties such as very high thermal and chemical stability, non-volatility and low vapor pressure, non-flammability, high boiling and low melting points, high biodegradability, and low toxicity and carcinogenity.[197,202–208] Furthermore, there is the possibility of producing "designer lubricants" via the selection of different anion and cation combinations, with the objective of tailoring their properties for a particular application.[209]

Various types of ILs have been tested and reported to effectively lubricate common tribo-pairs including steel,[210–217] aluminum,[216,218,220] copper,[220] and ceramic contacts.[221–226] Most of these studies have focused on ILs involving imidazolium cations and hexafluorophosphate (PF_6) and tetrafluoroborate (BF_4) anions containing different alkyl groups. Recently, studies dealing with other cations such as phosphonium,[227–229] choline,[230,231] pyridinium,[232] and pyrrolidinium[233] have also appeared in the literature. As with other types of base oils, there are active efforts ongoing for the search of better additives for ILs: This is particularly needed for ILs due to the differences in chemistry of ionic liquids and common base oils for which most additives are designed for. Only a limited number of studies have concentrated on this issue, mostly stemming from the recentness of the discovery of their desirable lubrication properties.[202,234–237] To be specific, for instance, Khare et al.[238] have recently demonstrated anti-wear additive properties of graphite for 1-butyl-3-methylimidazolium iodide. Wang and co-workers used various imidazolium containing ILs with functionalized graphene,[239] multiwall carbon nanotubes,[240] polytetrafluoroethylene[241,242] and they generally observed significant anti-wear behaviors and friction reduction. Carrion et al.[243] have relied on single-walled carbon nanotubes as additives for improving anti-wear performance of 1-octyl, 3-methylimidazolium chloride. Gusain and Khatri[244] have reported the dispersion of CuO nanorods in 1-hexyl-3-methylimidazolium acetate to achieve superior wear resistance for steel contacts. Silica nanoparticles, considered as green nanoparticles, are another type of additives that have also been used in lubricant oils due to their availability, mechanical robustness and biocompatibility.[245–247] Their high stiffness can help enhance the lubrication performance via increased rolling performance, and reduce the surface roughness and rolling force.

The objective of this study is to determine the influence of the presence and functionalization of silica nanoparticles on the rheological and tribological properties of 1-butyl-3-methylimidazolium (trifluoromethysulfony) imide. Frictional properties were evaluated using the nanotribometry with steel-steel tribo-pairs under boundary lubrication conditions while rheological properties were characterized with a rheometer in a rotational mode. Wear characteristics were probed using ex situ SEM measurements conducted after friction experiments. In addition, the colloidal stability of bare and functionalized silica nanoparticles in this ILs, which is an important parameter to consider for designing an additive for a lubricant, was investigated using dynamic light scattering.

B.3. Materials and Methods

B.3.1. Materials

Silicon dioxide (silica) nanoparticles (10-20 nm in size) and ionic liquid 1-butyl-3-methylimidazolium (trifluoromethysulfony) imide (≥ 98%) were obtained from Sigma-Aldrich (St. Louis, MO). Stainless steel plates with a mirror polish were supplied from Metals Depot (Winchester, KY). Octadecyltrichlorosilane (OTS) was purchased from Gelest Inc. (Morrisville, PA). Spectra/Por® 4 Dialysis Membrane (MWCO: 12-14,000 Daltons) was purchased from Spectrum Laboratories Inc. (Rancho Dominguez, CA). All materials were used as received.

B.3.2. Functionalization of Silica Nanoparticles

Figure 50a-c illustrate the functionalization of silica nanoparticles (SiO_2 NPs) with an organosilane (OTS), a transmission electron micrograph (TEM) of SiO_2 NPs, and resulting core–shell structure,[248–250] respectively. In this scheme, the first step was the addition of bare silica nanoparticles to the solution of chloroform and hexane (1:4 in volume). The mixture was then sonicated for 30 minutes to form a meta-stable colloidal suspension. The ligand OTS was added into the mixture dropwise (ten times as much quantity as that of the SiO_2 NPs) and final solution was sonicated for 10 hours to accomplish the functionalization of the nanoparticles. The unreacted or excess OTS was removed from the mixture by dialysis in chloroform for 8 hours, using the membrane having pore size of 7-8 nm. Finally, the solution was dried using a vacuum oven at room temperature to obtain the OTS-functionalized SiO_2 nanoparticles.

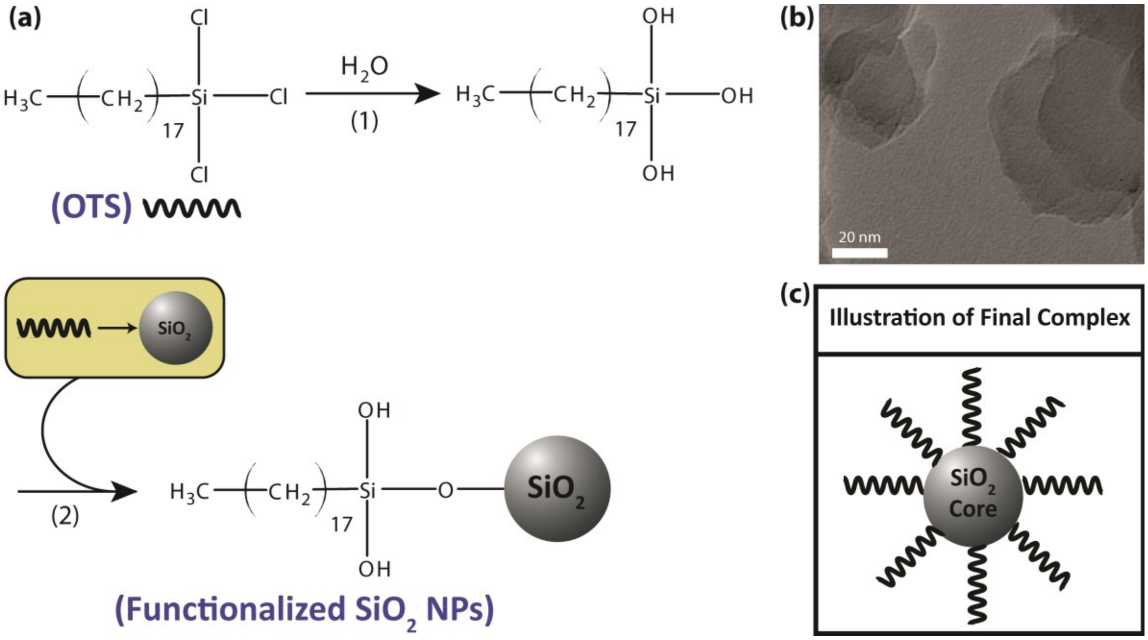

Figure 50. a) Reaction scheme for the functionalization of SiO_2 NPs with OTS, b) TEM micrograph of bare SiO_2 NPs, and c) schematic illustration of the final product

B.3.3. Characterization of Silica Nanoparticles

Transmission electron microscopy (TEM) was used to identify the shape of the silica NPs. The NPs dispersed on a CF400-CU copper grid (Electron Microscopy Sciences) was analyzed via a JEOL JEM-2010 TEM at 200 kV accelerating voltage with 0.23 nm point resolution.

Fourier transform infrared (FTIR) spectroscopy was used to examine the surface modification of silica NPs. In the FTIR experiments, functionalized nanoparticles were mixed with KBr powder, and then compressed at 275 MPa to form pellets, which were then characterized using an FTIR spectrometer (FT-IR100, Thermo Nicolet).

The degree of OTS functionalization on nanoparticle surfaces was determined using a thermogravimetric analyzer (TGA, Q500, TA Instruments, New Castle, DE). In these experiments, the samples were heated from 25 ˚C to 900 ˚C under nitrogen flow at a rate of 10 ˚C min^{-1} to ensure that the chamber temperature reaches a temperature above the decomposition temperature of OTS groups.

Using dynamic light scattering (DLS, Zetasizer Nano ZS90, Malvern), the size distributions of both bare and OTS-functionalized SiO_2 NPs in the IL were determined. We define the time, *t*, at which the sonication of samples was just completed as the starting point, *t*=0. From this point on, the samples were characterized via DLS at predefined intervals to determine the colloidal stability of nanoparticles in IL as a function of time.

B.3.4. Friction Measurements

The steel sheets were cut to form substrates with a dimension of 2 cm × 2 cm. Before testing, they were cleaned with acetone and dried with nitrogen (N_2). Then, OTS-functionalized SiO_2 NPs dispersed in IL with systematically varying nanoparticle concentrations (from 0.01 % wt. to 3% wt.) were placed on the steel substrates. Nano-tribometer (CSM Instruments, Switzerland) was used to take friction response at a total distance of 1 mm per cycle and a constant sliding speed of 0.5 mm/s, and 1000 cycles were completed for each experiment (2,000 seconds). All measurements were accomplished by shearing a highly smooth stainless steel sphere (diameter ~ 2 mm) with *rms* roughness of 2.14 ± 0.45 nm on a steel substrate. The smooth stainless steel sphere was lying along a cantilever with normal and tangential stiffnesses of 150 N/m and 128 N/m, respectively. The normal loads of 5.0, 10.0, 15.0, 20.0, 30.0, and 40.0 mN were applied for each test. For each loading value at least three measurements were taken at several points, and their averages were reported. The coefficient of variance was less than 10% for all measurements. The humidity was kept between 45-50 % throughout this study.

B.3.5. Rheological Tests

Rheological measurements were carried out using an Anton Paar Rheometer Physica MCR 301 (Ashland, VA) with a cone-and-plate geometry (50 mm diameter, 0.987° cone angle). The gap was set to 0.05 mm throughout the measurements. The shear rate range for measurements were about 1 s^{-1} to 1000 s^{-1}. The experiments were conducted using pure IL, bare silica nanoparticles dispersed in IL, and OTS-functionalized nanoparticles dispersed in IL with nanoparticle concentrations of 0.05 %, 0.1%, 1%, and 5% by weight at 22 °C. Each measurement was repeated at least three times for statistical reliability.

B.3.6. Surface Wear Analysis

The deformation and wear on the steel surfaces in presence of pure IL, IL with bare and OTS-functionalized SiO_2 NPs were analyzed using a QUANTA 600 Field

Emission SEM (FEI, Hillsboro, OR) with 10kV of accelerating voltage and 3A of beam current. The wear rates were assessed by comparing the width of wear tracks from SEM images.

B.4. Results and Discussion

B.4.1. Characterization of OTS-functionalized SiO_2 NPs

Figure 51 shows the FTIR spectra of the pure OTS, bare SiO_2 NPs, and OTS-functionalized SiO_2 NPs ranging from 4000 cm^{-1} to 400 cm^{-1}. It was observed that the characteristic double band of Si-Cl stretching at 567 cm^{-1} and 588 cm^{-1} disappeared upon the functionalization reaction. Another difference between the FTIR spectra of bare and OTS-functionalized SiO_2 NPs was the peak observed at 1467 cm^{-1}, which is due to the asymmetric CH_3 bending. For both bare and functionalized SiO_2 NPs, peak at 800 cm^{-1} was ascribed to the symmetrical stretching vibration of Si-O while the peaks at 1082, 1072 cm^{-1}, 964 cm^{-1} and 952 cm^{-1} were attributed to the asymmetric Si-O-Si stretching. Overall, the FTIR analysis of the samples indicates that after the functionalization reaction, the surface of silica NPs contained OTS molecules and Si-Cl molecules of OTS chemically reacted with silica NPs.

B.4.2. Determination of OTS Coverage on SiO_2 NPs

Figure 52 demonstrates the TGA thermogram of bare and OTS-functionalized SiO_2 NPs. For both samples, the weight decreased around 100 ˚C due to evaporation of

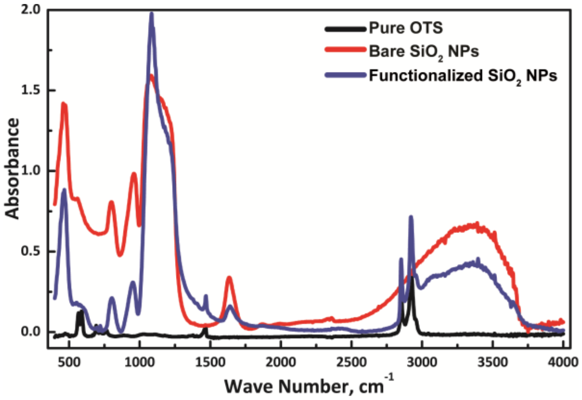

Figure 51. FTIR spectra of pure OTS, bare SiO$_2$ NPs, OTS-functionalized SiO$_2$ NPs within the frequency range of 400-4000 cm^{-1}.

water. Here, the smaller decrease in the OTS-functionalized silica NPs compared to the bare silica NPs is due to the hydrophobic nature of OTS-functionalized sample. Above 100 ˚C, the bare silica NPs remained stable for elevated temperatures with no substantial loss of weight. Meanwhile, the functionalized SiO$_2$ sample was stable up to 239 ˚C, above which the organic portion (octadecyl) of the modified NPs decomposed and the weight decreased drastically. As a result of heating from 239 ˚C up to 900 ˚C, the weight loss of the functionalized silica sample was around 30 wt.%. Based on this value, the surface density of the octadecyl group was calculated to be approximately 13.4 μmol/m^2.

B.4.3. Colloidal Stability of OTS-functionalized SiO$_2$ NPs

Colloidal stability, which can be regarded as the capability of an additive to remain in dispersion without any precipitation during prolonged storage, is a major factor to consider while designing new lubrication systems. As illustrated in Figure 53a, the functionalization of NP surfaces with organosilane molecules improved the colloidal

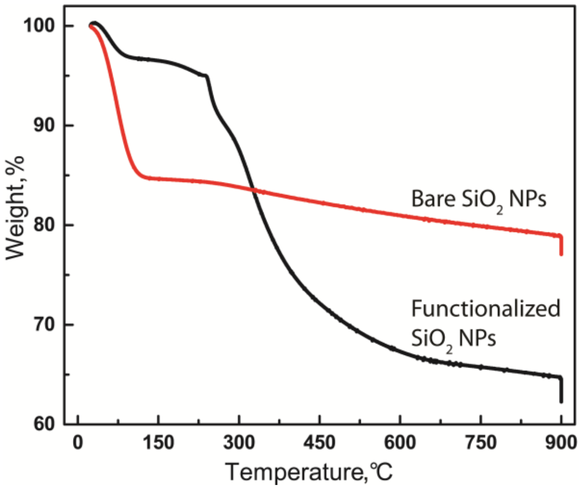

Figure 52. TGA thermogram of bare and OTS-functionalized SiO_2 NPs between room temperature and 900 ˚C under nitrogen atmosphere. Heating rate is 10 ˚C min$^{-1.}$

stability as evidenced by the lack of sedimentation and presentations from photographs. To quantify and better understand the dynamics of colloidal instability, we relied on time resolved dynamics light scattering. Right after the sonication step, both bare and OTS-functionalized SiO_2 NPs had a very similar size distribution peaking around 40 nm (Fig. 53b). For the case of bare SiO_2 NPs, shortly after the preparation of colloidal suspension, the particle size distribution transitioned from unimodal to bimodal (Fig. 53c). This finding suggests that the bare particles aggregate with time. On the other hand, no significant change in the particle size distribution was observed for functionalized SiO_2 NPs. Moreover, further particle size distribution data of the functionalized SiO_2 NPs were collected up to 24 hours to determine when (or if) the functionalized NPs tend to start aggregation (Fig. 4d). The functionalized SiO_2 NPs maintain their colloidal stability in the IL up to 6 hours and slowly aggregate after that. Thus, it can be stated that OTS-functionalized NPs have a better colloidal stability in IL than the bare ones. The possible reason is that the surface of the nanoparticles adsorbed around by the organic modification agent can screen out the attractive Van der Waals interactions to prevent the agglomeration.[245,251,252]

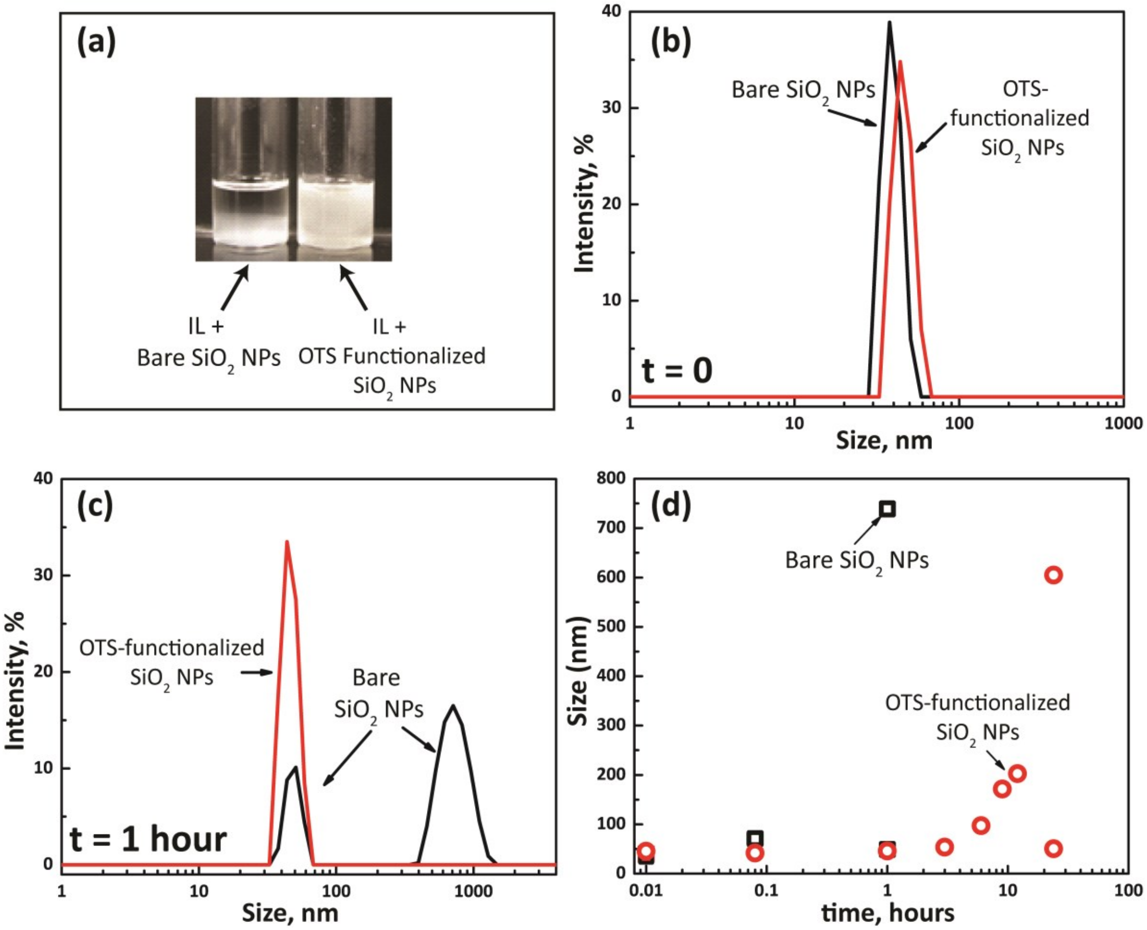

Figure 53. a) The sedimentation of 0.05 wt.% bare (left) and 0.1 wt.% OTS-functionalized SiO_2 NPs in IL (right) after 24 hours from preparation, (b, c) particle size distribution of bare and OTS-functionalized SiO_2 NPs in IL measured by DLS right after preparation (t=0) and after 1 hour, respectively, and d) particle size of the bare and OTS-functionalized SiO_2 NPs in IL as a function of time. The existence of two data points for certain time points indicates the bimodal size distribution. Even if the actual concentration of nanoparticles were lower for the case of functionalized nanoparticles, they displayed a better colloidal stability.

B.4.4. Effect of NP Concentration on Friction

In lubrication systems, the additive content plays an important role on tribological properties. As such, the effect of NP concentration on the friction coefficient of the OTS-functionalized SiO_2 NPs was measured within a range between 0.01 wt.% and 5 wt.% (Fig. 54). It was found that the friction coefficient decreased with increasing nanoparticle concentration, and reached a minimum at 0.1 wt.%. Then, it gradually increased by further increase in the concentration, which indicates that 0.1 wt.% is the optimal concentration of functionalized SiO_2 NPs in the IL.

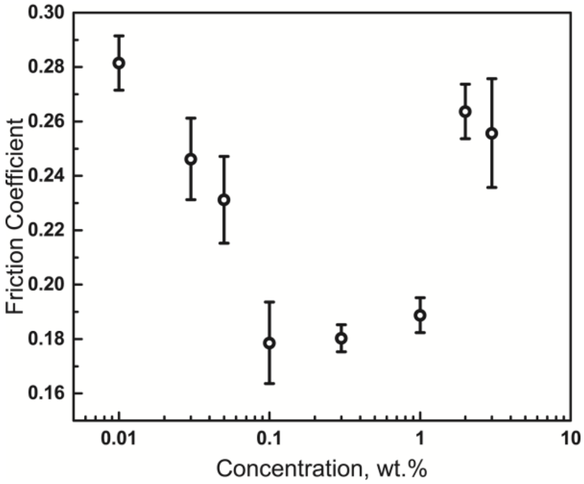

Figure 54. Effect of NP concentration on the friction coefficient of the OTS-functionalized SiO_2 NPs

A relatively high friction coefficient at low concentrations is presumably due to an insufficient number of NPs to prevent asperity-asperity contact.[253,254] Since the amount of NPs is not enough to form a protective layer and prevent the contact between shearing surfaces, it is necessary to increase the concentration of functionalized NPs in the IL to reduce the friction coefficient. However, the NPs start to form aggregates at high concentrations, and the aggregated NPs with non-uniform surface texture and large size tend to wear and scratch the surfaces under loading and sliding as debris particles do.[202,255,256] Therefore, high concentrations of NPs in the IL can adversely influence the lubrication of shearing surfaces.[257] Consequently, the sufficient number of covered nanoparticles can be obtained at the optimal concentration of 0.1 wt.% in order to form a protective film without the agglomeration of the nanoparticles.

B.4.5. Effect of Nanoparticles on Lubrication Behavior of IL

The effect of normal load on friction force for the pure IL, and IL with bare and OTS-functionalized SiO_2 NPs is shown in Figure 55. Here, the comparison is done at the optimum nanoparticle concentration for each system: for functionalized SiO_2 NPs, the concentration was 0.1wt.% while it was 0.05 wt.% for bare SiO_2 NPs (based on our previous work).[202] The friction force was found to linearly increase with increasing normal load for each case. The corresponding friction coefficient of pure IL was calculated to be 0.30±0.01 from the slope. The addition of bare SiO_2 NPs in IL reduced the coefficient of friction to 0.23±0.01, which is 23% less than that for pure IL, while the incorporation of functionalized SiO_2 NPs in IL resulted in a friction coefficient of 0.19±0.01, which is 37.2% and 16.7% less than that for the pure IL and IL with bare SiO_2 NPs, respectively. These data indicate that the presence of silica nanoparticles decreases the friction coefficient of ILs and organosilane functionalized silica nanoparticles outperform bare nanoparticles.

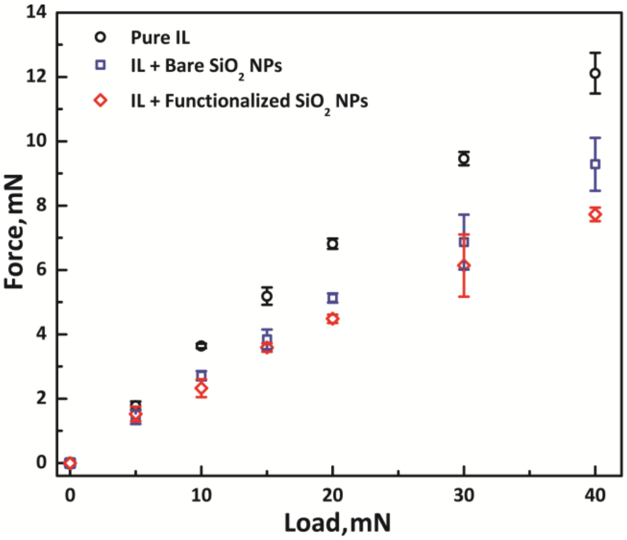

Figure 55. Load versus friction force data for pure IL, IL with 0.05 wt.% bare silica nanoparticles, and IL with 0.1 wt.% organosilane functionalized nanoparticles.

There are two mechanisms that may be responsible for the observed trends: Direct and indirect lubrication effects of nanoparticles. Regarding the direct effects, protective/tribo-film formation and ball bearing mechanism are two prominent models. Regarding the indirect effect, nanoparticles can alter the surface topography in synergistic way through mending/repairing effect or polishing/smoothing effect.

In the ball-bearing mechanism, spherical and quasispherical nanoparticles are believed to function like tiny ball bearings which roll into the contact area. Nanoparticles with such shapes are believed to change the sliding friction to a mix of sliding and rolling friction. This lubrication mechanism is attributed to tribo-pair system having stable low-load conditions between the shearing surfaces to maintain the shape and rigidity of the nanoparticles. There are also experimental studies showing that tribo-film formation mechanism can be responsible for superior lubrication. For example, Verma et al.[258] reported the formation of a durable tribo-film with Mo, S, and P elements, reducing the chances of severe wear, friction, and seizure for nanoMoS_2-based lubricant. The mending effect or self-repairing effect is characterized by nanoparticle deposition to fill scars and grooves of the sliding surfaces. This can happen before or during surfaces get damaged.[258–260] The polishing effect, also termed as smoothing effect, is reported to occur when the roughness of the lubricating surface is reduced by nanoparticle-assisted abrasion. In addition, self-assembled monolayers are well-known to improve the lubricity of sliding surfaces as reported by Yang et al.[261] By the same token, the presence of self-assembled monolayers on nanoparticles, which may be considered an extension of sliding surface, can improve the lubricity.

B.4.6. Rheological Properties

Viscosity of pure IL, and the ILs with various concentrations of bare and OTS-functionalized SiO_2 NP dispersions are shown in Figure 56a and b, respectively, as a function of shear rate. Pure IL and IL dispersions with functionalized NPs at low concentrations showed a Newtonian behavior: viscosity was independent of shear rate. On the other hand, IL dispersion with bare NPs at low concentrations displayed a shear thinning behavior. This difference can be owing to the enhanced colloidal stability and the reduced probability of aggregation for organosilane functionalized nanoparticles compared to bare ones. For all samples, the viscosity of dispersions increased with increasing concentration of SiO_2 NPs. An increase in the additive concentration amplifies the probability of NP agglomeration and network fractal superstructures due to the reduced particle-particle distance and the consequent increase in the frequency of particulate collisions, which leads to increases in viscosity.[262] At NP concentrations of 1 wt.% and above, a shear thinning behavior was observed with both bare and functionalized nanoparticles. The shear thinning behavior indicates a structural or organization rearrangement at increased shear rates. This finding can be explained by the persistence of networks and agglomerates at low shear rates and their disruption and destruction at higher shear rates.[257]

B.4.7. Wear Characteristics of IL Lubrication Systems with Nanoparticles

In addition to improved tribological properties, the additives are often used to protect surfaces against wear.[251] We assessed the wear protection performance of IL-based lubrication systems via secondary electron microscopy by probing the surfaces after undergoing a cyclic friction test in the presence of pure IL, and ILs with 0.05 wt.% bare and 0.1 wt.% OTS-functionalized SiO_2 NPs (Fig. 57). In the case of the pure IL, long scratches and a large amount of debris were observed on the steel surface (Fig. 57a). Meanwhile, the dispersion of bare and OTS-functionalized SiO_2 NPs in the IL resulted in better wear and damage protection than that of pure IL (Figs. 57b and c). To compare the wear characteristics of the pure IL, bare and OTS-functionalized SiO_2 NPs in IL, we compared the width of wear tracks of the steel surfaces, which were found to be 17.2±1.1 μm, 55.9±1.3 μm and 52.4±2.5 μm for pure IL, bare and functionalized NP, respectively. Although the wear track width in the pure IL case was the smallest, severe abrasive damage on the steel surface was clearly observed. On the other hand, dispersion

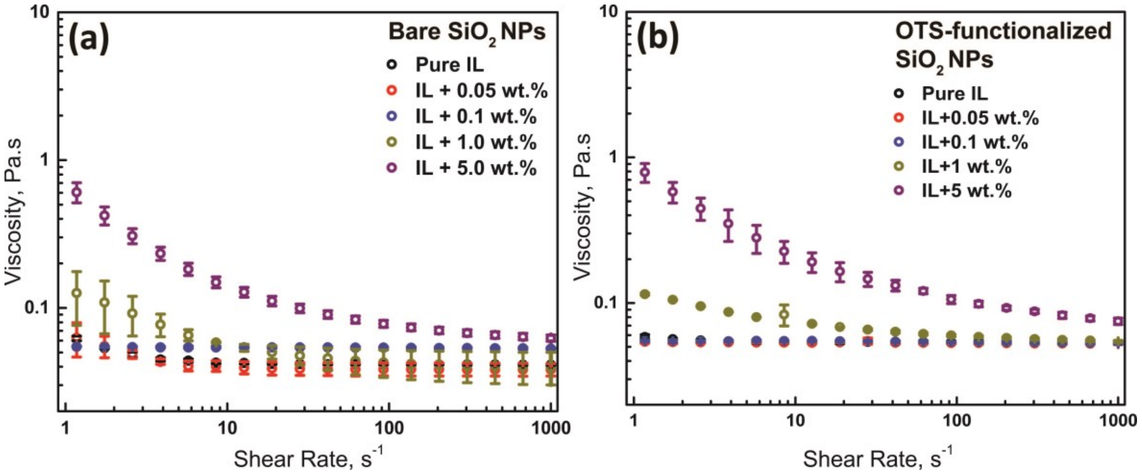

Figure 56. Viscosity of the neat IL and IL with different concentrations of (a) SiO_2 NPs and (b) OTS-functionalized SiO_2 NPs as a function of shear rate

of the NPs in the IL led to a mild damage. The wear track width of bare and functionalized NP correspond to about 6.3% reduction in wear size, which is a small improvement. In both cases the steel surfaces had much better protection than that of IL.

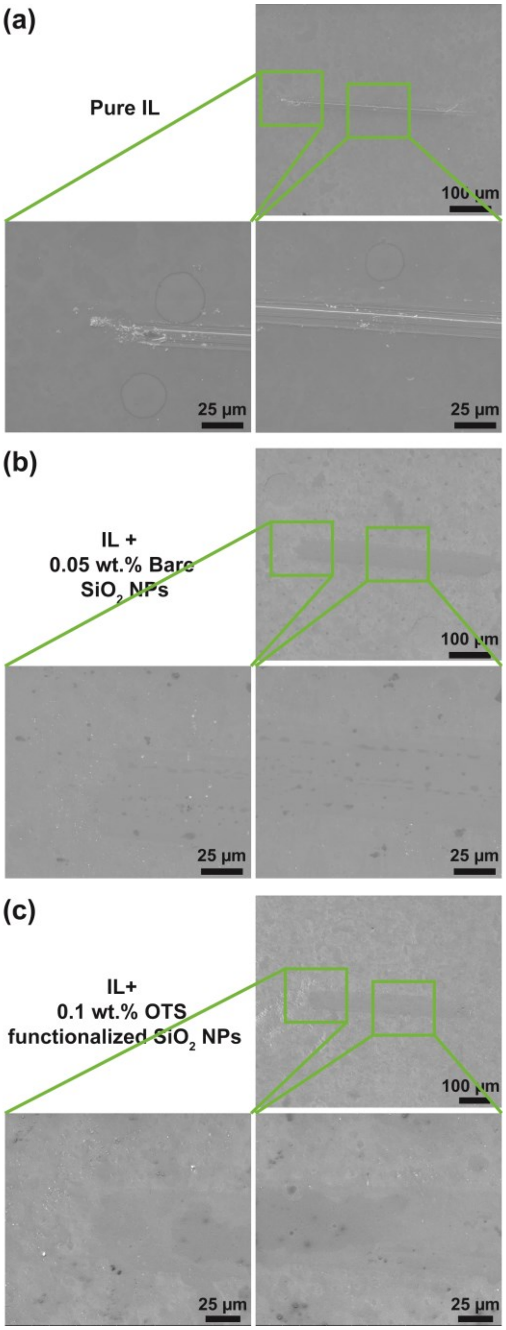

Figure 57. SEM micrographs displaying morphologies of steel surfaces after shearing under three different lubrication conditions: a) pure IL, b) IL + 0.05 wt.% bare SiO_2 NPs, and c) IL + 0.1 wt.% OTS-functionalized SiO_2 NPs. Low and high magnifications of the middle and edge parts of the wear track are shown.

B.5. Conclusions

This study investigates how the presence of nanoparticles (NPs) with and without surface functional groups influences the friction and wear characteristics of an ionic liquid (1-butyl-3-methylimidazolium (trifluoromethysulfony) imide) under boundary lubrication conditions. It was found that: (i) the coefficient of friction depended on the concentration of functionalized NPs and the optimum concentration was 0.1 wt.%, (ii) the addition of functionalized NPs to the IL reduced the coefficient of friction by 37.2% and 16.7% compared to that of pure ionic liquid and IL with bare SiO_2 NPs under boundary lubrication conditions, (iii) the presence of nanoparticles significantly reduced wear and damage on steel surfaces lubricated through the IL. Improvements in tribological performance were ascribed to the roller bearing effect of spherical silica nanoparticles. Furthermore, the functionalized NPs have a hard core/soft shell structure that helps them maintain the rigidity of the NPs while the outer surface is soft, flexible, and slippery.

Moreover, rheological properties of pure IL, IL dispersions involving bare silica NPs, and IL dispersions containing organosilane functionalized silica NPs were compared to gain insight into their lubrication performance under elastohydrodynamic conditions. It was found that (i) pure IL displayed a Newtonian behavior, (ii) IL with bare NPs demonstrated a shear thinning behavior for all concentrations, and (iii) IL with functionalized NPs showed a Newtonian behavior at low concentrations and shear thinning behavior at high concentrations (>1 wt.%). The differences in rheological properties of IL with bare and functionalized NP at low concentrations are attributed to the screening of interparticulate van der Waals interactions due to the low dielectric constant, organosilane layer and resultant changes in the dynamics of formation of particulate fractal networks.

Overall, this study indicates that the addition of nanoparticles, in particular functionalized ones, can further improve the promising tribological properties of ionic liquids and promotes further tribological studies with nanofluids involving ionic liquids and nanoparticles/nanomaterials.